

EXPERIMENTS AND MODELS FOR OPERATION OF A SEALED ENDS  
SQUEEZE FILM DAMPERS: A STEP TOWARDS QUANTIFYING AIR  
INGESTION IN SQUEEZE FILMS

A Dissertation

by

BONJIN KOO

Submitted to the Office of Graduate and Professional Studies of  
Texas A&M University  
in partial fulfillment of the requirements for the degree of  
DOCTOR OF PHILOSOPHY

Chair of Committee,	Luis San Andrés
Committee Members,	Adolfo Delgado
	Waruna Kulatilaka
	Minsu Cha
Head of Department,	Andreas Polycarpou

December 2019

Major Subject: Mechanical Engineering

Copyright 2019 Bonjin Koo

## ABSTRACT

Squeeze film dampers (SFDs) in high-performance turbomachinery reduce rotor motion amplitudes as it traverses a critical speed or when the system has a dynamic instability, thus ensuring system reliability. To improve the damping capacity in aircraft engines within a limited space, piston ring (PR) seals are installed at the axial ends of a film land. Even though PRs effectively seal a SFD, a significant amount of a lubricant exits through the gap at the abutted ends of the PR (PR slit). However, when the squeeze-film pressure is lower than ambient pressure, air ingests into the film and mixes with the lubricant. The advanced turbomachines have a larger operating speed with a smaller lubricant supply than traditional turbomachines; hence, air entrainment in a sealed ends SFD becomes significant.

This dissertation presents a computational physics model for a sealed ends SFD and open to ambient, hence prone to air entrainment; and delivers predictions benchmarked against experimental test results.

The first embodiment is a SFD with a PR and an O-ring (OR) sealing the film land. In the tests, a known gas (air) volume fraction (GVF or  $\beta$ ) in a mixture of air and ISO VG2. The PR and the O-ring (OR) that seal the film land are located in the grooves at the top and bottom of the journal, respectively. The supplied mixture discharges through the PR slit, located at the top axial end, into a vessel submerged within a large volume of lubricant. Another damper, which has same journal geometric parameters, is supplied with a pure lubricant of a supply pressure. Both the top and bottom axial ends are sealed with PRs and opened to ambient. Hence, the supplied lubricant exits through the PR slits

into ambient, and the air ingests through the PR slits when the film pressure is below the ambient pressure.

There are two distinctive models evaluating the evolution of gas volume fraction in a squeeze film land: (a) a volume of fluid (VOF) model and (b) a bubbly mixture. The models predicting the pressure field in the squeeze film implement the Reynolds equation, modified to include temporal fluid inertia effects, and uses physics-based inlet and outlet lubricant conditions through a feed hole and PR slits, respectively

A parametric study produces the dynamic forced performance of the PR sealed ends SFD. The predictions show the time-space average GVF increases as the squeeze velocity ( $v_s$ ) increases. On the other hand, the GVF decreases as the supply pressure increases. The damper physical geometry also affects its dynamic forced performance. The GVF increases as the journal diameter increases; whereas the SFD axial length does not significantly change the GVF. The GVF reduces as the damper clearance increases. The GVF does not significantly change as the PR slit cross-sectional area varies.

An oil supply pressure large enough to prevent air ingestion varies with damper geometry, lubricant inlet/outlet conditions, and the kinematics of the journal. The PR slits allows air ingestion even as the squeeze velocity is small. As the damper diameter to clearance ratio ( $D/c$ ) increases, the GVF in the film increases. Most importantly, the location of the PR slit relative to the feedhole significantly affects the amount of air content in the film. When the PR slit faces to the feedhole, the film land is mostly filled with a pure lubricant. The GVF increases as the arc distance from the PR slit to the feedhole increases.

## DEDICATION

I would like to express my appreciation to my family.

## ACKNOWLEDGEMENTS

Thanks to all the students at the Turbolab, especially, Scott Tran. Special thanks to Sung-hwa, Tingcheng, Xueliang, Wonbae, and Dr. Yang.

I sincerely appreciate to Dr. Luis San Andrés for encouraging me to pursue research at Texas A&M Turbomachinery Laboratory under his guidance. His endeavor towards perfection inspired me.

## CONTRIBUTORS AND FUNDING SOURCES

### **Contributors**

This work is supported by the dissertation committee chair, Dr. Luis San Andrés, and the committee consisting of Dr. Delgado, Dr. Kulatilaka [Mechanical Engineering Department], and Dr. Cha [Civil and Environmental Department].

### **Funding Sources**

Graduate study is supported by Pratt&Whitney and the Texas A&M Turbomachinery Research Consortium.

## NOMENCLATURE

$A_{slit}$	Area of slit (opening) at PR ends [m <sup>2</sup> ]
$c$	Damper radial clearance [m]
$C$	Damping coefficient [N-s/m], $\underline{C} = C/C^*$ [-]
$C_S$	Structural damping coefficient [N-s/m]
$C_d$	Feed hole loss coefficient [-]
$C_{slit}$	Piston ring loss coefficient [-]
$D$	Journal diameter [m]
$f$	Volume of liquid transferred across a cross-sectional area [m <sup>3</sup> ]
$H$	Complex dynamic stiffness [N/m],  $H = K - \omega^2 M + i(\omega C + K_0)$ ; $i = \sqrt{-1}$ .
$h$	Film thickness [m]
$\dot{h}$	Film velocity, $\dot{h} = dh/dt$ [m/s]
$K$	Stiffness coefficient [N/m], $\underline{K} = K/K_{S+seals}$ [-]
$K_0$	Quadrature stiffness [N/m] $\underline{K}_0 = K_0/K_{S+seals}$ [-]
$K_S$	Structural stiffness coefficient [N/m]
$L$	Film axial length [m]

$\dot{m}_g$	Air mass flow at $P_s$ delivered to sparger [kg/s]
$\dot{M}_{in}, \dot{M}_{slit}$	Inlet and outlet mass flow rates [kg/s]
$M$	Added mass coefficients [kg], $\underline{M} = M/M^*$ [-]
$M_{BC}$	Mass of bearing cartridge [kg]
$M_S$	Structural added mass coefficient [kg]
$N_{CFL}$	Courant-Friedrichs-Levy number, $U_{\Theta}dt/(R\Delta\Theta)$ or $U_zdt/(\Delta z)$ [-]
$P$	Fluid film pressure [Pa]
$P_s, P_a$	Supply and ambient pressures [Pa]
$P_v$	Liquid (oil) vapor pressure [1 kPa]
$Q_{in}, Q_{slit}$	Inlet and outlet orifice volumetric flow rate [m <sup>3</sup> /s]
$Q_l$	Oil flow rate delivered to test system [m <sup>3</sup> /s]
$q$	Flow rate of mixture per a unit length [m <sup>2</sup> /s]
$r$	Orbit radius [m]
$Re_s$	$\frac{\rho\omega c^2}{\mu}$ . Squeeze film Reynolds number [-]
$T$	$2\pi/\omega$ . Period of circular whirl motion [s].
$U_B$	Bias uncertainty [-]



$U_V$	Uncertainty due to variability [-]
$v_s$	$r\omega$ . Squeeze film velocity [m/s]
$(X, Y)$	Coordinate systems.
$z$	Axial coordinate [m]
$\alpha$	Liquid volume fraction in mixture
$\beta$	$(1-\alpha)$ . Gas volume fraction (GVF).
$\beta_{avg}$	Time-space average GVF, $\beta_{avg} = \frac{\int \int \int \beta_{(\Theta, z, t)} d\Theta dz dt}{2\pi LT}$ .
$\beta_s$	Gas volume fraction at inlet supply pressure
$\Theta, \theta$	Circumferential coordinates [rad], $\theta = (\Theta - \omega t)$
$\gamma$	Time and space average liquid volume fraction [-]
$\mu_{oil}, \mu_g$	Oil and gas viscosities [Pa-s]
$\mu_m$	Mixture viscosity [Pa-s]
$\phi$	Diameter of feed orifice [m]
$\rho_{oil}, \rho_g$	Oil and gas densities [kg/m <sup>3</sup> ]
$\rho_m$	Mixture density [kg/m <sup>3</sup> ]

$\omega$                     Excitation frequency [rad/s]

$\zeta_s$                     Structural damping ratio

### **Matrices and Vectors**

**a**                    absolute acceleration

**C**                    Damping coefficients

**F**                    Force

**H**                    Complex dynamic stiffness

**K**                    Stiffness coefficients

**M**                    Inertia coefficients

**z**                    BC displacements relative to journal

### **Abbreviations and subscripts**

BC                    Bearing cartridge

CCO                    Circular centered orbit

GVF                    Gas volume fraction

JFO                    Jakobsson-Floberg-Olsson

LVF                    Liquid volume fraction

OR                    O-ring seals

PR                    Piston ring seals

seals    End seals: O-ring + piston ring

S        Structure

SFD     Squeeze film damper

VOF     Volume of fraction

## TABLE OF CONTENTS

	Page
ABSTRACT .....	ii
DEDICATION .....	iv
ACKNOWLEDGEMENTS .....	iv
CONTRIBUTORS AND FUNDING SOURCES.....	vi
NOMENCLATURE.....	vii
TABLE OF CONTENTS .....	xii
LIST OF FIGURES.....	xv
LIST OF TABLES .....	xviii
CHAPTER I INTRODUCTION .....	1
Literature review .....	5
Objectives of work .....	12
CHAPTER II NUMERICAL MODELS FOR A SEALED ENDS SFD	
OPERATING WITH OIL AND GAS.....	14
Boundary conditions considering an inlet feedhole and piston ring abutted end....	17
Gas volume fraction in a SFD operating with a bubbly mixture .....	19
Liquid volume fraction in a SFD operating with a flow of two separate phases ....	21
CHAPTER III DESCRIPTION OF THE EXPERIMENTAL FACILITY AND	
TEST DAMPER.....	31
Test rig description.....	31
CHAPTER IV TEST PROCEDURE AND FORCE COEFFICIENT	
IDENTIFICATION .....	38
Estimation of force coefficients from measurements of force displacements .....	38

CHAPTER V DYNAMIC FORCED PERFORMANCE OF A SEALED ENDS SFD SUPPLIED WITH A BUBBLY MIXTURE TEST DATA AND PREDICTION .....	43
A sample of the measured complex dynamic stiffnesses for the lubricated test system of the PR-OR sealed ends SFD .....	43
Force coefficients for PR-OR sealed ends SFD supplied with a bubbly mixture ...	47
CHAPTER VI DYNAMIC PERFORMANCE OF A SFD SEALED WITH PISTON RINGS AND SLITS OPEN TO AMBIENT (NATURAL AIR INGESTION) .....	54
Complex dynamic stiffness measurements of lubricated system.....	57
PR sealed SFD damping and inertia force coefficients: measurements and predictions .....	60
CHAPTER VII COMPARISONS OF MODEL PREDICTIONS FOR A SEALED ENDS SFD SUPPLIED WITH A BUBBLY MIXTURE AND A PR SEALED SFD WITH PR SLITS OPEN TO AMBIENT.....	65
Note on the computational time .....	65
Comparisons of model predictions.....	67
CHAPTER VIII PARAMETERIC STUDY OF A SEALED SFD WITH ENDS OPEN TO AMBIENT. PREDICTIONS FROM A VOF MODEL AND A BUBBLY MIXTURE MODEL .....	73
Effect of squeeze velocity ( $v_s = r\omega$ ) on the SFD dynamic forced performance.....	76
Effect of location of feedhole and PR slits on SFD dynamic forced performance .	79
Effect of SFD axial length on the SFD dynamic forced performance .....	81
Effect of SFD journal diameter on the SFD dynamic forced performance.....	82
Effect of SFD film clearance on the SFD dynamic forced performance .....	84
Effect of SFD supply pressure on the SFD dynamic forced performance .....	86
Effect of SFD PR slit area on the SFD dynamic forced performance.....	88
CHAPTER IX CONCLUSIONS.....	90

REFERENCES.....	95
APPENDIX A IDENTIFIED PARAMETERS FOR THE UNLUBRICATED TEST SYSTEM.....	101
APPENDIX B UNCERTAINTY OF IDENTIFIED FORCE COEFFICIENTS .....	104
Bias uncertainty.....	104
Uncertainty due to curve fit.....	105
Uncertainty due to variability.....	106
Total uncertainty .....	107
APPENDIX C ESTIMATION OF THE LOSS COEFFICIENTS FOR A FEEDHOLE AND PISTON RING SLITS .....	109

## LIST OF FIGURES

	Page
Figure 1. Schematic view of a hole-fed SFD with end seals.....	2
Figure 2. Schematic view of SFD with a whirling journal and a BC with its coordinate system.....	15
Figure 3. Schematic view of film land in a sealed ends SFD with inlet(hole) and outlet mass (piston ring slits) flows.....	16
Figure 4. Schematic view of pressure around a control volume. Subscripts e,w,n,s denote faces of a control volume towards east, west, north, and south, respectively. This figure is adapted from Ref. [34]......	24
Figure 5. Schematic views of free surface shapes used in the advection of fluid: (a) Donor-acceptor arrangement and (b-e) examples. This figure is adapted from [7]. ..	26
Figure 6. Air is drawn into the damper during the negative dynamic pressure portion of a whirl cycle (d)-(i), and is swept away during the high pressure portion of the wave (a), (b), (c), (k), (l). This figure is adapted from Ref. [19]......	30
Figure 7. Photograph of SFD test rig with shakers and sensors adapted from Ref.[34]. ..	32
Figure 8. Photograph of SFD test rig as lubricated with a controlled bubbly mixture. ...	33
Figure 9. Schematic cross-section view of SFD test rig with flow path for supplied bubbly mixture (not to scale). .....	36
Figure 10. Idealization of mechanical system as a point mass (bearing cartridge) and force coefficients for squeeze film, structure, and end seals.....	41
Figure 11. SFD operating with a bubbly mixture ( $\beta_s=0.0$ and $0.5$ ): Lubricated test system supplied with $P_s = 6.2$ bar(g): real and imaginary parts of complex dynamic stiffnesses ( $H_{XX}, H_{YY}$ ) <sub>L</sub> vs. whirl frequency ( $\omega$ ). Circular centered orbits with amplitude $r = 0.2c$ and frequency $\omega = 10-60$ Hz. One feedhole at ( $\Theta_{in} = 225^\circ, z = -1/2L$ ) and PR slit at $\Theta_{slit} = (315^\circ, z = 1/2L)$ .....	45
Figure 12. SFD operating with a bubbly mixture ( $\beta_s=0.0$ and $0.5$ ): Lubricated test system supplied with $P_s = 2.1$ bar(g): real and imaginary parts of complex dynamic stiffnesses ( $H_{XX}, H_{YY}$ ) <sub>L</sub> vs. whirl frequency ( $\omega$ ). Circular centered orbits with	

amplitude $r = 0.2c$ and frequency $\omega = 10-60$ Hz. One feedhole at $(\Theta_{in} = 225^\circ, z = -1/2L)$ and PR slit at $\Theta_{slit} = (315^\circ, z = 1/2L)$ .....	46
Figure 13. SFD operating with a bubbly mixture: Experimentally derived and predicted damping coefficients ( $\underline{C}_{SFD}$ ) vs. supply pressure ( $P_s$ ) and vs. inlet gas volume fraction ( $\beta_s$ ) at $P_s$ . Top graphs show the $XX$ -coefficient, and bottom graphs show the $YY$ -coefficient.....	49
Figure 14. SFD operating with a bubbly mixture: Experimentally derived and predicted added mass coefficients ( $\underline{M}_{SFD}$ ) vs. supply pressure ( $P_s$ ) and vs. inlet gas volume fraction ( $\beta_s$ ) at $P_s$ . Top graphs show the $XX$ -coefficient, and bottom graphs show the $YY$ -coefficient.....	50
Figure 15. SFD operating with a bubbly mixture: Experimentally derived quadrature stiffnesses ( $\underline{K}_{oSFD}$ ) vs. supply pressure ( $P_s$ ) and vs. inlet gas volume fraction ( $\beta_s$ ) at $P_s$ . 51	
Figure 16. Experimentally derived and predicted direct stiffnesses ( $\underline{K}_{SFD}$ ) vs. supply pressure ( $P_s$ ) and vs. inlet gas volume fraction ( $\beta_s$ ) at $P_s$ . Top graphs show the $XX$ -coefficient, and bottom graphs show the $YY$ -coefficient.....	52
Figure 17. Schematic view of SFD test rig configuration for tests with air ingestion. ....	55
Figure 18. Photograph of a PR sealed ends SFD operating with PR slits open to ambient. ....	56
Figure 19. PR sealed SFD with PR slits open to ambient. Real and imaginary parts of complex dynamic stiffnesses ( $H_{XX}, H_{YY}$ ) <sub>L</sub> vs. whirl frequency ( $\omega$ ). Lubricant supplied at $P_s = 0.7$ bar(g). Circular centered orbits with amplitude $r = 0.2c$ and frequency $\omega = 40-70$ Hz. One feedhole at $(\Theta_{in} = 225^\circ, z = 0.0)$ and PR slits at $\Theta_{slit} = (315^\circ, z = \pm 1/2L)$ ...58	
Figure 20. PR sealed SFD with PR slits open to ambient. Real and imaginary parts of complex dynamic stiffnesses ( $H_{XX}, H_{YY}$ ) <sub>L</sub> vs. whirl frequency ( $\omega$ ). Lubricant supplied at $P_s = 4.1$ bar(g). Circular centered orbits with amplitude $r = 0.2c$ and frequency $\omega = 40-70$ Hz. One feedhole at $(\Theta_{in} = 225^\circ, z = 0.0)$ and PR slits at $\Theta_{slit} = (315^\circ, z = \pm 1/2L)$ ...59	
Figure 21. PR sealed SFD with PR slits open to ambient: Predicted average GVF ( $\beta_{avg}$ ) vs. supply pressure ( $P_s$ ) and whirl frequency ( $\omega$ ). Orbit radius $r = 0.2c$ . $\Delta\Theta = \Theta_{slit} - \Theta_{in} = 90^\circ$ . ....	61
Figure 22. PR sealed SFD with PR slits open to ambient: Experimentally derived and predicted (a) damping ( $\underline{C}$ ) and (b) inertia ( $\underline{M}$ ) coefficients vs. supply pressure ( $P_s$ ). Orbit radius $r = 0.2c$ and whirl frequency $\omega = 40-70$ Hz. $\Delta\Theta = \Theta_{slit} - \Theta_{in} = 90^\circ$ . ....	64



Figure 23. Flowchart of the SFD computational model using VOF method. ....	66
Figure 24. Predicted film pressure field, gas volume fraction, and film thickness vs. circumferential coordinate and axial coordinate produced by (a) VOF model and (b) bubbly mixture model with $\beta_s=0.3$ . Supply pressure $P_s=0.7$ bar(g). Orbit radius $r=0.2c$ . Whirl frequency $\omega=60$ Hz. $t=3/8T$ when the film thickness is the largest at the feedhole.....	69
Figure 25. VOF model predicted film pressure ( $\underline{P}$ ) and GVF at $z=0$ , film thickness ( $\underline{h}$ ) and film velocity ( $\underline{\dot{h}}$ ) vs. circumferential coordinate ( $\Theta$ ) at $t=0, 1/4T, 1/2T$ , and $3/4T$ . Supply pressure $P_s=0.7$ bar(g). Orbit radius $r=0.2c$ . Whirl frequency $\omega=60$ Hz. $v_s=28$ mm/s. $\Delta\Theta=\Theta_{slit}-\Theta_{in}=90^\circ$ . ....	70
Figure 26. Dynamic film pressure and film thickness at $\Theta=45^\circ$ vs. time ( $t/T$ ). Supply pressure $P_s=0.8$ bar(g). Orbit radius $r=0.2c$ . Whirl frequency $\omega=30$ Hz. Squeeze velocity $v_s\sim 14$ mm/s. Reynolds # $Re_s=8$ . Graphs include measured data and predictions from (a) VOF model and (b) bubbly mixture model. ....	72
Figure 27. Dynamic film pressure and film thickness at $\Theta=45^\circ$ vs. time ( $t/T$ ). Supply pressure $P_s=0.7$ bar(g). Orbit radius $r=0.2c$ . Whirl frequency $\omega=60$ Hz. Squeeze velocity $v_s\sim 28$ mm/s. Reynolds # $Re_s=16$ . Graphs include measured data and predictions from (a) VOF model and (b) bubbly mixture model. ....	72
Figure 28. SFD operating with a circular centered orbit.....	74
Figure 29. Predicted film reaction forces in tangential and radial directions vs. time. Supply pressure $P_s=0.7$ bar(g). Orbit radius $r=0.2c$ . Whirl frequency $\omega=60$ Hz. Squeeze velocity $v_s\sim 28$ mm/s. Reynolds # $Re_s=16$ . ....	75
Figure 30. Average GVF, film peak-to-peak pressure, and damping and inertia coefficients ( $\underline{C}_t, \underline{M}_r$ ) vs. whirl frequency: Predictions from (a) VOF model and (b) bubbly mixture model. $P_s=0.7$ bar(g), $D=127$ mm, $L=25.4$ mm, $c=373$ mm, $\Delta\Theta=\Theta_{slit}-\Theta_{in}=90^\circ$ , $r=0.2c$ , $A_{slit}=2$ mm <sup>2</sup> . ....	78
Figure 31. Average GVF, film peak-to-peak pressure, and damping and inertia coefficients ( $\underline{C}_t, \underline{M}_r$ ) vs. orbit radius ( $r/c$ ): Predictions from (a) VOF model and (b) bubbly mixture model. $P_s=0.7$ bar(g), $D=127$ mm, $L=25.4$ mm, $c=373$ mm, $\Delta\Theta=90^\circ$ , $\omega=60$ Hz, $A_{slit}=2$ mm <sup>2</sup> .....	79
Figure 32. Average GVF, film peak-to-peak pressure, and damping and inertia coefficients ( $\underline{C}_t, \underline{M}_r$ ) vs. angular distance between PR slit and feedhole ( $\Delta\Theta$ ): Predictions from (a) VOF model and (b) bubbly mixture model. $P_s=0.7$ bar(g), $D=127$ mm, $L=25.4$ mm, $c=373$ mm, $r=0.2c$ , $\omega=60$ Hz, $A_{slit}=2$ mm <sup>2</sup> .....	80

Figure 33. Average GVF, film peak-to-peak pressure, and damping and inertia coefficients ( $\underline{C}_t$ ,  $\underline{M}_r$ ) vs. seal axial length ( $L$ ): Predictions from (a) VOF mode I and (b) bubbly mixture model.  $P_s=0.7$  bar(g),  $D=127$  mm,  $c=373$ mm,  $r=0.2c$ ,  $\omega=60$  Hz,  $\Delta\Theta=90^\circ$ ,  $A_{slit}=2$  mm<sup>2</sup>. .....82

Figure 34. Average GVF, film peak-to-peak pressure, and damping and inertia coefficients ( $\underline{C}_t$ ,  $\underline{M}_r$ ) vs. journal diameter ( $D$ ): Predictions from (a) VOF model and (b) bubbly mixture model.  $P_s=0.7$  bar(g),  $L=25.4$  mm,  $c=373$ mm,  $r=0.2c$ ,  $\omega=60$  Hz,  $\Delta\Theta=90^\circ$ ,  $A_{slit}=2$  mm<sup>2</sup>. .....83

Figure 35. Average GVF, film peak-to-peak pressure, and damping and inertia coefficients ( $\underline{C}_t$ ,  $\underline{M}_r$ ) vs. film clearance ( $c$ ): Predictions from (a) VOF model and (b) bubbly mixture model.  $P_s=0.7$  bar(g),  $D=127$  mm,  $L=25.4$  mm,  $r=0.2c$ ,  $\omega=60$  Hz,  $\Delta\Theta=90^\circ$ ,  $A_{slit}=2$  mm<sup>2</sup>. .....85

Figure 36. Average GVF, film peak-to-peak pressure, and damping and inertia coefficients ( $\underline{C}_t$ ,  $\underline{M}_r$ ) vs. supply pressure ( $P_s$ ): Predictions from (a) VOF model and (b) bubbly mixture model.  $D=127$  mm,  $L=25.4$  mm,  $c=373$ mm,  $r=0.2c$ ,  $\omega=60$  Hz,  $\Delta\Theta=90^\circ$ ,  $A_{slit}=2$  mm<sup>2</sup>. .....87

Figure 37. Average GVF, film peak-to-peak pressure, and damping and inertia coefficients ( $\underline{C}_t$ ,  $\underline{M}_r$ ) vs. PR slit area ( $A_{slit}$ ): Predictions from (a) VOF model and (b) bubbly mixture model.  $P_s=0.7$  bar(g),  $D=127$  mm,  $L=25.4$  mm,  $c=373$ mm,  $r=0.2c$ ,  $\omega=60$  Hz,  $\Delta\Theta=90^\circ$ .....89

## LIST OF TABLES

	Page
Table 1. Dimensions of SFD test section and lubricant properties. ....	34
Table 2. Representative gas mixture volume fraction (GVF) and gas mass fraction (GMF) vs. supply pressure. ....	37
Table 3. Measured and predicted flowrates supplied to test SFD.....	63
Table 4. SFD physical geometry parameters and operating conditions. The nominal condition is bolded. ....	73
Table A1. Dry system structural parameters (without and with end seals) obtained from circular orbit tests without any lubricant. Parameters identified over frequency range 10–60 Hz. Orbit amplitude $r = 0.2c$ . ....	101
Table B1. Measured system force coefficients $(K,C,M)_L$ for the PR sealed ends SFD test rig at nominal operating condition, $P_s = 0.7$ bar(g), $r = 0.2c$ , and $\omega = 40-70$ Hz. ....	106

# CHAPTER I

## INTRODUCTION

A modern rotating machine operates at a high rotor speed to achieve higher power density and efficiency. High-performance turbomachine commonly experiences significant dynamic loads that produce excessive amplitude rotor motions. A broad range of operating speeds, including critical speeds, and a use of tighter clearances in secondary flow passages help make vibration problems acute. Pertaining to aircraft engines, squeeze film dampers (SFDs) add a significant damping to rigid ball bearings that commonly lack this ability. SFDs isolate mechanical components of turbo machines, reduce excessive amplitudes of rotor synchronous vibration, and aid to reduce non-synchronous rotor instabilities. SFDs also decrease the transmission of forces to the bearing supports for operation at supercritical speeds [1, 2].

Figure 1 depicts a schematic view of a sealed ends SFD in series with a ball bearing supported rotor. An annular gap between a bearing cartridge and the outer race of a ball bearing makes the lubricant film. An anti-rotation (dowel) pin or a centering spring (squirrel cage) prevents rotation of the outer race of the ball bearing. SFDs whirl due to rotor vibrations caused by rotor dynamic displacements squeezing the lubricant film and thus generate a large hydrodynamic pressure field producing a dynamic reaction force. End seals amplify the viscous damping within a limited space and operate with a small amount of lubricant flow. Most dampers in practice are short in axial length ( $L/D < 0.5$ ) to save space [1].

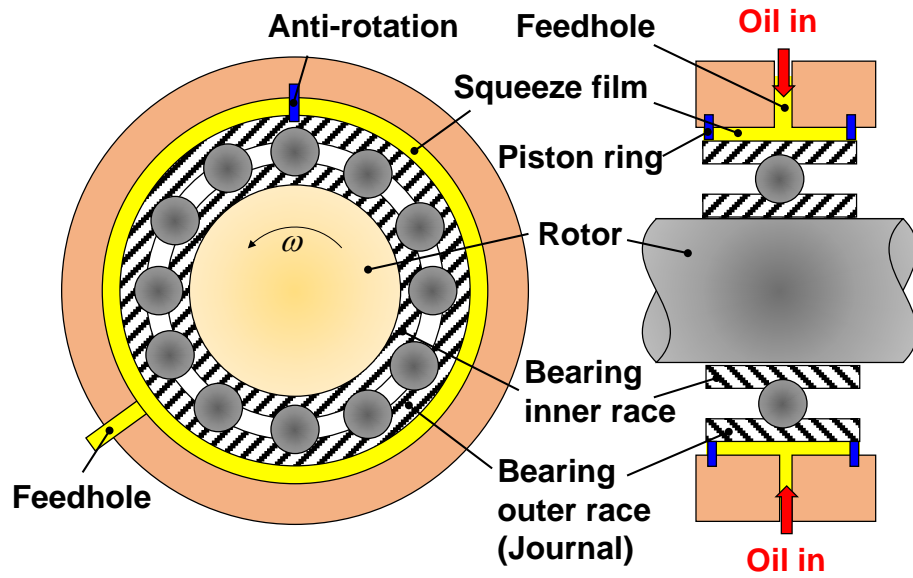


**Figure 1. Schematic view of a hole-fed SFD with end seals.**

Often simplified predictive models miss important physical phenomena observed in actual application of SFDs [3, 4]. Understanding air ingestion in a sealed ends SFD is particularly of note to accurately predict the force performance, as air contents in a film greatly affect the SFD forced performance characteristics. There is no literature on a predictive model considering fluid inertia in the film land and air ingestion through piston ring slits.

According to the classical lubrication theory, squeeze film forces generated by a journal whirl motion can be classified into both viscous type and inertial type. The contribution of the fluid inertia effect to the film reaction force is quantified in terms of the squeeze film Reynolds number ( $Re_s = \rho\omega c^2/\mu$ ), where  $\omega$  is a journal whirl frequency,  $c$  a radial film clearance, and  $\rho$  and  $\mu$  the lubricant density and viscosity, respectively.

Squeeze film forces are (typically) represented in linearized form as follows:

$$F = -M \ddot{z} - C \dot{z} - K z \quad (1)$$

where  $(K, C, M)$  are the stiffness, damping, and inertia force coefficients, respectively, and  $(z, \dot{z}, \ddot{z})$  the instantaneous journal center displacement, velocity, and acceleration, respectively. Noteworthy is SFDs do not generally produce a direct stiffness,  $K \sim 0$  [1]; thus, the squeeze film force is determined by the net force from the fluid viscous and inertia effects. In many applications,  $Re_s < 1$  due to a relatively small clearance ( $c$ ) [3, 4].

When the fluid inertia effect is negligible ( $M \sim 0$ ), the squeeze film reaction force is proportional to the instantaneous velocity of the journal center. However, San Andrés (1985) [5] experimentally shows the importance of fluid inertia effects in a sealed ends SFD test rig and states that for  $Re_s > 10$ , the radial film force from fluid inertia is comparable with the tangential force arising from fluid viscosity. An apparent added mass ( $M$ ) characterizes the fluid inertia effect generated by the acceleration of the lubricant (not the journal) within the clearance.

A rotor-bearing system natural frequency can be affected significantly by the added mass with respect to the journal mass. For a tightly sealed ends damper operating with a centered circular orbit (CCO) under a full film condition, the damper force coefficients ( $C, M$ ) are as [5]:

$$C^* = 12 \pi \mu L \left( \frac{D}{2c} \right)^3 \quad (2a)$$

$$M^* = \rho \frac{\pi L}{c} \left( \frac{D}{2} \right)^3 \quad (2b)$$

In particular, for a  $\pi$ -film (or half film) model, the damping and added mass coefficients are  $\frac{1}{2} C^*$  and  $\frac{1}{2} M^*$ , respectively. From Eq. (2), for a journal whirling with a centered circular orbit, the ratio between the film inertia (radial) force and the viscous (tangential) force is

$$\left| \frac{F_r}{F_t} \right| = \frac{M a_s}{C v_s} = \frac{1}{12} \left( \frac{\rho}{\mu} \omega c^2 \right) = \frac{1}{12} \text{Re}_s \quad (3)$$

where  $v_s = r\omega$  and  $a_s = r\omega^2$ .  $\text{Re}_s = \rho\omega c^2/\mu$  is the squeeze film Reynolds number. Above,  $|F_r| > |F_t|$  for  $\text{Re}_s > 12$ . The damping and added mass coefficients ( $C^*$ ,  $M^*$ ) are strictly valid for SFDs that are fully submerged in a pool of lubricant. Hence, the force coefficients in Eq. (3) are not adequate for SFDs that draw air into the film land, i.e., air ingestion.

The presence of oil vapor or air in lubricant is generally acknowledged as the main source of discrepancy between theory and practice of SFD [4]. Typically, with the help of a sufficiently high oil flow rate, end seals effectively prevent air ingestion into a film land. Thus, many sealed ends SFDs operating with a large squeeze velocity ( $v_s = r\omega$ ) are most likely to operate with oil vapor cavitation rather than with air ingestion. However, recent tests [6] show that a piston ring (PR) sealed ends damper lubricated with a low supply pressure source (low flow rate) produce significant air ingestion when the squeeze velocity ( $v_s = r\omega$ )  $> 30$  mm/s. Dynamic film pressure measurements and visual inspection show that air ingestion into the film of the sealed ends SFD increases with a decrease in the supplied oil pressure.

The prediction of force coefficients in SFDs is useful for rotor-bearing designers working in high-speed turbomachinery. However, the trend toward more stringent operating conditions, such as with a low oil flow rate (a low supply pressure), with a larger radial clearance, as tighter axial end seals. The low oil flow rate starves the film and causes a significant amount of air ingestion. A more accurate predictive model that accounts for air ingestion is needed. A large amount of research addressing two-phase flows in SFDs is available [8-20]; however, none of these references presents a realistic model for PR sealed ends SFDs operating with air ingestion.

This dissertation investigates how the degree of air ingestion in a damper film land affects its dynamic forced performance. The results will give engineers insight to better design sealed ends SFDs and will assist their needs to engineer better rotor-bearing systems.

### **Literature review**

Zeidan et al. (1996) [3] show practical designs of SFDs and their successful application in aircraft engines and commercial turbomachinery. Adilleta and Della Pietra (2002) [4] review the theoretical and experimental research on SFDs for over four decades since the 1960's. The rich history of the studies on SFDs emphasizes that oil cavitation in a squeeze film strongly influences SFD forced performance and its dynamic force coefficients.

Zeidan et al. (1990) [8] and Braun and Hannon (2010) [9] summarize about studies on SFDs operating under oil vapor cavitation and/or air ingestion/entrapment. The



appearance of either oil cavitation or air ingestion mainly depends on operation conditions such as supply pressure/flow rate, squeeze film velocity (orbit radius  $\times$  whirl frequency), and the journal static eccentricity.

Oil vapor cavitation is characterized by phase transition (from liquid to gas) of a lubricant boiling near zero absolute pressure. This phenomenon appears when a sealed ends SFD operates with a supply pressure supplying an enough flow to prevent air ingestion. [1, 8]. Jung and Vance [10, 11] analytically and experimentally investigated the effects of oil vapor cavitation on the force coefficients of an SFD and used the Swift-Stieber cavitation condition [12,13] to model oil vapor cavitation. The test SFD is a short-length SFD ( $L/D \sim 0.2$ ) with a large clearance ( $c/D = 0.01$ ). An O-ring tightly seals one axial end of the damper; whereas a serrated piston ring (PR) seal with 72 semicircular holes seals another end. The serrated PR seal efficiently prevents air ingestion in the SFD when operating with a low supply pressure ( $P_s = 0.7$  bar(g)) and squeeze film velocity ranging  $v_s = (\text{orbit amplitude } r \times \text{whirl frequency } \omega) = 0.15$  m/s to 0.23 m/s.

Recently, Bayada, and Chupin (2013) [14] introduce a vaporous oil cavitation model applied to a thin film and including lubricant compressibility. The authors compare their results against those obtained with Jakobsson-Floberg-Olsson (JFO) and the Elrod-Adam's (EA) models [15, 16]. The JFO/EA models satisfy mass conservation under the assumption of constant pressure in a cavitation zone and a film pressure above the lubricant vapor pressure. The model by Bayada and Chupin treats a lubricant as a homogeneous compressible mixture with a possible oil saturation pressure below the

pure lubricant cavitation pressure assumed in JFO/EA model. The saturation pressure considers the density and the sound speed of both the liquid and the vapor. The vaporous oil cavitation model can better predict for a lubricant starvation flow condition (an insufficient inlet flow) compared to the JFO/EA models.

In sealed ends SFDs lubricant vapor cavitation frequently appears [4], but air ingestion is commonly observed in open (to ambient) ends SFDs operating with a squeeze film velocity ( $v_s=r\omega$ )  $>10$  mm/s and a low supply pressure ( $P_s < 1$  bar(g)) (low flow rate). Entrained air persists even in the film high pressure regions [1, 8].

Sun and Brewe [17] present equations to calculate the characteristic time for the formation of either a void due to an oil vapor or that for a dissolved gas bubble to come out. The authors show that the evaporation time, i.e., phase change from liquid to gas, is much faster than the time taken by a dissolved gas to release from a lubricant. Hence, the bubbles in the film are likely due to vapor cavitation and not dissolved gas. White [18] and Zeidan and Vance [19] argue that persistent gas bubbles in a squeeze film damper operating with a squeeze velocity  $v_s = 47$  mm/s are not dissolved gas bubbles but entrained air.

Later, Tao et al. [20] and Diaz and San Andrés [21] present the formulation of the non-homogenous bubbly mixture due to air ingestion and entrapment within a periodically moving film at high frequency. They advance a modified Reynolds equation for SFDs operating with a bubbly mixture. The predicted peak film pressures and forces compare well with measurements conducted in an open end SFD operating with a bubbly mixture under a controlled (known) gas volume fraction. The authors also

introduce a flow parameter  $\gamma = \frac{Q_s}{(\pi D L r \omega)}$ , which represents the ratio of the lubricant supplied flowrate ( $Q_s$ ) to the dynamic flow change in the film volume at any instant of time. When  $\gamma \geq 1$  the supplied inlet flow rate is adequate; hence, the film is fully filled by the lubricant. Whereas, when  $\gamma < 1$  air is ingested into the film land.

Diaz and San Andrés [21] validate an air entrainment predictive model with the flow parameter ( $\gamma$ ) by comparing the predictions with the measurements of a SFD operating under both natural air ingestion or with a controlled oil supplied flowrate to 1.2 LPM. The open ends SFD has  $D = 129$  mm,  $L = 31$  mm, and  $c = 0.343$  mm. For a small to large squeeze film velocity ( $v_s = 20$  mm/s to 110 mm/s), predictions of film pressure and forces correlate well with the measurements. The amount of air in the film highly depends on the test apparatus and operating conditions ( $P_s$  and  $v_s$ ).

Later, Mendez et al. [22] extend the work of Diaz and San Andrés [21] to consider a finite length damper ( $L/D \neq 0$ ). The amount of entrained air decreases as the slenderness ( $L/D$ ) ratio increases. The authors show that for an infinite long-length SFD (i.e. a sealed ends SFD) there should be nearly no air ingestion. However, in practice, end seals cannot perfectly prevent air ingestion due to PR slits or discharge holes open to ambient.

To model SFDs operating with air ingestion, Xing et al. [23, 24] use three-dimensional Navier-Stokes equations (NSE) coupled with a model assuming the oil cavitation zone is homogeneous in terms of pressure and gas volume fraction. In these studies. The CFD predictions show that the film peak pressure decreases with an increase in the gas volume fraction of the mixture. The predicted damping coefficient for

a low gas volume fraction is greater than that from the  $\pi$ -film assumption albeit it decreases with an increase in gas volume fraction. The decrease in the direct damping coefficient can cause an increase in the rotor vibration amplitude near the critical speed as it reduces the system damping ratio. The authors also emphasize that both the gas volume fraction and oil cavitation play an important role in rotor-bearing system dynamics. Noteworthy is that the authors do not consider fluid inertia in their study as the fluid density is set to  $\sim 0.0$ , i.e., the film flow is Stokes flow.

Younan et al. [25] analyze a rotordynamic system supported on an SFD operating with air ingestion. At one axial end, a tight seal prevents the outward flow of a lubricant while the other end allows a high pressure lubricant exiting to a reservoir. The paper presents a new model using a bubbly mixture model adopted from Nikolajsen [26] to derive a nonlinear Reynolds equation for SFDs that includes air entrainment. The density of the mixture is a function of the air bubble diameter and the surface tension of the bubble. As expected, an increase in air volume fraction decreases the peak film pressure and the squeeze film force. In particular, at a large air volume fraction of the supplied mixture, the model better agrees with the experimental results shown in Ref. [15] than other predictions obtained with JFO model, which is shown in the same reference.

Gehannin et al. [27] use the volume of fluid (VOF) method to model air ingestion in open ends SFDs. By adopting the VOF method originally proposed by Hirt and Nicholas [7], the authors introduce a numerical model for SFDs operating with both oil vapor cavitation and/or air ingestion. This method captures the free boundary of an incompressible liquid, implying a non-contamination of an incompressible lubricant with

air bubbles, i.e., two separate fluid zones. It solves a single set of momentum equations and tracks the volume fractions. The numerical results agree well with experimental data by Adilletta and Pietra [28] and demonstrate the influence of vapor cavitation and air ingestion on the performance of an open ends SFD. However, the predictions underestimate the extent of the flat (constant) pressure zone due to air ingestion, i.e., the air ingestion at the SFD is underestimated.

In general, tight end seals may prevent air entrainment into the film where supplied with a sufficiently large flow rate. The film may experience lubricant vapor cavitation. There are few technical papers discussing the effect of air entrainment on a sealed ends SFD. In particular, a piston ring (PR) seal has abutted ends (slit) that allow air ingestion. The flow through the PR slit is simply ignored in most predictive models until recently [39].

Zeidan and Vance [29] obtain SFD fluid film force coefficients from the measured responses of rotors supported on SFDs. For test conditions with loose end seals and operation at a low pressure supply, the amount of entrained air increases with rotor center squeeze velocity ( $v_s$ ). Under a high oil supply pressure or configured with tight end seals, oil vapor cavitation appears only for operation with the journal orbiting with a large amplitude orbit. The test results show that both oil vapor cavitation and air ingestion lead to a nonlinear effect on the operation of SFDs. Oil vapor cavitation shows a hardening effect of the film effective stiffness ( $K_{eff} \sim \omega^2$ ), whereas air ingestion causes a softening effect of the film effective stiffness under certain operating conditions ( $K_{eff} < 0$ ).

Dousti [30] presents a numerical analysis of SFDs using the extended Reynolds equation considering temporal fluid inertia effects. This model is similar to that derived by San Andrés and Delgado [31], but includes a second-order temporal fluid inertia term. The dissertation proves this secondary term is not important in a SFD dynamic force performance. Dousti states that tight axial end seals cannot fully prevent air ingestion; hence, in most configurations, including sealed ends SFDs, a  $\pi$ -film model should be adequate in a predictive analysis.

Recently, Jeung (2017) [6] measure film dynamic pressure profiles in a tightly sealed ends SFD operating with a low pressure supply ( $< 1$  bar(g)) and under moderate to large orbit amplitude motions ( $v_s = 43$  mm/s – 86 mm/s). The pressure profiles show similar shapes (flat pressure zone) observed as those in Refs. [5, 32], thus evidencing the presence of both oil vapor cavitation and air ingestion. For a moderate oil supply pressure (2.8 bar(g)), the dynamic pressure profile shows a flat pressure zone near zero absolute pressure to evidence oil vapor cavitation; whereas, for a low oil supply pressure (0.7 bar(g)), the dynamic pressure wave shows high frequency spikes and a flat pressure zone near ambient pressure, thus indicating air ingestion.

Note that a tightly sealed damper with PRs only allows flow through the PR slits. This configuration is different from those in Refs. [5, 32]. According to Jeung [6], oil vapor cavitation is seen to occur for operation at a squeeze velocity ( $v_s$ ) of 86 mm/s and with an oil supply pressure of 2.8 bar(g). On the other hand, air ingestion occurs for operation with an oil supply pressure of 0.7 bar(g). Furthermore, for operation with squeeze velocities ( $v_s$ ) ranging from 64 mm/s to 86 mm/s, and with an oil supply

pressure of 0.7 bar(g), both air ingestion and vapor cavitation coexist with in the squeeze film.

### **Objectives of work**

In most cases, air ingestion appears in open ends SFDs. However, in recent research, Jeung [6] shows pressure profiles evidencing presence of both oil vapor cavitation and air ingestion in a tightly sealed ends SFD. San Andrés et al. [39] state the abutted ends (slits) of a PR allow for air ingestion even with a tightly sealed ends SFD. The presence of air causes large discrepancies between the measurements and predictions of a SFD dynamic forced performance.

This dissertation contemplates the following

1. Model PR sealed ends SFDs lubricated with a lubricant and air mixture to quantify the effect of air content on the dynamic forced performance of a sealed ends SFD.
2. Model PR sealed ends SFDs to quantify air ingestion thru PR slits using a VOF method. The VOF method tracks the location of the interface between a lubricant and air by solving a transport equation for the liquid volume fraction in the flow field [7].
3. Compare predictions of film dynamic pressures and forces with corresponding measurements. The tests include measurements with a piston ring (PR) sealed ends damper with PR slits (abutted area) and a single lubricant feedhole.

4. Perform a parametric study to obtain the forced performance of a PR sealed ends SFD with lubricant discharging to an open plenum ambient. The parametric study shows the effects of journal kinematics, damper geometry, and lubricant supply/discharge conditions on the dynamic forced performance of the SFD.



## CHAPTER II<sup>1</sup>

### NUMERICAL MODELS FOR A SEALED ENDS SFD OPERATING WITH OIL AND GAS

Figure 2 gives a schematic view of a simple squeeze film with an off-centered journal describing a circular motion with amplitude  $r$  and frequency  $\omega$ . The graph includes a coordinate system  $(X, Y)$ ;  $\Theta$  denotes the circumferential coordinate with origin at the  $-X$  axis. The journal kinematics superimposes a static off-centered eccentricity  $(e_{X_0}, e_{Y_0})$  and a dynamic motion  $(r_{X(t)}, r_{Y(t)})$ . Hence, the instantaneous position of the journal center  $(e_X, e_Y)$  is as follows:

$$e_{X(t)} = e_{X_0} + r_{X(t)}, \quad e_{Y(t)} = e_{Y_0} + r_{Y(t)} \quad (4)$$

In the vector form, the journal eccentricity at a given time is  $\mathbf{e}_{(t)} = \mathbf{e}_0 + \mathbf{r}_{(t)}$ . For circular centered orbits (CCO) with amplitude  $r$ , the vector  $\mathbf{r}_{(t)}$  with a whirl frequency  $\omega$  is

$$\mathbf{r}_{(t)} = \begin{bmatrix} r_X \\ r_Y \end{bmatrix} = r \begin{bmatrix} \cos(\omega t + \phi) \\ \sin(\omega t + \phi) \end{bmatrix} \quad (5)$$

---

<sup>1</sup> Portions of this section reprinted with permission from [41] *Model and Experimental Verification of the Dynamic Forced Performance of a Tightly Sealed Squeeze Film Damper Supplied with a Bubbly Mixture* by San Andrés, L., and Koo, B., 2019, ASME J. Eng. Gas Turb. Pwr., GTP-19-1415, Copyright 2019 by ASME.

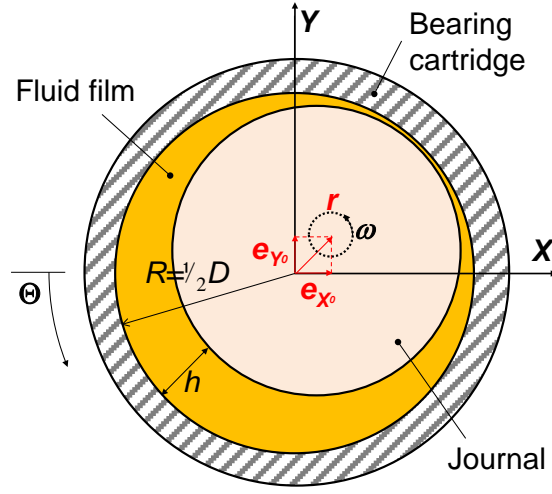


**Figure 2. Schematic view of SFD with a whirling journal and a BC with its coordinate system.**

The film thickness  $h$

$$h_{(\Theta,t)} = c + r \cos(\Theta - \omega t - \phi) \quad (6)$$

Note, the film thickness  $h$  does not vary along the axial direction. The time derivatives of the film thickness equal to

$$\frac{\partial h}{\partial t} = v_s \sin(\Theta - \omega t - \phi) \quad (7)$$

$$\frac{\partial^2 h}{\partial t^2} = -r \omega^2 \cos(\Theta - \omega t - \phi) \quad (8)$$

where  $v_s (= r\omega)$  is the squeeze film velocity.

The journal motion squeezes a mixture of lubricant and gas to generate a hydrodynamic pressure field ( $P$ ) that produces a fluid film reaction force acting on the journal. Figure 3 depicts a schematic view of a film land of a sealed ends SFD with its inlet and outlet mass flows.

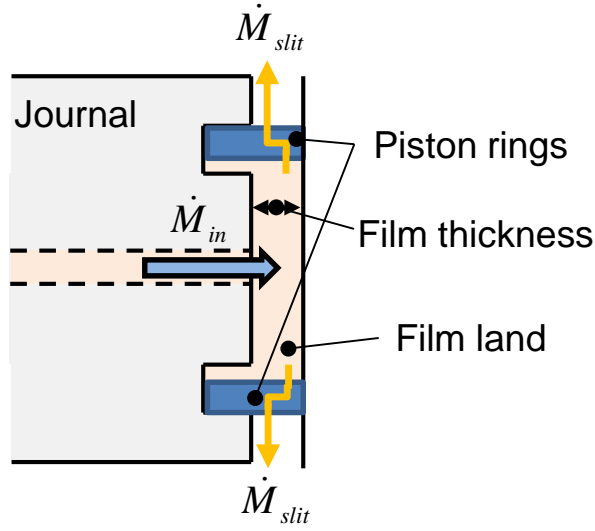


**Figure 3. Schematic view of film land in a sealed ends SFD with inlet (hole) and outlet mass (piston ring slits) flows.**

The governing equation for the generation of squeeze-film pressure in an oil and gas mixture is [21, 31] as follows:

$$\frac{\partial}{R\partial\Theta}\left(\frac{\rho_m h^3}{12\mu_m}\frac{\partial P}{R\partial\Theta}\right) + \frac{\partial}{\partial z}\left(\frac{\rho_m h^3}{12\mu_m}\frac{\partial P}{\partial z}\right) = \frac{\partial}{\partial t}(\rho_m h) + \frac{\rho_m h^2}{12\mu_m}\frac{\partial^2}{\partial t^2}(\rho_m h) + \sum_k\left(\frac{\dot{M}_s}{A}\right)_k \delta_k \quad (9)$$

Above  $\rho_m$  and  $\mu_m$  are the mixture (effective) density and viscosity;  $\dot{M}_s$  stands for a local source or sink of mass flow. Note that  $\dot{M}_{s,k} = \rho_k Q_k$ , where the subscript  $k$  is either *in* for an inlet feedhole or *slit* for a PR slit;  $Q_k$  denotes a volumetric flow rate and  $A_k$  is the area of a feedhole or a PR slit. At a feedhole or a PR slit,  $\delta_k = 1$ , whereas  $\delta_k = 0$  at other locations. Note that  $\dot{M}_{in} > 0$  for an inlet feedhole, and  $\dot{M}_{slit} < 0$  for a PR slit. If there is no squeeze film velocity  $v_s = r\omega = 0$ , then  $\dot{M}_{in} = -2\dot{M}_{slit}$  as PRs are located at both ends of a damper film land as shown in Fig. 3.

The mixture properties are a function of the gas(air) volume fraction  $\beta$  [12], i.e.

$$\rho_m = (1 - \beta_{(\Theta, z, t)}) \rho_{oil} + \beta_{(\Theta, z, t)} \rho_{air} \sim \alpha \rho_{oil} \quad (10a)$$

$$\mu_m = (1 - \beta_{(\Theta, z, t)}) \mu_{oil} + \beta_{(\Theta, z, t)} \mu_{air} \sim \alpha \mu_{oil} \quad (10b)$$

The LVF ( $\alpha = 1 - \beta$ ) ranges from one for pure oil content to zero for just air content. The approximate expressions on the right side follow since  $\mu_{oil} \gg \mu_{air}$  and  $\rho_{oil} \gg \rho_{air}$ .

Clearly  $\beta < 0$ .

Eq. (9) is applicable over a region containing two distinct components, liquid and/or gas, and cannot account for vapor cavitation (phase change). Note, Eq. (9) is actually derived from the mass flow conservation equation,

$$\frac{\partial(\dot{m}_\theta)}{R\partial\Theta} + \frac{\partial(\dot{m}_z)}{\partial z} + \frac{\partial(\rho_m h)}{\partial t} + \sum_k \left( \frac{\dot{M}_s}{A} \right)_k \delta_k = 0 \quad (11)$$

where

$$\dot{m}_\theta = \rho_m h U_\theta \leftarrow U_\theta = -\frac{h^2}{12\mu_m} \frac{\partial P}{R\partial\Theta} \quad (12)$$

$$\dot{m}_z = \rho_m h U_z \leftarrow U_z = -\frac{h^2}{12\mu_m} \frac{\partial P}{\partial z} \quad (13)$$

are mass flow rates per unit length and ( $U_\theta$ ,  $U_z$ ) are the mixture mean flow circumferential and axial velocities.

### **Boundary conditions considering an inlet feedhole and piston ring abutted end**

The pressure field needs to be continuous and periodic in the circumferential direction,  $P_{(\theta, z, t)} = P_{(\theta + 2\pi, z, t)}$ ; and if the journal motion is periodic in time, the pressure field must also show the same periodicity, i.e.,  $P_{(\theta, z, t)} = P_{(\theta, z, t + 2T)}$ , where  $T = 2\pi/\omega$ . At an inlet

hole with area  $A_{in} = \pi/4 \phi_{in}^2$  located at  $\{\Theta_{in}, z=0\}$ , where  $\phi_{in}$  is a diameter of the inlet hole, the supply mass flow of lubricant is

$$\dot{M}_{in} = \rho_{in} Q_{in} = \text{sgn}\left(P_s - P_{(\Theta_{in}, 0)}\right) \left[ C_d A_{in} \sqrt{2\rho_{in} \left| P_s - P_{(\Theta_{in}, 0)} \right|} \right] \quad (14)$$

where  $P_s$  is the lubricant supply pressure (well upstream of the hole) and  $P_{(\Theta_{in}, 0)}$  is the film pressure. Above  $C_d$  denotes an empirically determined orifice pressure loss coefficient. Eq. (14) allows backward flow modeling an orifice feedhole without a check valve. If a check valve is present,  $M_{in} \sim 0.0$  when  $P_s < P_{(\Theta_{in}, 0)}$ .

Conventional analyses [5, 33] typically model the outflow through end seals as proportional to a local pressure drop ( $P_{out} - P_a$ ) and an (empirical) end-seal coefficient. In lieu of the profuse experimental evidence, this widespread model is presently abandoned (see for example Ref. [34]). As early as in 1991, a photograph in Ref.[19] shows a jet-like outflow through the PR slit. Thus, the mass flow through a PR slit with area  $A_{slit}$  is modeled as

$$\dot{M}_{slit} = \rho_{slit} Q_{slit} = \text{sgn}\left(P_a - P_{(\Theta_{slit}, \pm 1/2 L)}\right) \left[ C_{slit} A_{slit} \sqrt{2\rho_{slit} \left| P_{(\Theta_{slit}, \pm 1/2 L)} - P_a \right|} \right] \quad (15)$$

with  $P_{(\Theta_{slit}, \pm 1/2 L)}$  as the film pressure just upstream of the PR slit;  $Q_{slit}$  denotes a local outlet volume flow through the PR slit.  $\rho_{slit} = \rho_{(\Theta_{slit}, \pm 1/2 L)}$  if  $P_a < P_{(\Theta_{slit}, \pm 1/2 L)}$  otherwise  $\rho_{slit} = \rho_{air}$ .

The computational physics program implements a finite element method (FEM) to iteratively solve the modified Reynolds Eq.(9) and which includes an update of the mixture properties. The process simultaneously solves for the pressure field and updates the gas volume fraction ( $\beta$ ), its time derivatives, the mixture density, and viscosity at

every time step (200 time steps in one period of whirl motion). A difference of a percent or less between consecutive iteration pressure fields determines convergence.

Diaz and San Andrés [21] make predictions (vs. test data) about open end SFD operating with a bubbly mixture. For example, the model considers the pressure to rotate around the bearing circumference,  $P_{(\theta-\omega t, z)}$ , without any distortion, and uses the kinematic conditions [ $\theta = \Theta - \omega t$ ],

$$\frac{\partial \beta}{\partial t} = -\omega \frac{\partial \beta}{\partial \theta}, \quad \frac{\partial^2 \beta}{\partial t^2} = \omega^2 \frac{\partial^2 \beta}{\partial \theta^2} \quad (16)$$

The kinematic relations above show that the film thickness and its temporal (time) derivatives are time-invariant in the rotating coordinate system. This assumption can cause a large error near feedholes or PR slits. The current transient response analysis does not use Eqs. (16) but will apply a “true” time derivative calculated from the (stored) pressure field and LVF calculated in the previous time steps. The first iteration shows the code assumes the film land is filled with just pure oil, and the whirl motion gradually ingests air content within the film land through the PR slit. It takes a number of full periods to obtain a dynamic pressure field evolving toward a steady condition.

### **Gas volume fraction in a SFD operating with a bubbly mixture**

Diaz and San Andrés [21] introduce a simplified form of the Plesset equation for use in SFDs to account for a bubbly mixture in an open ends SFD. The authors assume a homogeneous bubbly mixture of air and lubricant and use a simple model for the GVF ( $\beta$ ):

$$\beta_{(P)} = 1 - \alpha_{(P)} = \frac{1}{1 + \frac{P_{(\theta,z,t)} - P_v}{P_s - P_v} \left( \frac{1 - \beta_s}{\beta_s} \right)} \quad (17)$$

where  $P_v$  is the lubricant vapor pressure (1 kPa) and  $\beta_s = (1 - \alpha_s)$  the gas volume fraction at  $P_s$  (supply pressure).

A volume integration of Eq. (11) gives

$$\iiint \left[ \frac{\partial \rho_m}{\partial t} + \nabla \cdot (\rho_m \mathbf{U}) \right] dV = 0 \Rightarrow \dot{M}_{in} + 2\dot{M}_{slit} = \frac{\partial M_v}{\partial t} \quad (18)$$

where  $\mathbf{U}$  is the flow velocity vector and  $\dot{M}_{in}$  and  $\dot{M}_{slit}$  are the inlet and outlet mass flow rates, respectively. The mass in the film land is

$$M_v = \tilde{\rho}_{m(t)} V \quad (19)$$

where the volume of the film land is  $V$  and a spatial average of the mass density over the

whole domain is  $\tilde{\rho}_{m(t)} = \frac{1}{V} \iiint \rho_{m(x,y,z,t)} dV$ . For a half volume on the side of the

squeezing volume,  $\frac{1}{2} \frac{dV}{dt} = r\omega\pi RL$ . Hence, the time derivative of the mass at half

volume is

$$\frac{1}{2} \dot{M}_v = \frac{1}{2} \dot{\tilde{\rho}}_m V + \tilde{\rho}_m \left( \frac{1}{2} \dot{V} \right) \quad (20)$$

Over a time period,  $T = 2\pi/\omega$ , an averaged mass in the film is

$$\frac{1}{2} \dot{M}_v \approx \bar{\tilde{\rho}}_m \left( \frac{1}{2} \dot{V} \right) = \bar{\tilde{\rho}}_m (r\omega\pi RL) \approx \gamma \rho_{oil} (r\omega\pi RL); \quad \bar{\tilde{\rho}}_m \approx \gamma \rho_{oil} \quad (21)$$

where  $\gamma$  is a time and space average liquid volume fraction, i.e.,

$$\gamma = \frac{1}{T} \int_t^{t+T} \frac{1}{V} \iiint \alpha \, dV dt .$$

From Eqs.(18, 21), the ratio of the supplied oil flow to the magnitude of the dynamic squeeze film is

$$\gamma = \frac{\frac{1}{2T} \int_t^{t+T} \dot{M}_{in} + 2\dot{M}_{slit} dt}{\rho_{oil} r \omega \pi RL} \Rightarrow \gamma = \frac{1/2 Q_{s,dyn}}{v_s \pi RL} = \frac{Q_{s,dyn}}{v_s \pi DL} \quad (22)$$

where  $Q_{s,dyn}$  is a dynamic flow rate, i.e., sum of the inlet flow thru the feedhole and the outlet flow thru the PR slits. Air will be ingested into the film ( $\gamma < 1$ ) if the dynamic flow is insufficient to fill the film volume ( $Q_{s,dyn} < v_s \pi DL$ ). Eq.(22) shows that air ingestion depends both on the lubricant supply condition and the kinematics of journal motion.

For an open ends SFD, the experimental results in Ref. [21] advance an empirical correlation between  $\gamma$  and  $\beta$ , i.e,  $\beta$  decreases as  $\gamma$  increases. However, the flow parameter  $\gamma$  is yet to be fully quantified for a PR sealed ends SFD discharging to ambient.

### **Liquid volume fraction in a SFD operating with a flow of two separate phases**

Several approaches assume the lubricant as a continuous homogeneous gas in liquid mixture. However, for the case of two separate immiscible phases, a specific computational fluid dynamics method known as the volume of fluid (VOF) method is adopted. This method introduced by Hirt and Nichols [7] is one of the most popular models for modeling two-phase flows. Here, a location of an interface between two phases is calculated by a transport equation delivering the volume of fraction of liquid in a computational cell. In application to SFD flow, this method must be adopted for thin



film flows dominated by two different length scales, film thickness, and damper circumference. Gehannin et al. [27] successfully adapted the VOF method to model an open ends SFD.

The total mass of a mixture in a given volume is an integral of the mixture density;

$$\iiint \rho_m dV \quad (23)$$

The mass per unit time flowing through the surface of the volume is

$$\oint \rho_m \mathbf{U} \cdot \mathbf{n} dS \quad (24)$$

where  $\mathbf{U}$  is the flow velocity vector, and  $dS$  and  $\mathbf{n}$  denote the surface element area and the surface normal vector, respectively. The rate of mass change in a volume equals to the mass flow thru the surface. Hence,

$$\frac{\partial}{\partial t} \iiint \rho_m dV = -\oint \rho_m \mathbf{U} \cdot \mathbf{n} dS \quad (25)$$

By Gauss theorem

$$\oint \rho_m \mathbf{U} \cdot \mathbf{n} dS = \iiint [\nabla \cdot (\rho_m \mathbf{U})] dV \quad (26)$$

Hence,

$$\iiint \left[ \frac{\partial \rho_m}{\partial t} + \nabla \cdot (\rho_m \mathbf{U}) \right] dV = 0 \quad (27)$$

Since  $\rho_m \sim \alpha \rho_{oil}$ ,

$$\iiint \left[ \frac{\partial \alpha \rho_{oil}}{\partial t} + \nabla \cdot (\alpha \rho_{oil} \mathbf{U}) \right] dV = 0 \quad (28)$$

By using the product rule for partial differentiation of three variables ( $\alpha$ ,  $\rho_{oil}$ , and  $\mathbf{U}$ ),

$$\iiint \left[ \alpha \left( \frac{\partial \rho_{oil}}{\partial t} + \nabla \cdot (\mathbf{U} \rho_{oil}) \right) + \rho_{oil} \frac{\partial \alpha}{\partial t} + \rho_{oil} \mathbf{U} \nabla \cdot (\alpha) \right] dV = 0 \quad (29)$$

The first term of the left hand side of Eq.(29) equals zero since  $\frac{\partial \rho_{oil}}{\partial t} + \nabla \cdot (\mathbf{U} \rho_{oil}) = 0$  (continuity equation) and  $\rho_{oil}$  is constant (incompressible). Hence,

$$\frac{D\alpha}{Dt} = \frac{\partial \alpha}{\partial t} + \nabla \cdot (\alpha \mathbf{U}) - \alpha (\nabla \cdot \mathbf{U}) = 0 \quad (30)$$

This equation states that  $(\alpha \times \rho_{oil})$  is a material constant in the flow domain. This means the total oil mass in the film region is constant at any given time.

Assuming a constant volume fraction ( $\alpha$ ) across the film thickness, integration of Eq. (30) across the gap gives [7]

$$\frac{\partial(\alpha h)}{\partial t} + \nabla \cdot (\alpha \mathbf{q}) = \alpha \left( \frac{\partial h}{\partial t} + \nabla \cdot \mathbf{q} \right) \quad (31a)$$

where  $\mathbf{q} = (q_\theta, q_z) = (hU_\theta, hU_z)$ , flow rates per unit length with  $(U_\theta, U_z)$  as the mean flow circumferential and axial velocities.

Eqn. (31a) is also written as

$$\frac{\partial(\alpha h)}{\partial t} + \frac{\partial(\alpha U_\theta h)}{R \partial \Theta} + \frac{\partial(\alpha U_z h)}{\partial z} = \alpha \left( \frac{\partial h}{\partial t} + \frac{\partial(U_\theta h)}{R \partial \Theta} + \frac{\partial(U_z h)}{\partial z} \right) \quad (31b)$$

Where  $q_\theta = U_\theta h = \frac{h^3}{12\mu_m} \frac{\partial P}{R \partial \Theta}$  and  $q_z = U_z h = \frac{h^3}{12\mu_m} \frac{\partial P}{\partial z}$ .

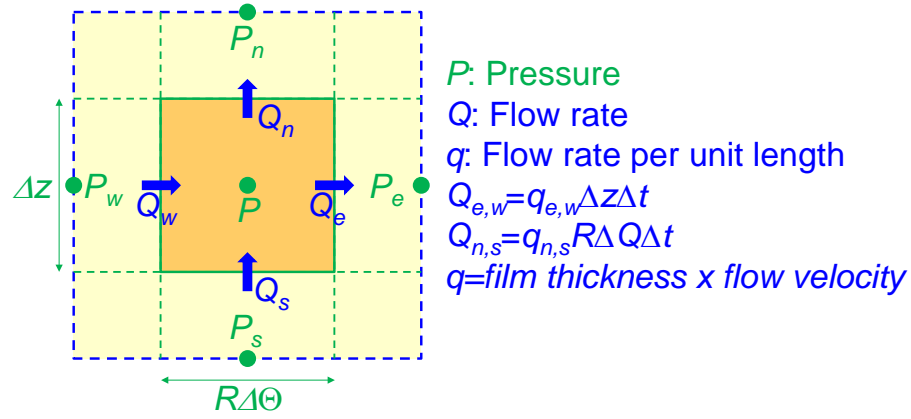


**Figure 4. Schematic view of pressure around a control volume. Subscripts e,w,n,s denote faces of a control volume towards east, west, north, and south, respectively. This figure is adapted from Ref. [34].**

Take a control volume with its east and west faces along the circumferential direction ( $R\Delta\Theta$ ) and north and south faces along the axial direction ( $\Delta z$ ). Integration of Eq. (31a) in a control volume gives, using Green's Theorem,

$$\begin{aligned} \iint \left[ \frac{\partial(\alpha h)}{\partial t} + \nabla \cdot (\alpha \mathbf{q}) \right] .dA &= \iint \alpha \left( \frac{\partial h}{\partial t} + \nabla \cdot \mathbf{q} \right) .dA \rightarrow \\ \iint \left[ \frac{\partial(\alpha h)}{\partial t} \right] .dA + \oint \alpha q_n ds &= \iint \alpha \left( \frac{\partial h}{\partial t} \right) .dA + \alpha \oint q_n ds \end{aligned} \quad (32)$$

The terms  $\oint f_n ds$  denote the flow of variable  $f$  across the boundary (= faces) of a control

volume. An approximation of the volume integral  $\iint \left[ \frac{\partial(\alpha h)}{\partial t} \right] .dA \sim \frac{\partial(\alpha h)}{\partial t} R\Delta\Theta\Delta z$  ;

then, Eq. (32) becomes

$$\begin{aligned} \frac{\partial(\alpha h)}{\partial t} R\Delta\Theta\Delta z + ([q_e \alpha_e - q_w \alpha_w] \Delta z + [q_n \alpha_n - q_s \alpha_s] R\Delta\Theta) \\ = \alpha \left( \frac{\partial h}{\partial t} \right) R\Delta\Theta\Delta z + \alpha ([q_e - q_w] \Delta z + [q_n - q_s] R\Delta\Theta) \end{aligned} \quad (33)$$

where  $q_e=(U_e h_e)$  is the flow of mixture through the east face,  $(\alpha_e q_e)$  is the flow of liquid through the same face,  $q_n=(U_n h_n)$  is the flow of mixture through the north face of the control volume, etc.

Introduce a forward difference for the time-derivative  $\frac{\partial(\alpha h)}{\partial t}$  above. Hence, Eq. (33)

becomes

$$\begin{aligned} & [(\alpha h)_{t+\Delta t} - (\alpha h)_t] R\Delta\Theta\Delta z + ([q_e\alpha_e - q_w\alpha_w]\Delta z + [q_n\alpha_n - q_s\alpha_s]R\Delta\Theta)\Delta t \\ & = \alpha [(h)_{t+\Delta t} - (h)_t] R\Delta\Theta\Delta z + \alpha ([q_e - q_w]\Delta z + [q_n - q_s]R\Delta\Theta)\Delta t \end{aligned} \quad (34)$$

Let the transferred or displaced fluid volumes (mixture and liquid) be

Mixture	Liquid
$Q_e = q_e\Delta z\Delta t$	$f_e = (\alpha Q)_e$
$Q_w = q_w\Delta z\Delta t$	$f_w = (\alpha Q)_w$
$Q_n = q_n R\Delta\Theta\Delta t$	$f_n = (\alpha Q)_n$
$Q_s = q_s R\Delta\Theta\Delta t$	$f_s = (\alpha Q)_s$

Then,

$$\begin{aligned} & [(\alpha_{t+\Delta t} \Delta V_{h_{t+\Delta t}}) - (\alpha_t \Delta V_{h_t})] + (f_e - f_w + f_n - f_s) \\ & = \alpha [\Delta V_{h_{t+\Delta t}} - \Delta V_{h_t}] + \alpha (q_e - q_w + q_n - q_s) \end{aligned} \quad (35)$$

$$\begin{aligned} & (\alpha_{t+\Delta t} \Delta V_{h_{t+\Delta t}}) - \alpha_{t+\Delta t} [\Delta V_{h_{t+\Delta t}} - \Delta V_{h_t}] - \alpha_{t+\Delta t} (q_e - q_w + q_n - q_s)_t \\ & = (\alpha_t \Delta V_{h_t}) - (f_e - f_w + f_n - f_s)_t \end{aligned} \quad (36)$$

Cancelling like terms give the following:

$$\alpha_{t+\Delta t} \left\{ [\Delta V_{h_{(t)}}] - (\sum q) \right\} = (\alpha_t \Delta V_{h_{(t)}}) - (\sum f)_t \quad (37)$$

In the VOF method [7], a special equation known as the donor-acceptor flux approximation evaluates the volume of liquid  $f_i \equiv (\alpha Q)_i$  transferred across the faces  $I = w, e, n, \text{ or } s$  of a control volume ( $\Delta V_h$ ) during a one-time step  $\Delta t$ . Figure 5 displays a graphical explanation the volume of the transferred liquid.

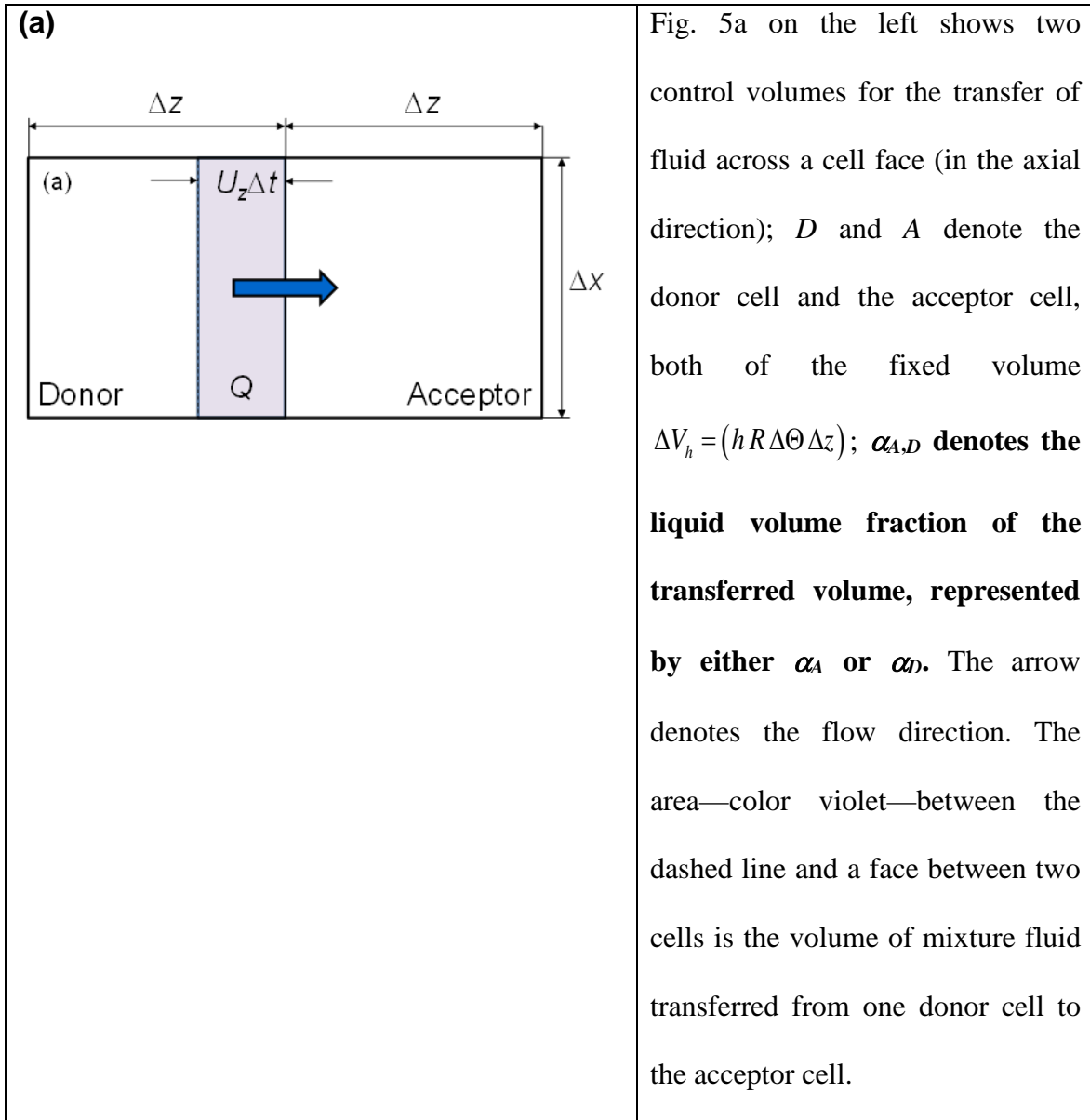


**Figure 5. Schematic views of free surface shapes used in the advection of fluid: (a) Donor-acceptor arrangement and (b-e) examples. This figure is adapted from Ref. [7].**

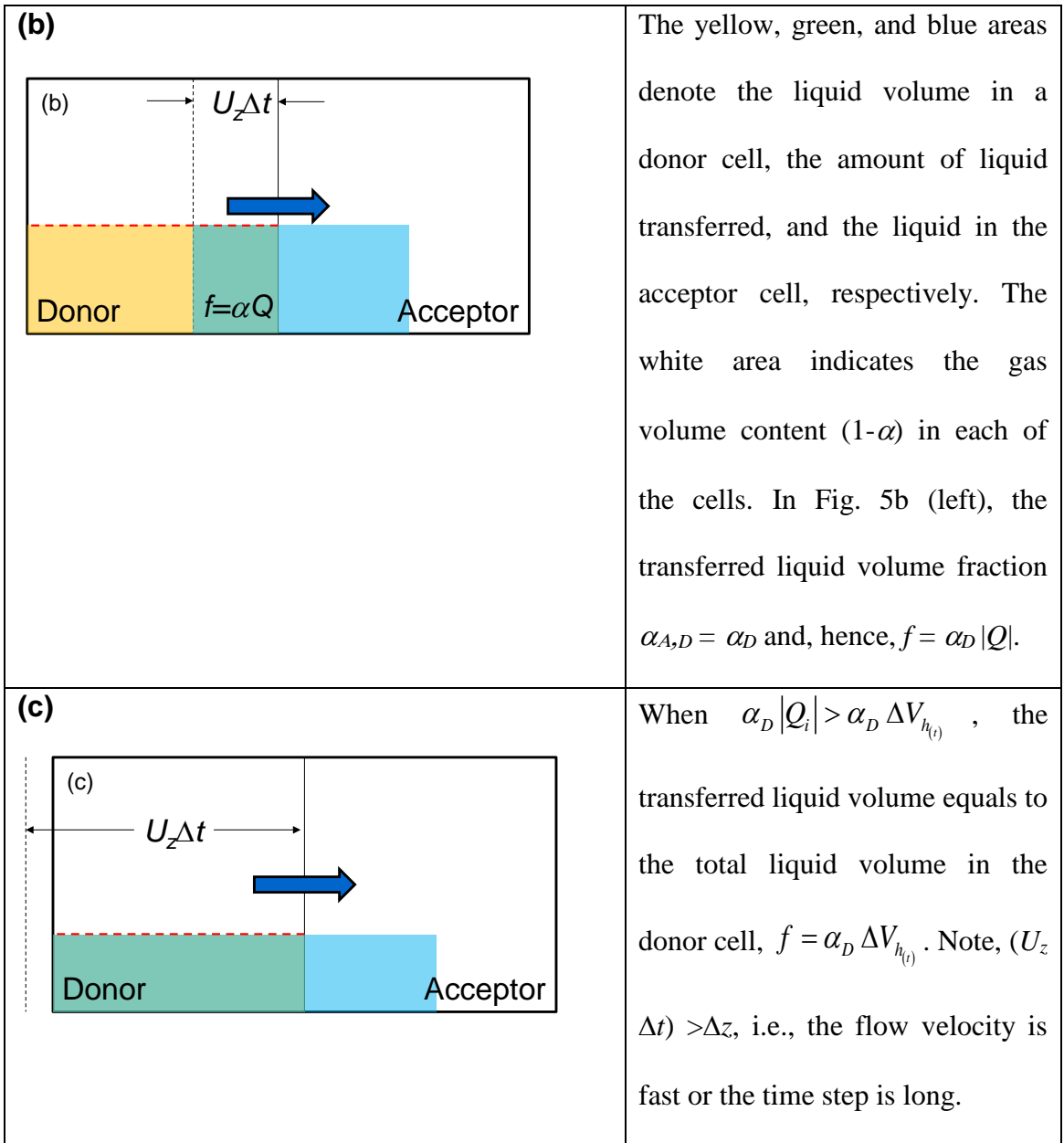
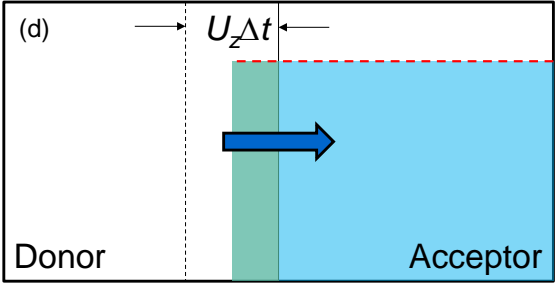
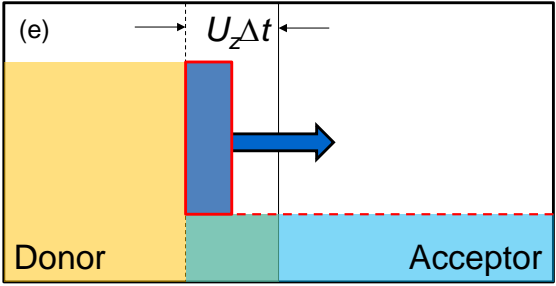


Figure 5. (continued)

<p><b>(d)</b></p>  <p>Donor</p> <p>Acceptor</p>	<p>The volume fraction <math>\alpha_A</math> in the acceptor cell defines the volume fraction <math>\alpha_{A,D}</math> of the transferred volume across the cell face, i.e. <math>\alpha_{A,D} = \alpha_A</math>, when all the fluid in the donor cell is transferred and the liquid lying in the transition area is transferred to the acceptor cell.</p> <p>Note, <math>f = \alpha_D \Delta V_{h(t)} &lt; \alpha_A  Q </math>.</p>
<p><b>(e)</b></p>  <p>Donor</p> <p>Acceptor</p>	<p>When <math>\alpha_{A,D} = \alpha_A</math>, more liquid needs to be transferred than the amount <math>\alpha_A  Q </math>. The extra fluid in the transition area (box with red sides) is known as an additional volume of liquid (<math>CF</math>).</p>

**Figure 5. (continued)**

Ref. [7] present equations for the fraction of liquid ( $\alpha$ ) across the  $i$ -face of a control volume and during one time step  $\Delta t$ :

$$f_i = \begin{cases} \alpha_{A,D} |Q_i| + CF & \text{if } (\alpha_{A,D} |Q_i| + CF) < (\alpha_D \Delta V_{h(t)}) \\ (\alpha_D \Delta V_{h(t)}) & \text{if } (\alpha_{A,D} |Q_i| + CF) > (\alpha_D \Delta V_{h(t)}) \end{cases} \quad (38)$$

$$\text{where } CF = \begin{cases} (1 - \alpha_{A,D})|Q_i| - (1 - \alpha_D)(\alpha_D \Delta V_h) & \text{if } (1 - \alpha_{A,D})|Q_i| > (1 - \alpha_D)(\alpha_D \Delta V_h) \\ \text{otherwise } 0 \end{cases}$$

A split operator as used in Ref. [27], helps compute the liquid fraction ( $\alpha$ ) even for the case of an empty cell ( $\alpha = 0$  with just air) having two neighbors completely filled with liquid. The split operator has two steps for its calculation: the first involves calculating the volume fraction along the horizontal (circumferential) direction.

$$\alpha^* = \left( \frac{(\alpha_D \Delta V_{h(t)}) - f_e + f_w}{(\Delta V_{h(t)}) - Q_e + Q_w} \right)_t \quad (39)$$

Similarly, the second step involves calculating of the volume fraction along the axial direction:

$$\alpha_{t+\Delta t} = \alpha^* - \frac{(f_n - f_s)^*}{(\Delta V_{h(t)})_{t+\Delta t}} + \frac{\alpha^* (Q_n - Q_s)_t}{(\Delta V_{h(t)})_{t+\Delta t}} \quad (40)$$

Note,  $f_n$  and  $f_s$  are intermediate fluxes (along the north and south faces after calculating the intermediate volume fraction  $\alpha^*$ ) calculated from Eq. (39).

Refs. [6, 19] show a jet (air/oil) mixture quickly entering a film land through a PR slit, see Fig. 6. The jet flow has a large velocity. In the VOF method, this large velocity can be modeled using a very large GVF ( $\beta$ ), i.e., nearly pure air with an extremely small viscosity compared to an oil viscosity. However, the jet flow through a PR slit is difficult to model with the simple VOF method and can cause convergence problems due to the complex flow nature. To avoid the convergence problems and save the computation time, the range of GVF ( $\beta$ ) for analysis is limited from 0.01 to 0.99.



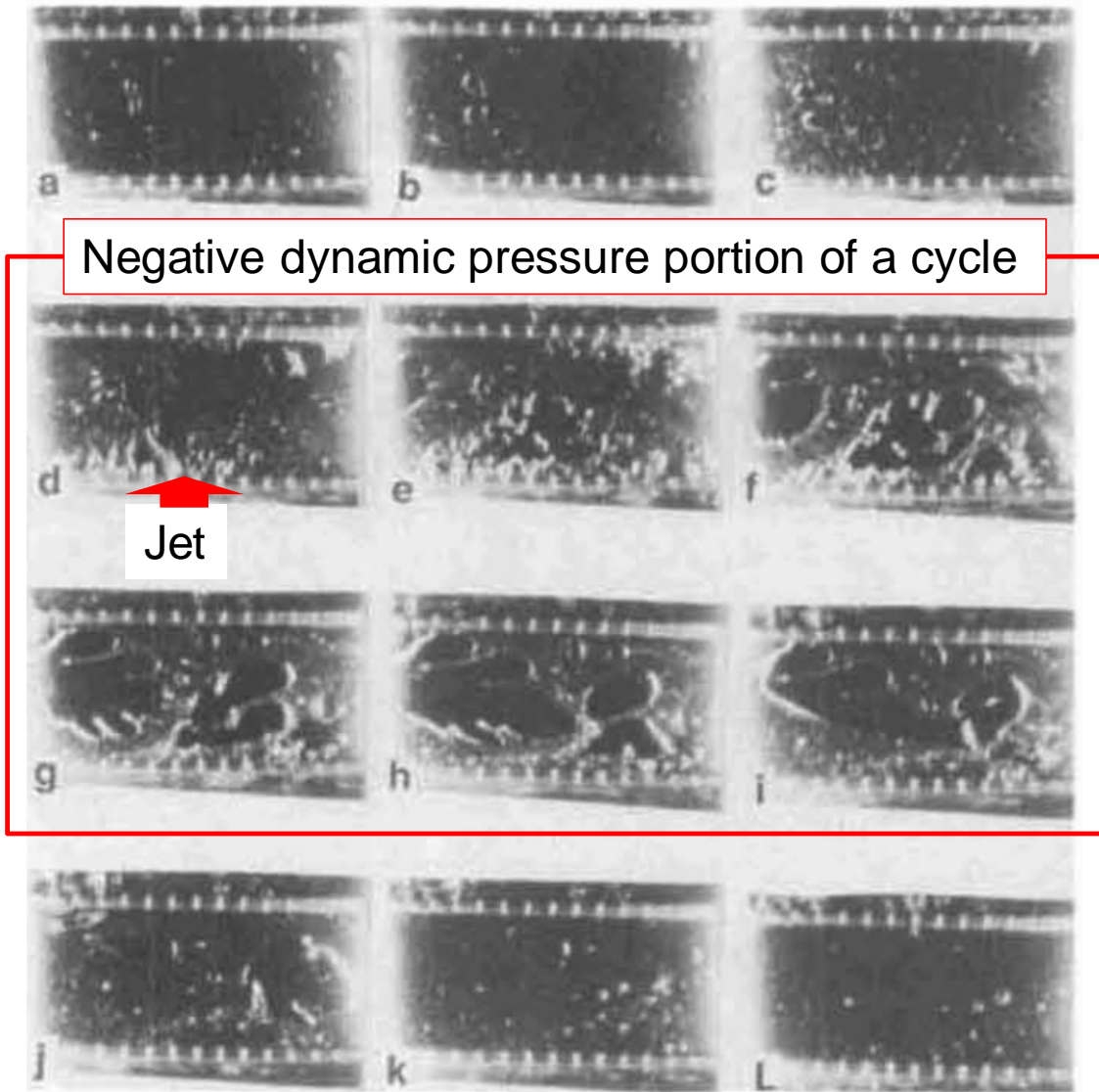


**Figure 6. Air is drawn into the damper during the negative dynamic pressure portion of a whirl cycle (d)-(i), and is swept away during the high pressure portion of the wave (a), (b), (c), (k), (l). This figure is adapted from Ref.[19].**

## CHAPTER III<sup>2</sup>

### DESCRIPTION OF THE EXPERIMENTAL FACILITY AND TEST DAMPER

This section describes the test facility and the test squeeze film damper, and included the test procedure.

#### **Test rig description**

Figure 7 depicts a photo of the SFD test rig and its major components for generating and measuring dynamic motions. The rig consists of four elastic rods supporting a bearing cartridge (BC), and a journal is rigidly mounted to a test bed. The rods provide structural stiffness ( $K_s$ ) replicating a squirrel cage. Two electromagnetic shakers orthogonally mounted shake the BC with controlled dynamic loads. A computer algorithm iteratively searches magnitudes of dynamic loads to produce a specified orbit radius ( $r$ ). When the damper whirls with the orbit radius ( $r$ ), pairs of displacement sensors, acceleration sensors, and dynamic force sensors measure the dynamic responses along  $X$  and  $Y$  axes. Simultaneously, piezoelectric dynamic pressure sensors record dynamic pressure at the film land.

This test rig is modified to test sealed ends SFDs operating (a) first with a bubbly mixture, and (b) next with PR slits open to ambient (described in Ch. VI).

In experiments with the controlled bubbly mixture, the influence of the GVF on the SFD dynamic forced performance is readily quantified. The GVF for the SFD operating

---

<sup>2</sup> Portions of this section reprinted with permission from [41] *Model and Experimental Verification of the Dynamic Forced Performance of a Tightly Sealed Squeeze Film Damper Supplied with a Bubbly Mixture* by San Andrés, L., and Koo, B., 2019, ASME J. Eng. Gas Turb. Pwr., GTP-19-1415, Copyright 2019 by ASME.

with PR slits open to ambient is quantified by comparing its dynamic forced performance against that of the SFD operating with a bubbly mixture.

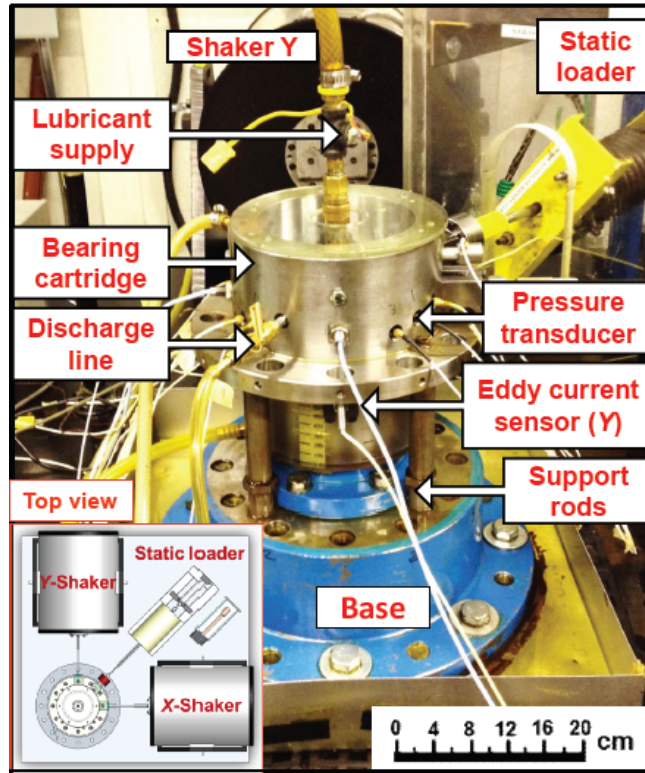


**Figure 7. Photograph of SFD test rig with shakers and sensors adapted from Ref.[34].**

**Bubbly mixture tests.** The computational analysis aims to model accurately the physical behavior of (sealed ends) SFDs operating with a bubbly mixture and hence, it is vital to produce experimental data appropriate for the model validation. If the validation succeeds, the model could be extended to predict the performance of SFDs operating with natural air ingestion. To this end, the following describes a test rig and operating procedure to deliver the test data necessary for validation.

Two important aspects are relevant to the design and realization of the experiments. One is to establish the means and procedure for making bubbly mixtures of quantifiable (known) gas content, and the other aspect is a practical implementation, while in operation, that prevents (any) ambient air be drawn into the film, and so that it could alter the composition of the supplied mixture. To prevent air ingestion, the first configuration has the damper submerged in an oil bath.

Figure 8 depicts a photograph of the SFD test rig and its major components for tests with bubbly mixture. Table 1 lists the damper dimensions and lubricant properties. The journal diameter  $D = 127$  mm. The film land length  $L = 25.4$  mm and the radial clearance  $c = 373 \mu\text{m}$  ( $c/D \sim 0.0029$ ).

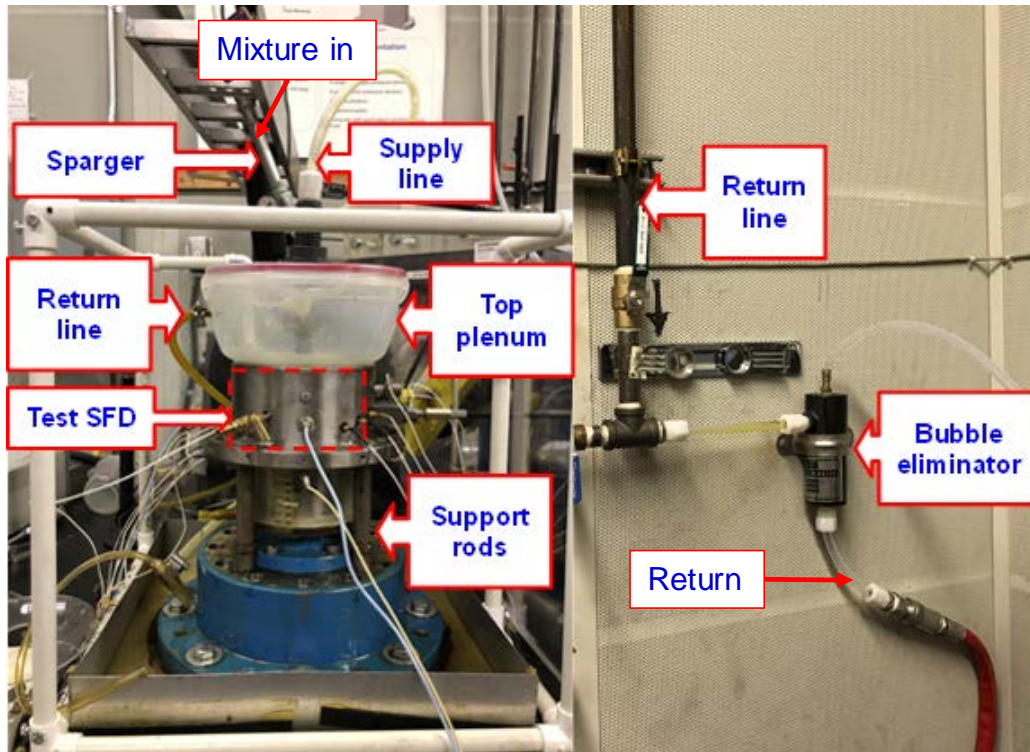


**Figure 8. Photograph of SFD test rig as lubricated with a controlled bubbly mixture.**

**Table 1. Dimensions of SFD test section and lubricant properties.<sup>3</sup>**

Journal diameter, $D$	127 mm
Axial film land length, $L$	25.4 mm
Radial clearance, $c$	373 $\mu\text{m}$
<b>Feedhole</b> orifice diameter, $\phi_{in}$	2.5 mm
Angle location, $\Theta_{in}$	45°
<b>Piston ring</b> slit area, $A_{slit}$	0.2 mm <sup>2</sup>
Angle location, $\Theta_{slit}$	135°
<b>ISO VG 2 oil</b>	
Lubricant viscosity, $\mu$	2.6 mPa-s
Lubricant density, $\rho$	799 kg/m <sup>3</sup>
Total structure mass $M_s$	24.3 kg
Bearing cartridge mass, $M_{BC}$	15.2 kg
Structural stiffness, $K_S$	3 MN/m (4MN/m with seals)
Structural damping, $C_S$	900 N-s/m
Structural quadrature stiffness, $K_O$	0.5 MN/m

Figure 9 shows a cross-section view of the test rig with the flow path into the film land and out of it. There are two distinctive axial end grooves at the top and bottom of the film land. The top groove hosts a PR, while the one at the bottom hosts an O-ring (OR). A 3.8 kW hydraulic pump delivers ISO VG2 oil from an oil tank. The measured lubricant viscosity is  $\mu = 2.6$  cP and density is  $\rho = 799$  kg/m<sup>3</sup> at supply temperature  $T_s = 23^\circ\text{C}$ . The physical properties of the used lubricant are similar to those of the oil in aircraft engines operating at a high temperature of  $T \sim 200^\circ\text{C}$ ). An air supply line draws dry air from a large pressurized tank with a regulated constant pressure. An air flowmeter measures the air volumetric flowrate at a standard condition. An oil turbine

<sup>3</sup> The sponsor selected the damper radial clearance. The loss coefficients for both the feed orifice and the PR slit are empirically estimated from static flow measurements conducted with the system lubricated with just oil.

flowmeter records oil volumetric flowrate. Two needle valves at each supply line control the inlet flow rates to determine a set inlet GVF ( $\beta_s$ ),

$$\beta_s = \frac{Q_{g(P_s)}}{Q_l + Q_{g(P_s)}} \quad (43)$$

where  $Q_l$  is the liquid volume flow rate and  $Q_{g(P_s)} = \frac{\dot{m}_g}{\rho_{(P_s)}}$  is the gas (air) volume flow rate extracted from the recorded mass flow rate ( $\dot{m}_g$ ) and the air density at the supply pressure  $\rho_{(P_s)}$ .

The two fluid streams merge into a larger component with a pore size of 2 mm to mix the fluids in homogenous form. The mixed bubbly mixture flows thru one feed hole ( $\phi_{in} = 2.5$  mm) at the bottom of the film land and  $\Theta_{in} = 45^\circ$ . The mixture lubricates the film land and exits thru a PR slit, abutted end of PR and located at  $\Theta_{slit} = 135^\circ$ . Note the OR effectively seals the film land and hence, there is artificially no leakage. A plastic reservoir with its volume of 4.4 liter accumulates the exit flow above the journal. A 750 watt return pump sucks the mixture from the top plenum while a pressure regulator maintains the pressure inside of the plenum as ambient. A bubble eliminator removes air content in the mixture, and then a pure oil returns to the oil tank.

The experiments called for dynamic load measurements to be conducted over a range of lubricant supply pressures ( $P_s$ ), from 2.1 to 6.2 bar(g), with a constant increment of 0.7 bar, and with air in oil mixtures of increasing gas content to GVF = 0.5, in steps of 0.1. Table 2 sums for various test conditions, the supply pressure and the exit bubbly

mixture GVF as well as the gas mass fraction,  $GMF = \frac{\dot{m}_g}{\dot{m}_g + \rho_{oil} Q_l} = \frac{\rho_g}{\rho_m} \beta_s$ . Notice that

the GVF at ambient pressure nearly doubles that at the supply condition, whereas the gas mass fraction remains minute since  $\rho_g < \rho_m < \rho_{oil}$ .

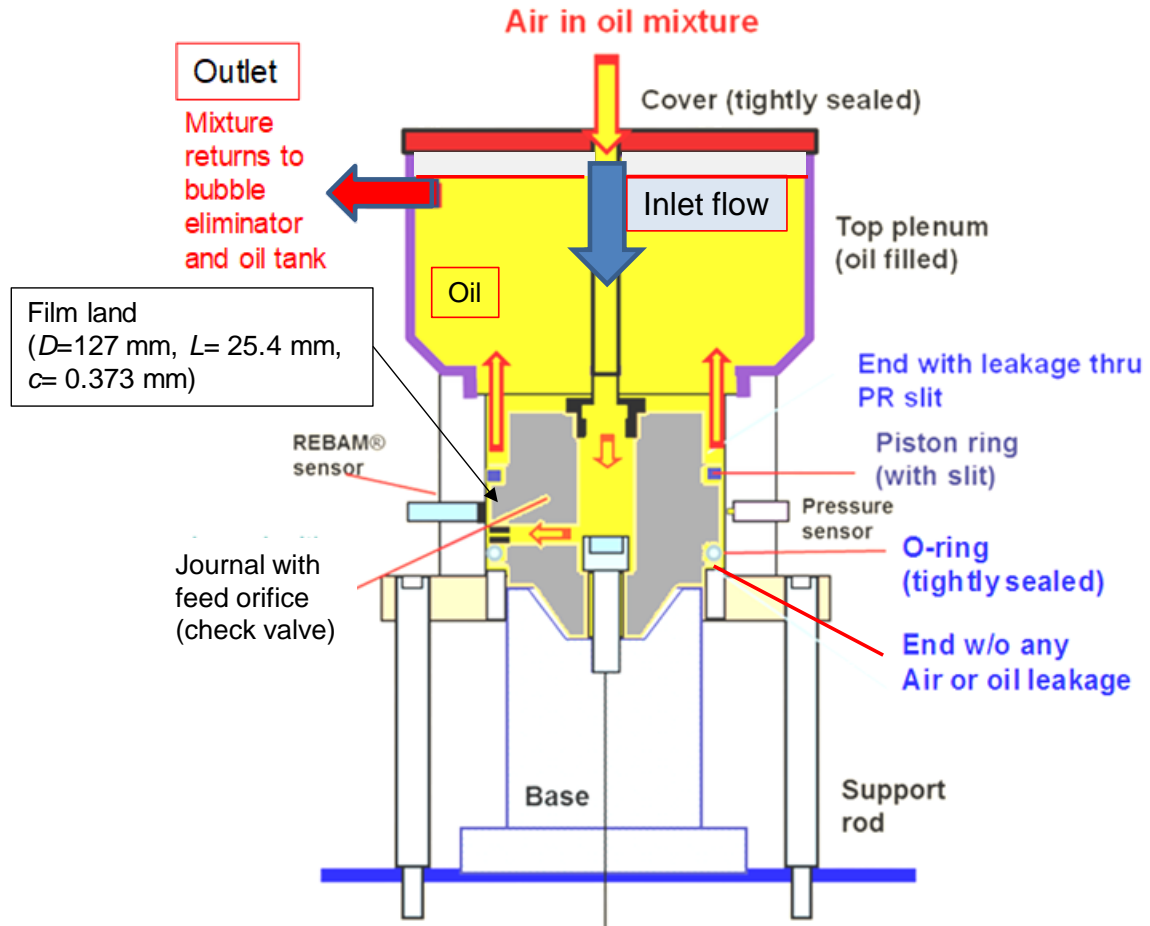


**Figure 9. Schematic cross-section view of SFD test rig with flow path for supplied bubbly mixture (not to scale).**

**Table 2. Representative gas volume fraction (GVF) in mixture and gas mass fraction (GMF) vs. supply pressure.**

$P_s$ , bar(g)	GVF at $P_s$	GVF at $P_a$	GMF $\times 10^{-3}$
6.2	0.1	0.43	1.1
	0.2	0.62	2.4
	0.3	0.74	4.2
	0.4	0.81	6.3
	0.5	0.86	9.1
4.8	0.1	0.36	0.83
	0.2	0.53	1.7
	0.3	0.67	3.1
	0.4	0.77	5.0
	0.5	0.83	7.2
2.1	0.1	0.19	0.36
	0.2	0.34	0.78
	0.3	0.46	1.3
	0.4	0.59	2.1
	0.5	0.68	3.2



## CHAPTER IV<sup>4</sup>

### TEST PROCEDURE AND FORCE COEFFICIENT IDENTIFICATION

#### **Estimation of force coefficients from measurements of force displacements**

In the experiments, the shakers deliver single frequency ( $\omega$ ) forces to produce circular orbits with amplitude<sup>5</sup>  $r=0.2 c$ . The shaker forces vector is written as

$$\mathbf{F}_{d(t)} = F_d [1 \pm i]^T e^{i\omega t} = \bar{\mathbf{F}} e^{i\omega t} \quad (44)$$

with  $i$  as the imaginary unit. The whirl frequency varies discretely from  $\omega=10\text{Hz}$  to 60 Hz. Hence, the maximum squeeze velocity  $v_s=r\omega \sim 28 \text{ mm/s}$ , and the maximum squeeze Reynolds number  $\text{Re}_s = [(\rho/\mu)\omega c^2] \sim 16$ .

The damper reaction force is modeled, in linear form, with matrices of damping and inertia force coefficients,

$$-\mathbf{F}_{SFD} = \mathbf{C}_{SFD} \dot{\mathbf{z}} + \mathbf{M}_{SFD} \ddot{\mathbf{z}} \quad (45a)$$

$$-\begin{Bmatrix} F_X \\ F_Y \end{Bmatrix}_{SFD} = \begin{bmatrix} C_{XX} & C_{XY} \\ C_{YX} & C_{YY} \end{bmatrix}_{SFD} \begin{Bmatrix} \dot{r}_X \\ \dot{r}_Y \end{Bmatrix} + \begin{bmatrix} M_{XX} & M_{XY} \\ M_{YX} & M_{YY} \end{bmatrix}_{SFD} \begin{Bmatrix} \ddot{r}_X \\ \ddot{r}_Y \end{Bmatrix} \quad (45b)$$

where  $\mathbf{z} = [r_X \quad r_Y]^T = \bar{\mathbf{z}} e^{i\omega t}$  is a vector of BC displacements. For circular centered orbits, the matrices of coefficients are not isotropic, i.e.,  $C_{XX} \neq C_{YY}$  and  $M_{XX} \neq M_{YY}$ , due to the presence of feed holes and the PR slits.

---

<sup>4</sup> Portions of this section reprinted with permission from [41] *Model and Experimental Verification of the Dynamic Forced Performance of a Tightly Sealed Squeeze Film Damper Supplied with a Bubbly Mixture* by San Andrés, L., and Koo, B., 2019, ASME J. Eng. Gas Turb. Pwr., GTP-19-1415, Copyright 2019 by ASME.

<sup>5</sup> A peak load capacity of  $\sim 4.5 \text{ kN}$  limits the range of applied dynamic load. The amplitude of BC motion (20%  $c$ ) is dictated by the sponsor application. The current system is excessively stiff due to the end seals, O-ring and PR. Hence, the test excitation frequency range is small.

Figure 10 depicts an idealized schematic view of the SFD test rig with lumped parameters such as the bearing cartridge mass ( $M_{BC}$ ), and springs ( $K$ 's) and dashpots ( $C$ 's) representing the support structure and the SFD. The dynamic loads generated by the shakers produce BC relative motions to the fixed journal. The equation of motion for the bearing with mass  $M_s$  is

$$M_s \mathbf{a} = \mathbf{F}_d + [\mathbf{F}_S + \mathbf{F}_{seals} + \mathbf{F}_{SFD}] \quad (46)$$

where the acceleration vector is  $\mathbf{a} = [a_x \quad a_y]^T = \bar{\mathbf{a}} e^{i\omega t}$ . In the experiments, the excitation forces, the BC displacements relative to the journal, and the BC accelerations are measured. That is, at frequency  $\omega$ , there are complete time records of  $\mathbf{F}_d$ ,  $\mathbf{z}$  and  $\mathbf{a}$ .

The reaction forces from the structure and the end seals (O-ring and PR) are:

$$-\mathbf{F}_S = \mathbf{K}_S \mathbf{z} + \left( \mathbf{C}_S + \frac{\mathbf{K}_{0,S}}{\omega} \right) \dot{\mathbf{z}} \quad (47)$$

$$-\mathbf{F}_{seals} \sim \mathbf{K}_{seals} \mathbf{z} + \left( \mathbf{C}_{seals} + \frac{\mathbf{K}_{0,seals}}{\omega} \right) \dot{\mathbf{z}} \quad (48)$$

with  $(\mathbf{K}, \mathbf{C})_S$ ,  $(\mathbf{K}, \mathbf{C})_{seals}$  as matrices of stiffness and damping force coefficients for the structure and for the combined effect of both end seals (O-ring and PR), respectively. Above  $\mathbf{K}_0$  is a quadrature stiffness that appears in elements showcasing either structural damping and/or dry-friction behavior, as will be evident later. For example, upon dynamic operation, one face of the piston rig slides against the groove in the journal to create a dissipative force (that is a function of the static pressure within the film).

In the frequency domain, Eq. (45) becomes

$$\begin{aligned} \bar{\mathbf{F}} - M_s \bar{\mathbf{a}} &= \left[ \mathbf{K}_L - \omega^2 \mathbf{M}_L + i(\omega \mathbf{C} + \mathbf{K}_0)_L \right] \bar{\mathbf{z}} = \mathbf{H}_L \bar{\mathbf{z}} \\ & \left[ (\mathbf{K}_S + \mathbf{K}_{seals}) - \omega^2 \mathbf{M}_{SFD} + \left( \mathbf{C}_{SFD} + \mathbf{C}_S + \mathbf{C}_{seals} + \frac{1}{\omega} \mathbf{K}_{0,seals} \right) i\omega \right] \bar{\mathbf{z}} \end{aligned} \quad (49)$$

Above define a lubricated system complex dynamic stiffness

$$\mathbf{H}_L = \left[ \mathbf{K}_L - \omega^2 \mathbf{M}_L + i(\omega \mathbf{C} + \mathbf{K}_0)_L \right] \quad (50)$$

where

$$\mathbf{K}_L = \mathbf{K}_S + \mathbf{K}_{seals}; \quad \mathbf{C}_L = \mathbf{C}_S + \mathbf{C}_{SFD} + \left( \mathbf{C} + \frac{1}{\omega} \mathbf{K}_0 \right)_{seals}; \quad \mathbf{M}_L = \mathbf{M}_{SFD} \quad (51)$$

$(\mathbf{K}, \mathbf{C}, \mathbf{M})_L$  are matrices containing the stiffness, damping and added mass coefficients of the lubricated test system.

A first set of tests without any lubricant delivers the (*dry*) structure force coefficients  $(\mathbf{K}, \mathbf{C})_S$ , listed in Table 1 and Appendix A, and the quadrature stiffness  $\mathbf{K}_{0,seals}$ , representative of the PR sliding friction. Next, multiple tests over a range of whirl frequencies, clockwise ( $+\omega$ ) and counter clockwise ( $-\omega$ ), produce enough data to determine the complex dynamic stiffness of the lubricated system.

In the identification procedure, the instrumental variable filter method [36] finds the best parameters fitting the model,  $\text{Re}(\mathbf{H}_L) \rightarrow (\mathbf{K}_L - \omega^2 \mathbf{M}_L)$  and  $\text{Im}(\mathbf{H}_L) \rightarrow (\omega \mathbf{C}_L + \mathbf{K}_{0,L})$  within a specific frequency range.

The SFD squeeze film force coefficients follow from

$$\mathbf{K}_{SFD} = \mathbf{K}_L - \mathbf{K}_S - \mathbf{K}_{seals}, \quad \mathbf{C}_{SFD} = \mathbf{C}_L - \mathbf{C}_S - \mathbf{C}_{seals}, \quad (52a)$$

$$\mathbf{M}_{SFD} = \mathbf{M}_L, \quad \mathbf{K}_{0,SFD} = \mathbf{K}_{0,S} - \mathbf{K}_{0,seals} \quad (52b)$$

Note  $\mathbf{K}_{SFD} \sim 0$  whereas  $\mathbf{K}_{0,SFD}$  roughly represents both a viscoelastic behavior from the O-ring and the sliding friction from the PR, a function of the supplied pressure.

Note the identified SFD cross-coupled force coefficients,  $(C_{XY}, C_{YX})$  and  $(M_{XY}, M_{YX})$  show magnitudes lower than 10% of the direct force coefficients magnitudes, and thus not discussed.

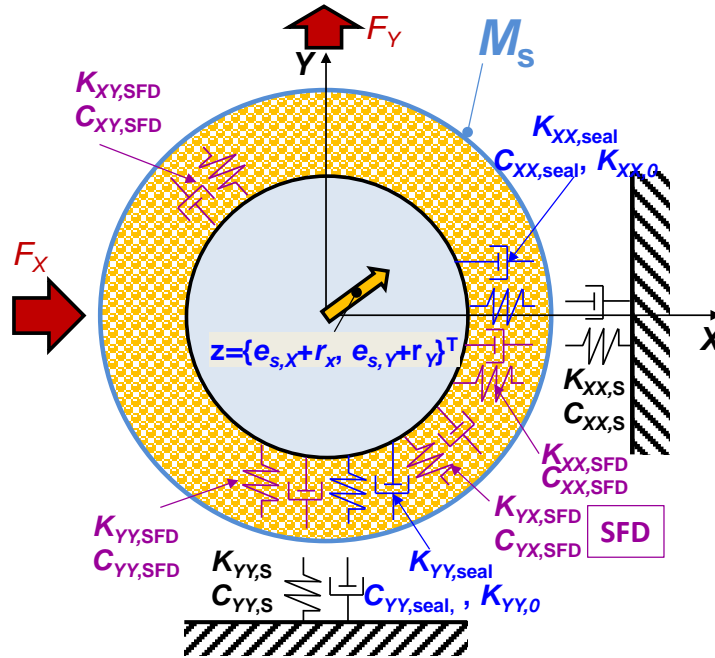


**Figure 10. Idealization of mechanical system as a point mass (bearing cartridge) and force coefficients for squeeze film, structure, and end seals.**

**Analytical force coefficients.** For a tightly sealed ends damper operating with small amplitude CCO, the SFD viscous damping ( $C^*$ ) and added mass ( $M^*$ ) coefficients are [35]

$$C^* = 12\pi\mu L \left(\frac{D}{2c}\right)^3 = 13 \text{ kN-s/m}; M^* = \rho \frac{\pi L}{c} \left(\frac{D}{2}\right)^3 = 44 \text{ kg} \quad (2)$$

These coefficients ( $C^*$ ,  $M^*$ ) are strictly valid for operation without liquid cavitation and in a physical configuration not allowing any lubricant leakage, and worse yet any air ingestion and entrapment.

In the following, the experimentally identified SFD force coefficients are normalized as  $\underline{C} = C/C^*$ ,  $\underline{M} = M/M^*$ . Note that  $\underline{C}$  and  $\underline{M} \sim 1.0$  reveal an experimentally derived coefficient perfectly agreeing with the magnitudes in Eq. (2). Normalized stiffnesses are  $\underline{K} = K/K_{S+seals}$  and  $\underline{K}_0 = K_0/K_{S+seals}$  where  $K_{S+seals} = 4 \text{ MN/m}$ . See Appendix. A for details of the identified system dry force coefficients.

## CHAPTER V<sup>6</sup>

### DYNAMIC FORCED PERFORMANCE OF A SEALED ENDS SFD SUPPLIED WITH A BUBBLY MIXTURE TEST DATA AND PREDICTION

This section delivers predictions of sealed ends SFD operating with a film filled by a bubbly mixture, benchmarked against profuse laboratory test data. The predictive models implement a Reynolds equation adapted for a bubbly mixture with a known gas volume fraction at a reference condition, namely the supply upstream of an orifice. The models include temporal fluid inertia effects, and uses physics based inlet and outlet lubricant conditions through feed holes and PR slit, respectively. The identified cross-coupled force coefficients are smaller than 10% of the direct force coefficients magnitude and thus not discussed in this dissertation.

#### **A sample of the measured complex dynamic stiffnesses for the lubricated test system of the PR-OR sealed ends SFD**

Recall Table 2 stating representative magnitudes for the mixture supply pressure and inlet GVF ( $\beta_s$ ). For the tests with  $P_s = 6.2$  bar(g), Figure 11 depicts the real and imaginary parts of the direct complex dynamic stiffnesses ( $H$ ) operating with either pure oil or with a bubbly mixture with  $\beta_s = 0.5$ . Similarly, Figure 12 displays the direct complex dynamic stiffnesses ( $H$ ) for operation with a low supply pressure,  $P_s = 2.1$  bar(g). The symbols denote the measured test system complex stiffness, and the solid and dashed lines display the physical model best curve fit to the measurements. The inset

---

<sup>6</sup> Portions of this section reprinted with permission from [41] *Model and Experimental Verification of the Dynamic Forced Performance of a Tightly Sealed Squeeze Film Damper Supplied with a Bubbly Mixture* by San Andrés, L., and Koo, B., 2019, ASME J. Eng. Gas Turb. Pwr., GTP-19-1415, Copyright 2019 by ASME.

tables list the normalized damping and inertia ( $\underline{C}, \underline{M}$ )<sub>L</sub> coefficients and the correlation coefficients ( $R^2$ ).

For both  $P_s$ , the correlation factors  $R^2 > 0.9$  show that the physical model fits well the test data. The real parts of the complex dynamic stiffness,  $\text{Re}(H_L) = (K_L - \omega^2 M_L)$ , show a significant quadratic coefficient indicating a large inertia coefficient ( $M_L \gg 0$ ). The intercept of the real part shows the lubricated system stiffness ( $K_L$ ), and which is almost identical to the one for the dry structure; that is  $K_L \sim K_S \sim 4 \text{ MN/m}$ ; thus  $K_{\text{SFD}} \sim 0$ . Recall, in classical lubrication theory, a SFD does not produce a film reaction force to a static journal displacement.

The imaginary parts of the complex dynamic stiffness,  $\text{Im}(H_L) = \omega C + K_0$ , evidence that viscous type damping is dominant. The intercept ( $K_0$ )<sub>L</sub> increases from  $\sim 1 \text{ MN/m}$  to  $> 2 \text{ MN/m}$  as the supply pressure increases from 2.1 bar(g) to 6.2 bar(g). ( $K_0$ )<sub>L</sub>  $> 1 \text{ MN/m}$  ( $\sim 0.25 K_{dry}$ ) shows a significant contribution of the end seals.

For pure oil (GVF = 0.0) with a large supply pressure, the normalized damping coefficient  $\underline{C}_{\text{SFD}}$  is  $\sim 1.0$  indicating the prediction correlates well with the measurement. The damping coefficient significantly decreases ( $\underline{C}_{\text{SFD}} < 0.7$ ) as the GVF increases from 0.0 to 0.5 (from pure oil to 50% of gas volume in the mixture). Note  $\underline{C}_{\text{SFD}}$  for either a pure oil condition or a bubbly mixture (GVF = 0.5) does not change as the supply pressure decreases. The unexpected finding points out to the mixture effective viscosity not decreasing linearly with the gas content (as theory assumes).

On the other hand, for both pressure condition ( $P_s = 6.2 \text{ bar(g)}$  or  $2.1 \text{ bar(g)}$ ), the normalized inertia coefficient  $\underline{M}_{\text{SFD}}$  for the SFD lubricated with pure oil is  $\sim 1.0$ . For tests

with a bubbly mixture ( $\beta_s = 0.5$ ),  $\underline{M}_{SFD}$  is lower than 0.5, likely due to the lower mixture density, since  $\rho_m \sim (1 - \beta) \rho_{oil}$ .

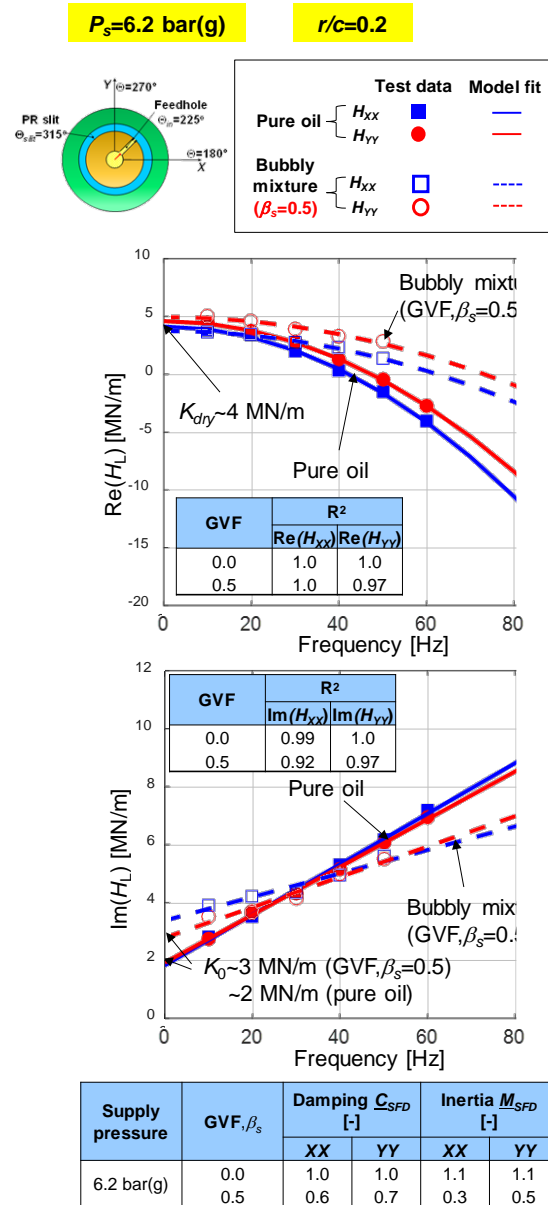
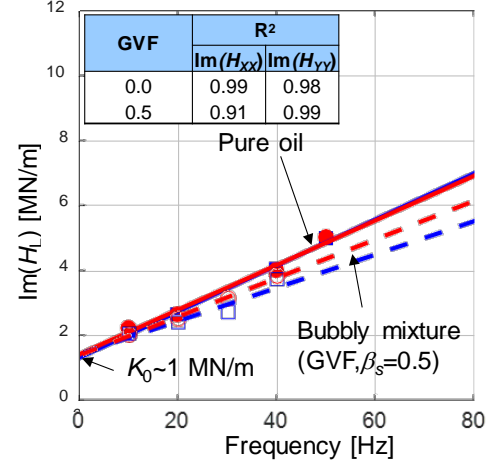
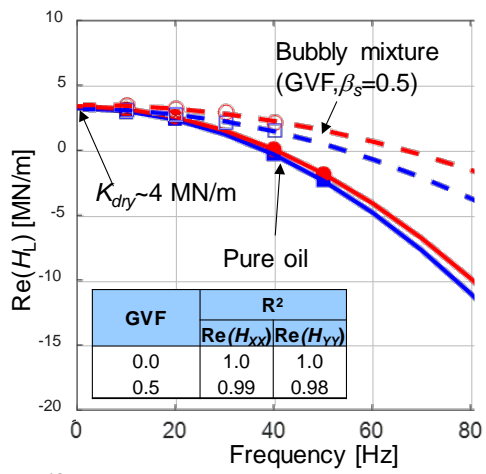
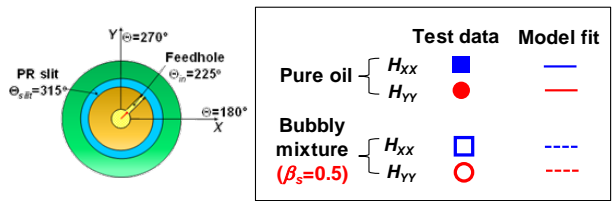


**Figure 11. SFD operating with a bubbly mixture ( $\beta_s=0.0$  and 0.5): Lubricated test system supplied with  $P_s = 6.2 \text{ bar(g)}$ : real and imaginary parts of complex dynamic stiffnesses ( $H_{XX}, H_{YY}$ )<sub>L</sub> vs. whirl frequency ( $\omega$ ). Circular centered orbits with amplitude  $r = 0.2c$  and frequency  $\omega = 10\text{-}60 \text{ Hz}$ . One feedhole at ( $\Theta_{in} = 225^\circ, z = -\frac{1}{2}L$ ) and PR slit at  $\Theta_{slit} = (315^\circ, z = \frac{1}{2}L$ ).**



$P_s=2.1$  bar(g)       $r/c=0.2$



Supply pressure	GVF, $\beta_s$	Damping $\underline{C}_{SFD}$ [-]		Inertia $\underline{M}_{SFD}$ [-]	
		XX	YY	XX	YY
2.1 bar(g)	0.0	0.8	0.8	1.0	1.1
	0.5	0.6	0.7	0.3	0.3

Figure 12. SFD operating with a bubbly mixture ( $\beta_s=0.0$  and  $0.5$ ): Lubricated test system supplied with  $P_s = 2.1$  bar(g): real and imaginary parts of complex dynamic stiffnesses ( $H_{XX}, H_{YY}$ )<sub>L</sub> vs. whirl frequency ( $\omega$ ). Circular centered orbits with amplitude  $r = 0.2c$  and frequency  $\omega = 10-60$  Hz. One feedhole at ( $\Theta_{in} = 225^\circ, z = -1/2L$ ) and PR slit at ( $\Theta_{slit} = 315^\circ, z = 1/2L$ ).

### **Force coefficients for PR-OR sealed ends SFD supplied with a bubbly mixture**

The single frequency dynamic loads produced BC orbital displacements equal to 20% of the damper radial clearance. The comprehensive test data sets were processed to deliver the SFD force coefficients, damping and inertia, as functions of the feed pressure and  $\beta_s$ . Do note the coefficients shown below are representative of the test damper dynamic performance over a certain frequency range (10 Hz-60 Hz).

Figures 13 and 14 depict as ribbon plots the experimentally derived damping  $\underline{C}_{SFD}$  and inertia  $\underline{M}_{SFD}$  coefficients versus supply pressure ( $P_s$ ) along one axis, and versus inlet GVF ( $\beta_s$ ) depicted along an orthogonal axes. The reference GVF ( $\beta_s$ ) is known (measured) and representative of the overall GVF in the film. Recall that the GVF ( $\beta$ ) varies with both time and spatial location, see Eq.(17).

Note the experimentally derived force coefficients ( $K$ ,  $C$ ,  $M$ ) have a total uncertainty (bias uncertainty + variability) of  $U_{t,K}= 6.9 \%$ ,  $U_{t,C}= 8.3 \%$ , and  $U_{t,M}=17 \%$ , respectively; see Appendix B for details. Once again, do realize the force coefficients depicted, test and model derived, are representative of operation within a certain whirl frequency range, from 10 Hz to 60 Hz.

Note that Figures 13 and 14 show the force coefficients along the  $X$  and  $Y$  directions (top and bottom). See inset graphs for a depiction of the coordinate system and the physical location of the inlet hole and PR slit. The force coefficients are expectedly not isotropic, i.e.,  $C_{XX} \neq C_{YY}$ , although the BC describes circular centered orbits.

In general, the predicted damping ( $\underline{C}_{SFD}$ ) (Fig. 13) agrees well with the test result for either a GVF ( $\beta_s$ )  $< 0.1$  or a GVF ( $\beta_s$ )  $>0.4$ . However, the experimental damping

coefficient remains nearly uconstant for GVF ( $\beta_s$ ) < 0.4; whereas the predicted  $\underline{C}_{SFD}$  gradually decreases as the GVF increases. That is, the model underpredicts (~10%) the damping coefficients for operation with a moderate GVF. As the oil supply pressure increases, the predicted damping and inertia coefficients slightly increase showing a decrease in vapor cavitation region in the film land [39-40].

Interestingly enough, the damping coefficients for the current sealed ends SFD differ in trend from those for an open ends SFD in Ref.[21] which shows  $\underline{C}_{SFD}$  linearly decreases with GVF ( $\beta_s$ ) to ~0.5. Note, however, that both the current tests and predictions produce a damping coefficient that decreases only ~20% as the inlet GVF increases to 0.5. Thus, a sealed ends SFD is more impervious to damping reduction, likely due to the substantial magnitude of the oil supply pressure ( $P_s= 2.1$  bar(g) to 6.2 bar(g)) administered during the tests.

In Fig. 14, the added mass coefficients ( $\underline{M}_{SFD}$ ) decrease quickly as the GVF ( $\beta_s$ ) increases and are independent of supply pressure  $P_s$ . Recall the density of the mixture is proportional to the GVF ( $\beta_s$ ), i.e.  $\rho_m \sim (1-\beta_s) \times \rho_{oil}$ ; hence then the quick reduction in  $\underline{M}_{SFD}$  magnitude as the gas content increases.

When GVF=0.0 (pure liquid) and  $P_s= 6.2$  bar(g), both non-dimensionalized damping and inertia coefficients experimentally derived and predicted ( $\underline{C}$ ,  $\underline{M}$ ) are nearly one, i.e., the results are close to the solution from the lubrication theory, see Eq.(2).

Note that the predictions rely on the input of empirical loss coefficients for both the lubricant feed orifice ( $C_d=1.0$ ) and the PR slit ( $C_{slit}=0.5$ ). These coefficients,  $C_d$  and  $C_{slit}$ , are taken as constant for the whole set of experiments, including those with the air in oil

mixtures. However, one must realize the named loss coefficients are a function of the flow condition, the Reynolds number, mixture composition, as well as the journal kinematics, i.e., the amplitude and frequency of whirl motion. Considering the apparent shortcomings, the agreement of the model predictions against the experimental coefficient is remarkable.

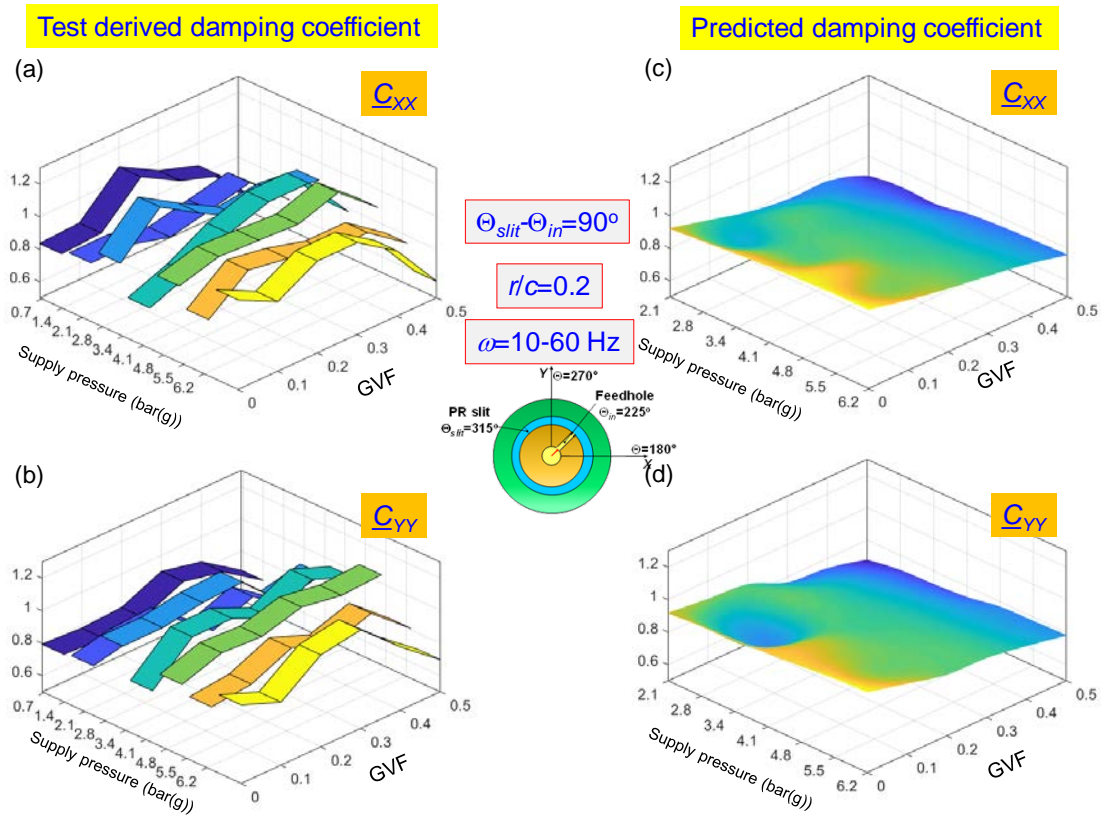


**Figure 13. SFD operating with a bubbly mixture: Experimentally derived and predicted damping coefficients ( $C_{SFD}$ ) vs. supply pressure ( $P_s$ ) and vs. inlet gas volume fraction ( $\beta_s$ ) at  $P_s$ . Top graphs show the XX-coefficient, and bottom graphs show the YY-coefficient.**

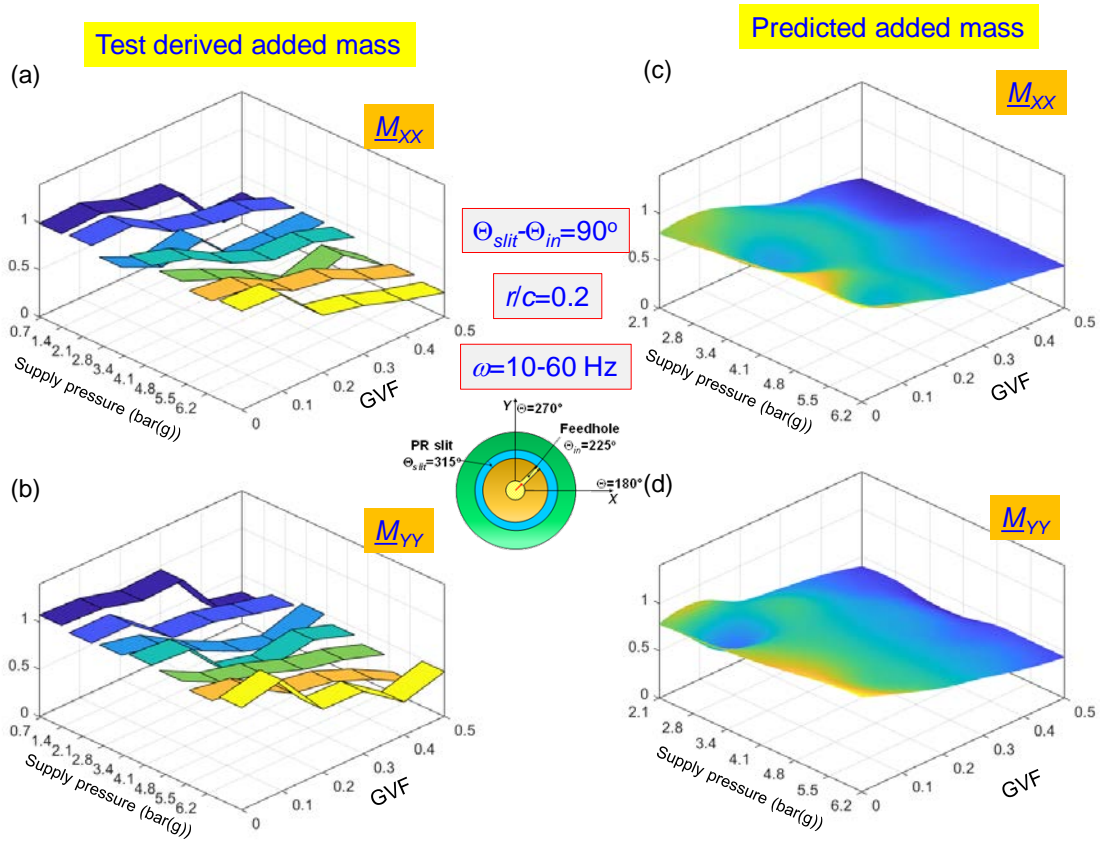


**Figure 14. SFD operating with a bubbly mixture: Experimentally derived and predicted added mass coefficients ( $\underline{M}_{SFD}$ ) vs. supply pressure ( $P_s$ ) and vs. inlet gas volume fraction ( $\beta_s$ ) at  $P_s$ . Top graphs show the XX-coefficient, and bottom graphs show the YY-coefficient.**

Figure 15 shows the test derived quadrature stiffness coefficients ( $\underline{K}_0$ )<sub>SFD</sub> vs supply pressure and vs. GVF ( $\beta_s$ ). Note ( $\underline{K}_0$ )<sub>SFD</sub> increases as the supply pressure  $P_s$  increases. The feed pressure pushes on the PR to increase the dry sliding frictional force between the ring side face and the groove in the journal. Interestingly, ( $\underline{K}_0$ )<sub>SFD</sub> also increases as the GVF increases. When air bubbles collapse, sharp pressure peaks with large magnitude appear in the squeeze film [39]. These large pressure peaks increase the frictional force between the ring side face and the groove. Ref. [39] presents the pressure

profile with the sharp pressure peaks. The normalized quadrature stiffness ( $K_\theta$ ) is large, as high as 50% of the structure stiffness. Incidentally, the large  $(K_\theta)_{SFD}$  (due to sliding friction) makes the system excessively *stiff* and demands more energy for the squeezing motion to take place. The fluid film model does not predict  $(K_\theta)_{SFD}$  as this coefficient is not related to the generation of squeeze-film pressure.

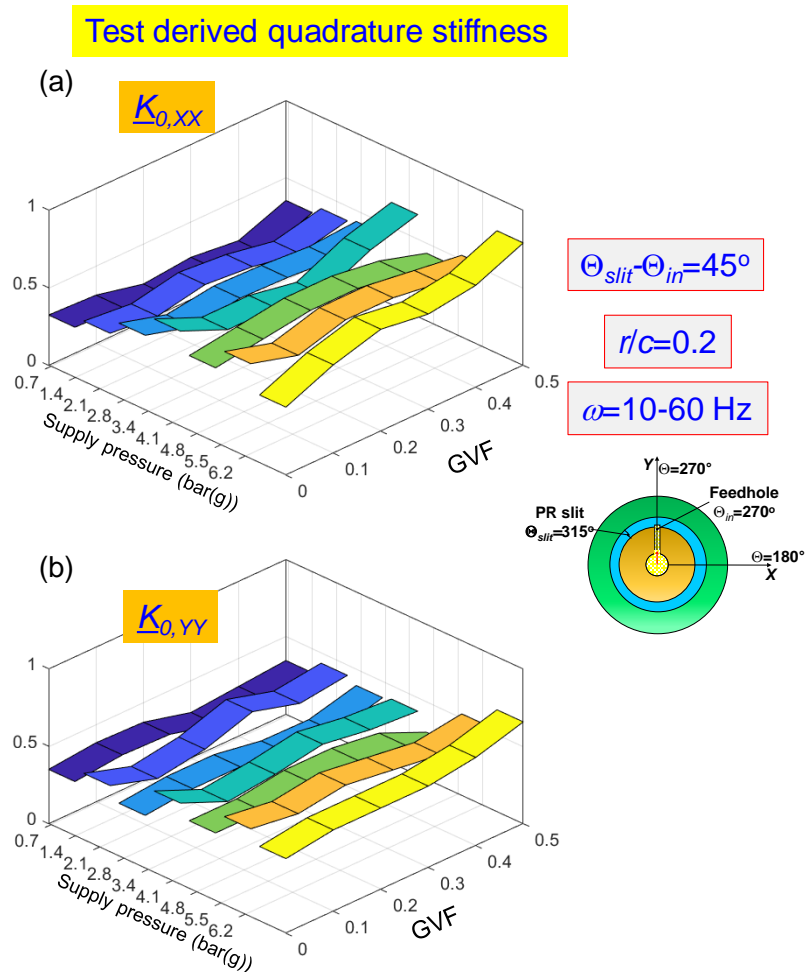


**Figure 15. SFD operating with a bubbly mixture: Experimentally derived quadrature stiffnesses ( $K_{0SFD}$ ) vs. supply pressure ( $P_s$ ) and vs. inlet gas volume fraction ( $\beta_s$ ) at  $P_s$ .**

Figure 16 depicts the direct stiffness coefficients  $\underline{K}_{SFD}$  derived from the dynamic load tests and predictions. Although the identified coefficients appear to increase as the supply pressure increases,  $\underline{K}_{SFD}$  is very small compared to the structure stiffness  $K_s$ . Both the test data and predictions show  $\underline{K}_{SFD}$  does not vary with the GVF ( $\beta_s$ ).

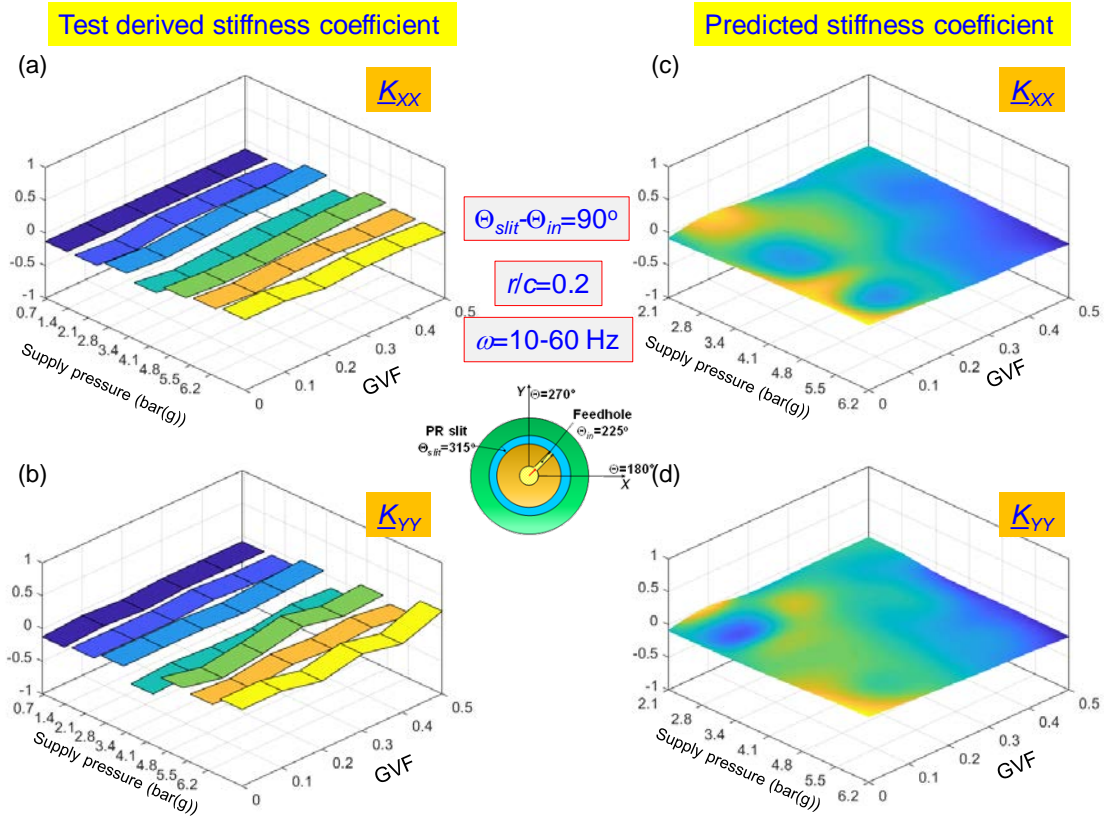


**Figure 16. Experimentally derived and predicted direct stiffnesses ( $\underline{K}_{SFD}$ ) vs. supply pressure ( $P_s$ ) and vs. inlet gas volume fraction ( $\beta_s$ ) at  $P_s$ . Top graphs show the  $XX$ -coefficient, and bottom graphs show the  $YY$ -coefficient.**

As a closure, the tests for the sealed ends SFD operating with a bubbly mixture (and submerged in an oil bath) show the effects of GVF on the damper dynamic forced performance. In general, the force coefficients ( $K$ ,  $C$ ,  $M$ ) decrease slightly as the GVF increases and/or the supply pressure decreases. In particular, the damping coefficient

$(C_{xx}, C_{yy})$  decreases only 20% while the GVF increases from 0.0 to 0.5. The results show that classical lubrication theory predicts well only if the film is lubricated with a pure liquid supplied with a large supply pressure ( $> 5 \text{ bar(g)}$ ). As  $\beta s$  increases from 0.0 to 0.5, the damping magnitude of an open ends SFD decreases  $\sim 50\%$ . [21].

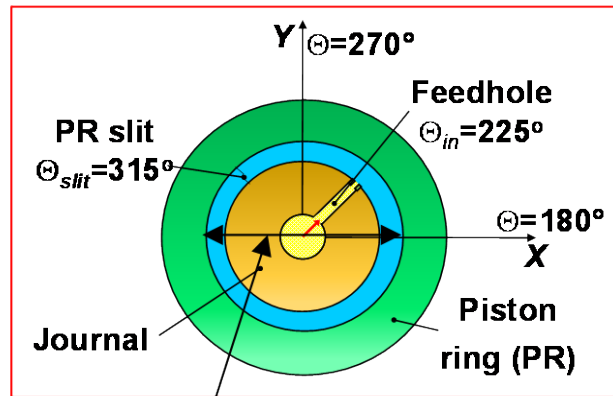
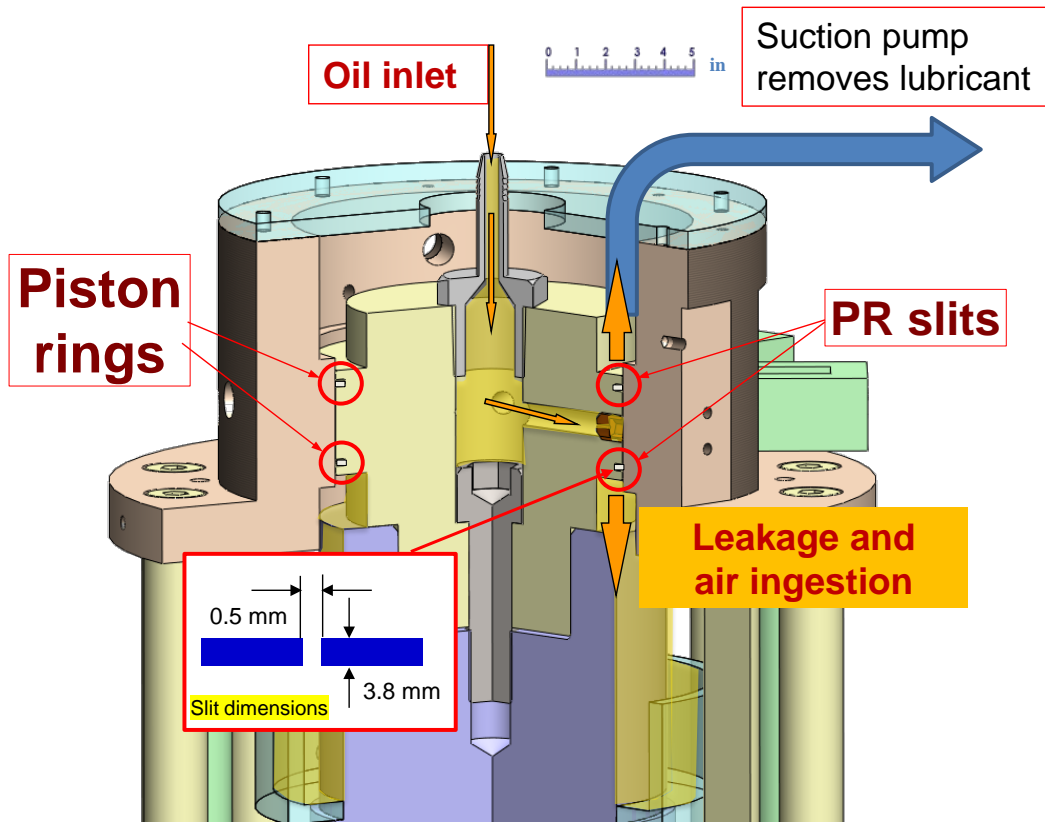


## CHAPTER VI

### DYNAMIC PERFORMANCE OF A SFD SEALED WITH PISTON RINGS AND SLITS OPEN TO AMBIENT (NATURAL AIR INGESTION)

Next in the experimented program, both axial ends of the damper film land are sealed with (identical) PRs and dynamic load tests follow. Note the PR slits being open to ambient (not a plenum) allow for natural air ingestion to occur. The PRs are fitted into the journal grooves bounding the film land. Hence, the lubricant exists through the PR slits and air can entrain (into the film land) when the squeeze-film pressure is lower than ambient.

In the experiments, pure lubricant is supplied through a feed hole ( $\phi_n = 2.5$  mm) at the middle of the film land ( $z = 0$ ,  $\Theta_{in} = 45^\circ$ ). The PR slits with a measured cross-sectional area measured ( $A_{slit}$ ) of  $2 \text{ mm}^2$  are  $90^\circ$  away from the feedhole ( $\Theta_{slit} = 135^\circ$ ). Both the feedhole and PR slit sizes are measured by a caliper with a bias uncertainty of  $\pm 0.01$  mm. Lubricant exiting thru the bottom of the damper falls by gravity into a collection bucket and immediately removed to a collection sump. On the other hand, the lubricant exiting to the top side is not allowed to accumulate since a suction line immediately routes this fluid (or bubbly fluid) to a bubble eliminator and main oil sump, as shown in Figure 17 and the photograph in Figure 18.



Journal diameter  
( $D = 127 \text{ mm}$ )  
Radial film clearance  
( $c = 373 \text{ }\mu\text{m}$ )

Figure 17. Schematic view of SFD test rig configuration for tests with air ingestion.

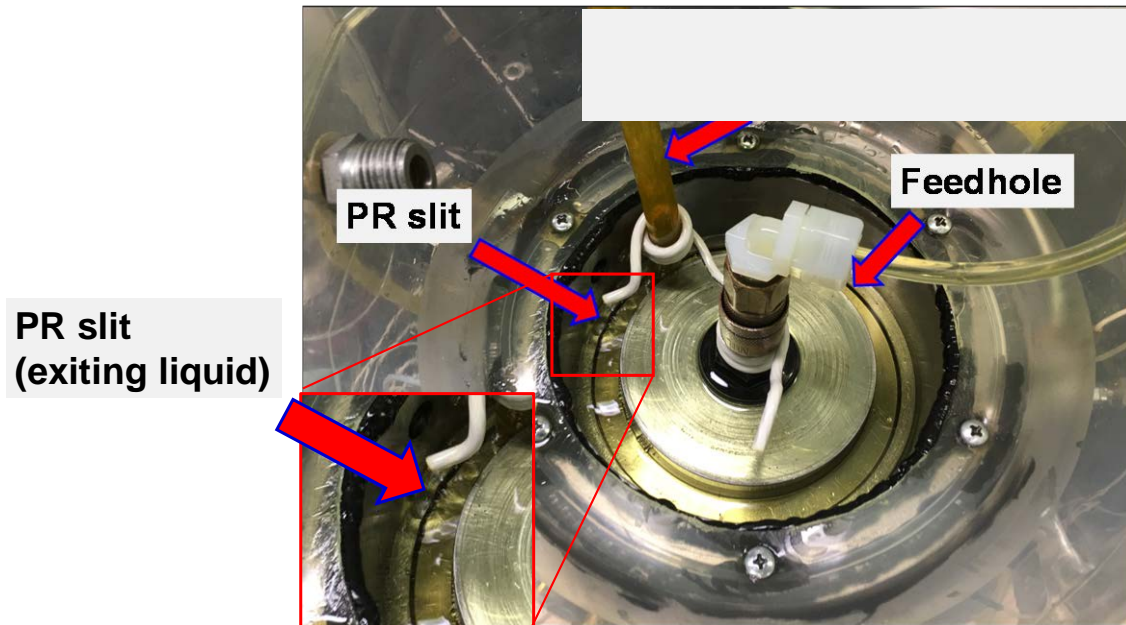


**Figure 18. Photograph of a PR sealed ends SFD operating with PR slits open to ambient.**

The single frequency dynamic load test procedure described in Ch. IV is here repeated for tests with the PR sealed ends SFD and the PR slits open to ambient. The dynamic shakers provide loads to generate a centered circular motion with an orbital displacement  $r=0.2c$ . The lubricant supply pressure  $P_s= 0.7 \text{ bar(g)}-6.2 \text{ bar(g)}$ . The identified force coefficients identified are representative of the dynamic forced performance of the test damper operating with PR slits open to ambient over a certain frequency range (40 Hz-70 Hz).

## Complex dynamic stiffness measurements of lubricated system

For tests with a sealed SFD, two PRs seal the axial ends of the journal and the PR slits open to ambient. The PR slits locate at  $\Theta_{slit} = 315^\circ$  and open to ambient. The lubricant supplies thru a feedhole located at  $\Theta_m = 225^\circ$  and  $z = 0$  (mid-plane).

For the tests with  $P_s = 0.7$  bar(g), Figure 19 depicts the lubricated system real and imaginary parts of the direct complex dynamic stiffnesses  $(H)_L$  versus whirl frequency  $(\omega)$ . The symbols denote the measured test system complex stiffness; whereas the solid lines represent the physical model best curve fit to the test data. Similarly, for tests with  $P_s = 4.1$  bar(g), Figure 20 shows both components of  $(H)_L$ . The inset tables list the correlation factors ( $R^2$ ) of the measured data to the curve fit. The test data correspond to the experiments with an orbit radius  $r=0.2c$ .

The intercepts of the real parts of  $H_L$  show the system static stiffness coefficients. For both pressure conditions, 0.7 bar(g) and 4.1 bar(g), the static stiffness is  $\sim 3.0$  MN/m. Recall the structural stiffness ( $K_S$ ) is  $\sim 3.0$  MN/m. Hence, the PR sealed ends SFD does not add to the test rig system direct stiffness. The correlation factor of  $\text{Im}(H_L) = (\omega C + K_0)$  is  $R^2 > 0.9$  although the quadrature stiffness  $(K_0)_L$  is negligible for tests of both pressure conditions. Hence, the imaginary parts of  $H_L$  evidence that a viscous type damping is dominant, i.e.,  $\text{Im}(H_L) / \omega \rightarrow C$ .

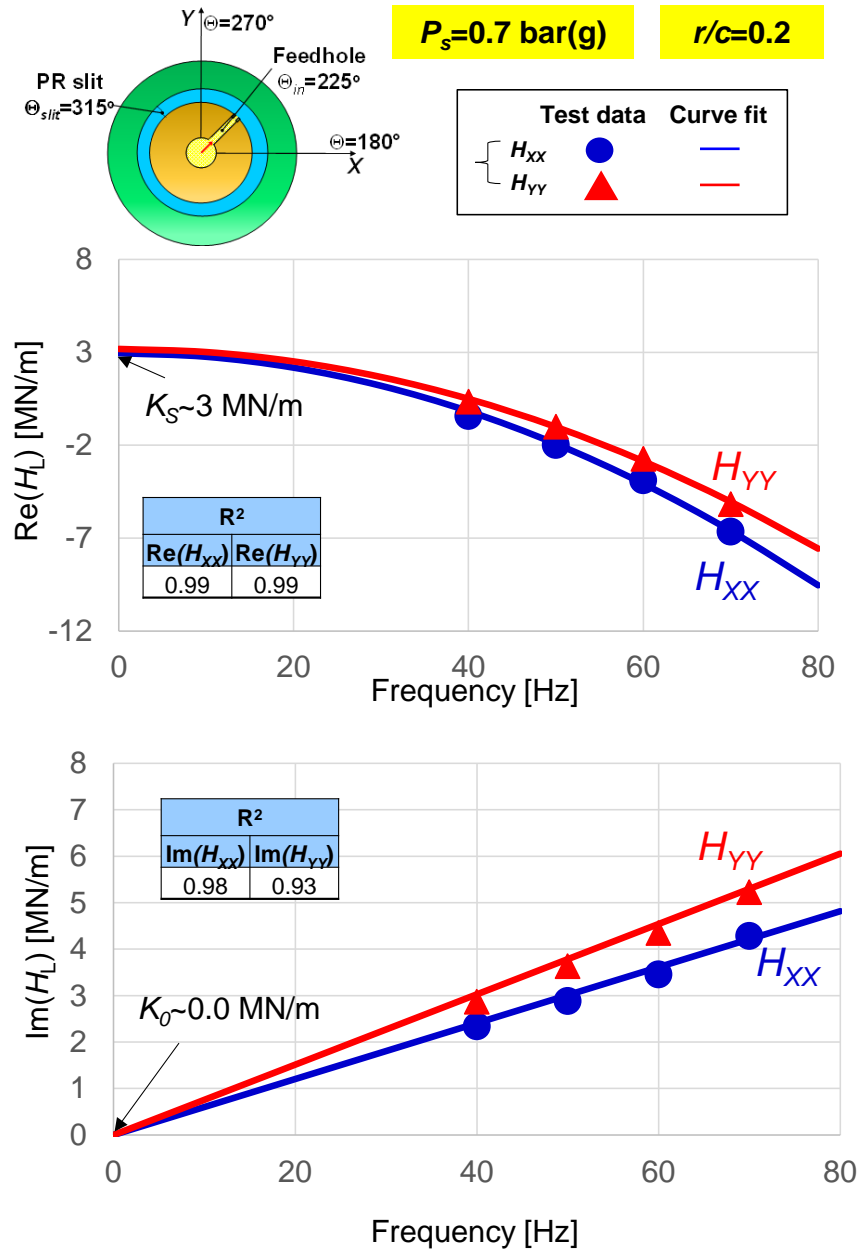


**Figure 19. PR sealed SFD with PR slits open to ambient. Real and imaginary parts of complex dynamic stiffnesses ( $H_{XX}$ ,  $H_{YY}$ )<sub>L</sub> vs. whirl frequency ( $\omega$ ). Lubricant supplied at  $P_s = 0.7 \text{ bar(g)}$ . Circular centered orbits with amplitude  $r = 0.2c$  and frequency  $\omega = 40\text{-}70 \text{ Hz}$ . One feedhole at ( $\Theta_{in} = 225^\circ$ ,  $z = 0.0$ ) and PR slits at  $\Theta_{slit} = (315^\circ$ ,  $z = \pm 1/2L$ ).**

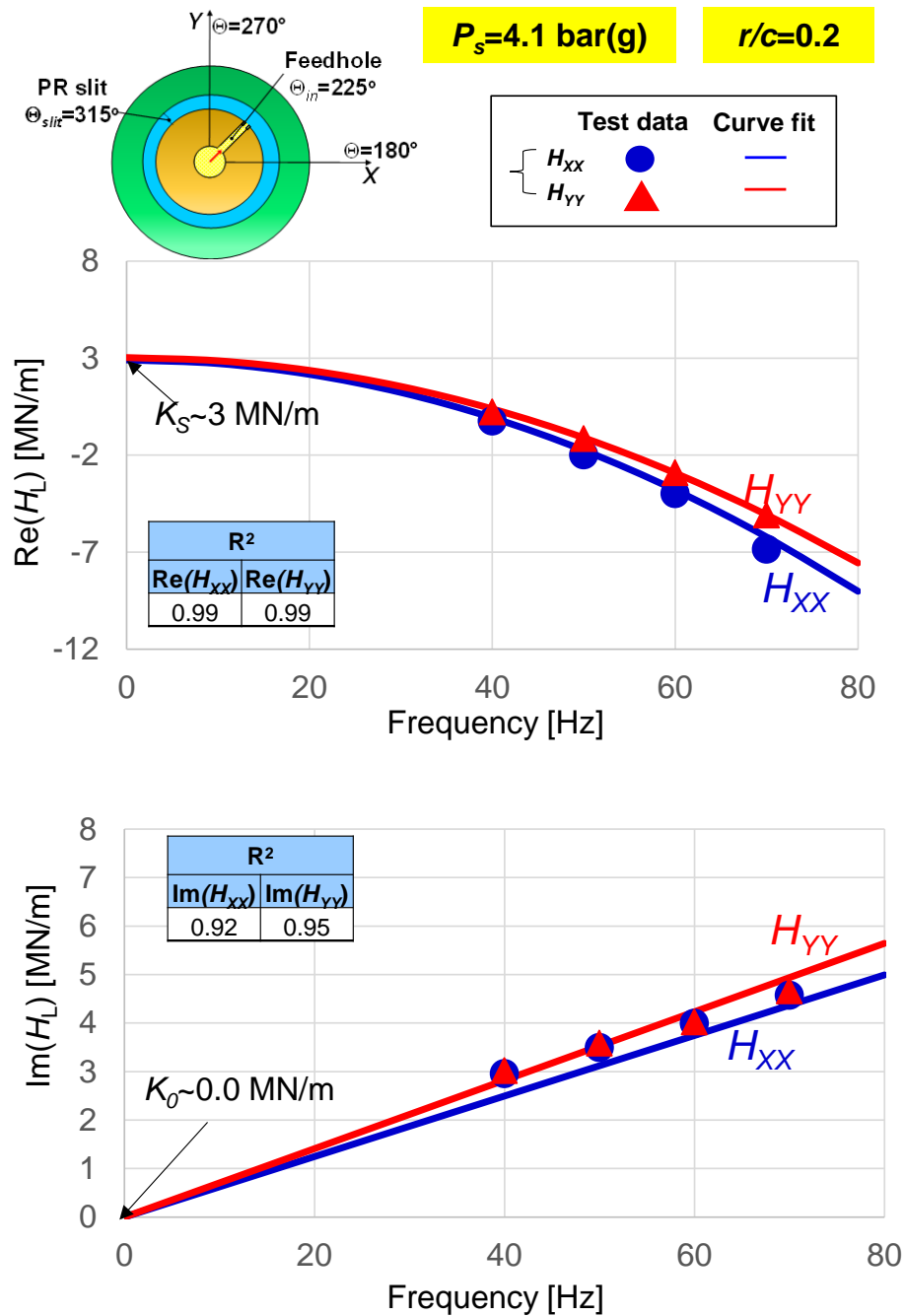


Figure 20. PR sealed SFD with PR slits open to ambient. Real and imaginary parts of complex dynamic stiffnesses ( $H_{XX}, H_{YY}$ )<sub>L</sub> vs. whirl frequency ( $\omega$ ). Lubricant supplied at  $P_s = 4.1 \text{ bar(g)}$ . Circular centered orbits with amplitude  $r = 0.2c$  and frequency  $\omega = 40\text{-}70 \text{ Hz}$ . One feedhole at ( $\Theta_{in} = 225^\circ, z = 0.0$ ) and PR slits at  $\Theta_{slit} = (315^\circ, z = \pm \frac{1}{2}L)$ .

## PR sealed SFD damping and inertia force coefficients: measurements and predictions

Over one period of whirl motion and the entire flow area, an average GVF ( $\beta_{avg}$ ) is

$$\beta_{avg} = \frac{\iiint \beta_{(\Theta,z,t)} d\Theta dz dt}{(2\pi L)T} \quad (53)$$

where  $T=2\pi/\omega$  is one period of whirl motion.

From the predictions using the SFD VOF model with natural air, Figure 21 displays as a surface plot of the time-space average GVF ( $\beta_{avg}$ ) versus oil supply pressure ( $P_s$ ) and whirl frequency ( $\omega$ ).

Figure 21 shows the space-time average GVF ( $\beta_{avg}$ ) increases as the whirl frequency increases. The average GVF is nearly zero when the supply pressure  $P_s > 3$  bar(g), i.e., a large supply pressure effectively prevents air ingestion into the SFD film land. For  $P_s=0.7$  bar(g), the GVF increases from 0.1 to 0.35 as the whirl frequency increases from 20 Hz to 70 Hz (the squeeze velocity increases from 9 mm/s to 33 mm/s).

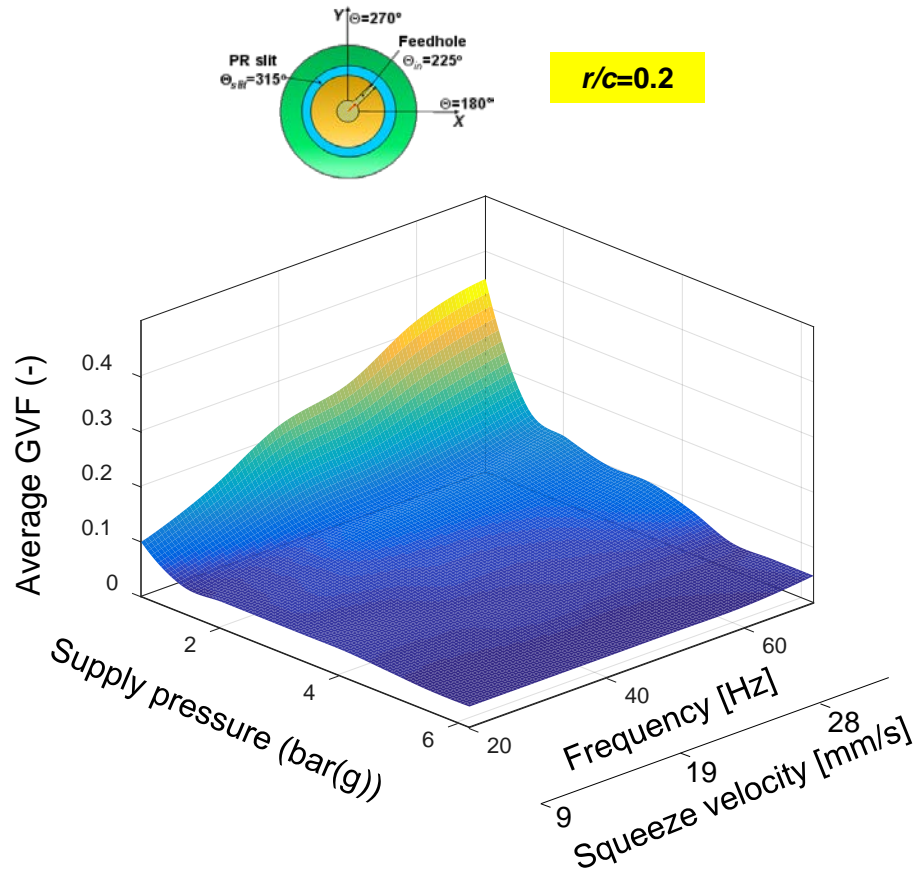


**Figure 21. PR sealed SFD with PR slits open to ambient: Predicted average GVF ( $\beta_{avg}$ ) vs. supply pressure ( $P_s$ ) and whirl frequency ( $\omega$ ) Orbit radius  $r = 0.2c$   $\Delta\Theta = \Theta_{slit} - \Theta_{in} = 90^\circ$ .**

Figure 22 depicts the experimentally derived and predicted (a) damping ( $\underline{C}$ )<sub>SFD</sub> and (b) added mass ( $\underline{M}$ )<sub>SFD</sub> coefficients versus supply pressure ( $P_s$ ). The results correspond to circular orbits with a radius  $r = 0.2c$ . The physical model uses the frequency range of 40-70 Hz for parameter identification. The maximum squeeze velocity is 33 mm/s, and the maximum Reynolds number equals 19.

The experimentally derived force coefficients include the total uncertainties of  $U_{t,K} = 5.9\%$ ,  $U_{t,C} = 8.3\%$ , and  $U_{t,M} = 17\%$ , respectively, see Appendix B. Note also the direct



stiffness and quadrature stiffness ( $K_0$ ) of the test SFD are small in comparison to the structural stiffness  $K_S= 3.0$  MN/m. Hence, the damper stiffness coefficients are not worthy of showing.

Over a period of whirl motion the feedhole and PR slits produce local pressure distortions that effect the generation of the instantaneous fluid film reaction force. The predictions shown correspond to time averages over a whole period of motion and with error bars denoting the maximum and minimum values. Note that force coefficients at one instant of time do not represent the whole dynamic performance of the SFD.

In Figure 22, the predicted damping coefficients ( $\underline{C}$ )<sub>XX,YY</sub> agree well with those experimentally derived, the maximum difference of ~10%. The predictions show the damping coefficient ( $\underline{C}$ ) increases as the supply pressure increases from 0.7 bar(g) to 2.7 bar(g) due to the decrease in GVF, see Fig. 21. Similarly, the experimentally derived normalized damping coefficient also increases from ~0.7 to ~1.0 as the supply pressure ( $P_s$ ) increases from 1.4 bar(g) to 6.2 bar(g).

Note the damping coefficients are not isotropic, i.e.,  $C_{XX} \neq C_{YY}$ , although the BC describes circular centered orbits,  $C_{XX}$  is ~10% larger than the  $C_{YY}$ . The locations of the feedhole and PR slits largely affect the dynamic forced performance of the test sealed ends SFD. The coefficients orthotropy is more pronounced than the one for the SFD lubricated with a bubbly mixture, see Fig. 13 since air content in the film land is more concentrated in the PR slit area compared to the one with a bubbly mixture.

The model under-predicts the inertia coefficients ( $M_{SFD}$ ) when compared to those experimentally derived. The maximum discrepancy is up to ~30%. The predicted

dimensionless inertia coefficients ( $\underline{M}_{XX}$ ,  $\underline{M}_{YY}$ ) increase from 0.7 to ~1.0 as the supply pressure ( $P_s$ ) increases since the average GVF ( $\beta_{avg}$ ) decreases. However, the experimentally identified inertia coefficient is nearly constant as the  $P_s$  increases. Recall the identified mass parameters have an uncertainty of 17 %.

Note a normalized force coefficient ( $\underline{C}$  or  $\underline{M}$ ) ~1.0 means the lubrication formula in Eq. (2) delivers a sound estimate of the named coefficient. For  $P_s < 3$  bar(g),  $C$  predicted by the VOF model shows a better agreement with the measurements than the one produced by the formulas in Eq. (2). The simple formula predicts accurately the inertia coefficient  $\underline{M}$  when  $P_s < 3$ bar(g) since the measured inertia coefficient is nearly constant as the supply pressure increases. For  $P_s > 3$  bar(g), the magnitudes of both experimental  $C$  and  $M$  agree with the simple formulas' predictions.

For completeness in this section, Table 3 lists the measured and predicted supplied flow rate into the sealed ends SFD for operation with supply pressure  $P_s$  from 0.7 bar(g) to 6.2 bar(g). The flow rate is representative of a static condition, i.e. without any journal whirl motion. Dynamic flow rates could not be recorded as the existing instrumentation was limited to steady state conditions.

**Table 3. Measured and predicted flowrates supplied to test SFD.**

Supply pressure (bar(g))	Flowrate (LPM)	
	Measurement	Prediction
0.7	0.31	0.27
1.4	0.42	0.38
2.8	0.62	0.53
3.4	0.66	0.59

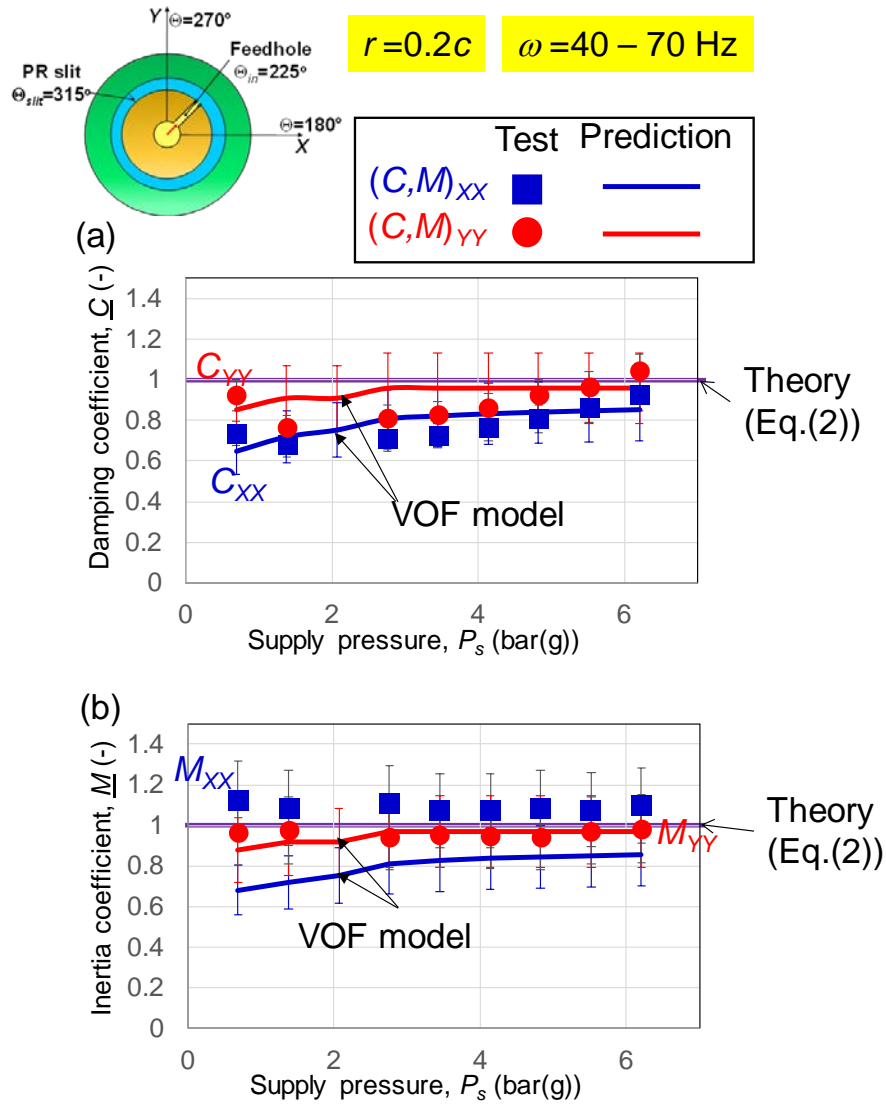


Figure 22. PR sealed SFD with PR slits open to ambient: Experimentally derived and predicted (a) damping ( $\underline{C}$ ) and (b) inertia ( $\underline{M}$ ) coefficients vs. supply pressure ( $P_s$ ). Orbit radius  $r=0.2c$  and whirl frequency  $\omega = 40-70$  Hz.  $\Delta\Theta = \Theta_{slit} - \Theta_{in} = 90^\circ$ .

## CHAPTER VII

### COMPARISONS OF MODEL PREDICTIONS FOR A SEALED ENDS SFD SUPPLIED WITH A BUBBLY MIXTURE AND A PR SEALED SFD WITH PR SLITS OPEN TO AMBIENT

The model for a SFD with a bubbly mixture requires of a known GVF at a reference condition. The bubbly mixture model takes the known GVF at the supply pressure and calculates the GVF at each film location. Thus, within the damper, the GVF decreases/increases as the film pressure increases/decreases.

On the other hand, the VOF model for a SFD (with natural ingestion) does not require of a known GVF. The damper physical geometry parameters, operating conditions (kinematics of journal), and lubricant properties determine the GVF.

#### **Note on the computational time**

Figure 23 shows a flowchart of the SFD computational model using the VOF method. First, the program iteratively calculates the pressure field by the modified Reynolds equation, Eq. (9), with given initial values (the journal location and the LVF) until the pressures at the feedhole and the PR slits are converged within 1% while satisfying the inlet/outlet orifice-like flowrates, Eqs. (14-15). From the updated pressure field, the transport, Eq. (40), produces a new LVF in the film land. The new LVF requires that the pressure field should be recalculated. The pressure and LVF repeatedly update each other until the updated pressure and LVF are within 1% as those of calculated in previous iteration. The computational code calculates the pressure field and the LVF for one period of motion and checks the inlet liquid flow thru the feedhole is equal to the

liquid flow in the mixture exit flow thru the feedhole and the PR slits. If the amounts of inlet flow and outlet liquid flow are not balanced, the algorithm repeats the calculations for one more period of whirl motion until the flows are balanced. For numerical stability, the Courant-Friedrichs-Levy number (CFL),  $N_{CFL} = U_{\theta}\Delta t / (R\Delta\theta)$  or  $U_z\Delta t / \Delta z$  should be smaller than 1 [7]. Note  $\Delta t$  is the discrete time step used in the numerical analysis.

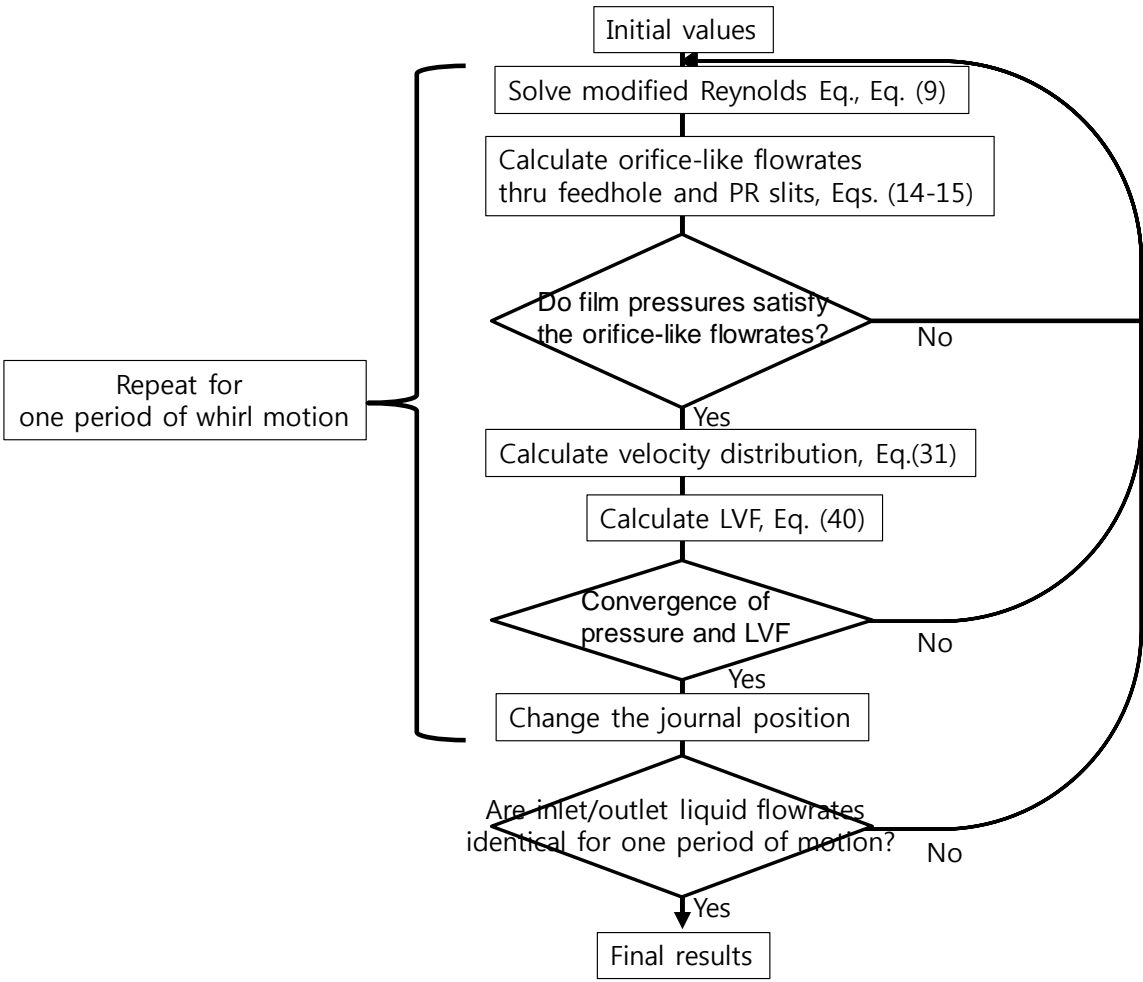


**Figure 23. Flowchart of the SFD computational model using VOF method.**

In a computer installed with an Intel i7-6700 HQ central processing unit (CPU) at 2.6 GHz and 32 GB random-access memory (RAM), the computational time to obtain a solution for either the bubbly mixture model or the VOF model is  $\sim 10$  s/period of whirl motion. However, actual convergence time for the VOF model is longer than the one for the bubbly mixture since the VOF model requires many periods of whirl motion to find a GVF condition.

As an example, the SFD case operating with  $P_s = 0.7$  bar(g),  $r = 0.2c$ , and  $\omega = 60$  Hz demands of numerical integration with no less than 50 time steps per one period of whirl motion. The overall computation time to obtain a complete solution is  $\sim 15$  min for a full period of whirl motion.

### **Comparisons of model predictions**

A PR sealed ends SFD operating with  $P_s = 0.7$  bar(g) and whirling with frequency  $\omega = 60$  Hz is used as an example to compare the predictions from a bubbly mixture model against those from the VOF model allowing natural air ingestion. The orbit radius  $r = 0.2c$ , hence the squeeze velocity  $v_s = (r\omega) = 28$  mm/s at  $\omega = 60$  Hz. The arc distance between the feedhole and the PR slit is  $90^\circ$ . The PR slit cross-sectional area is  $2 \text{ mm}^2$ , whereas the feedhole cross-sectional area is  $4.9 \text{ mm}^2$ .

Figure 24 shows the dynamic film pressure field, gas volume fraction (GVF), and the film thickness predicted (a) by the VOF model and (b) the bubbly mixture model. The graph only shows half length of the film land ( $z = 0$  to  $z = \frac{1}{2} L$ ). As an example, the

results are for a particular instant of time  $t = 3/8T$  (when the film thickness at the feedhole location is the largest. Recall  $T=2\pi/\omega$  is one time period of the whirl motion.

For the results from the VOF model, the GVF ( $\beta$ ) is a field variable varying with location and time. As expected,  $\beta$  is relatively low near the feedhole and large near the PR slit. Note the model assumes the PR slits are open to ambient and the feedhole supplies a pure lubricant.

The time-space average GVF ( $\beta_{avg}$ ), see Eq. 53, predicted from the VOF model is used as the reference GVF in the bubbly mixture model at the supply pressure condition, i.e.,  $\beta_{(\Theta_{in}, z=0, t)} = \beta_{avg}$ . In the SFD model with a bubbly mixture, the GVF increases as the film pressure decreases, recall Eq. (17). The data in Fig. 24 clearly reveals the GVF directly relates to the dynamic pressure in the film land.

For the VOF model, Figure 25 displays the mid-plane ( $z=0$ ) film pressure, mid-plane GVF, film thickness, and the film velocity at  $t=0, 1/4 T, 1/2 T,$  and  $3/4 T$  where  $T=2\pi/\omega$  is a period of whirl motion. The plot displays the pressure, film thickness and the film velocity in normalized form as  $\underline{P}=P/(3 \text{ bar(g)})$ ,  $\underline{h}=(h-c)/h_{max}$ , and  $\underline{\dot{h}}=d\underline{h}/d(\omega t)$ , respectively. The red solid line shows the film pressure, and the blue solid line shows the GVF. The purple solid and dashed lines display the film thickness ( $\underline{h}$ ) and velocity ( $\underline{\dot{h}}$ ), respectively.

In general, although the film pressure and the film velocity show a phase-lag, the film dynamic pressure increases where the film thickness decreases. Note the feedhole causes a large distortion in the film pressure. As an example, at  $t= 3/4 T$ , the maximum film pressure is nearly in-phase with the maximum film thickness. The peak-to-peak ( $pk-$

$pk$ ) film pressure at the feedhole location is much lower than those at other film circumference location as discussed in Ref. [39].

The GVF significantly fluctuates near the feedhole; whereas the GVF is nearly constant over the rest of the land area, see Fig. 25. The GVF at the feedhole is also relatively smaller than the GVF at other locations ( $\beta_s \sim 0.3$ ). The minimum GVF at the feedhole is  $< 0.2$ .

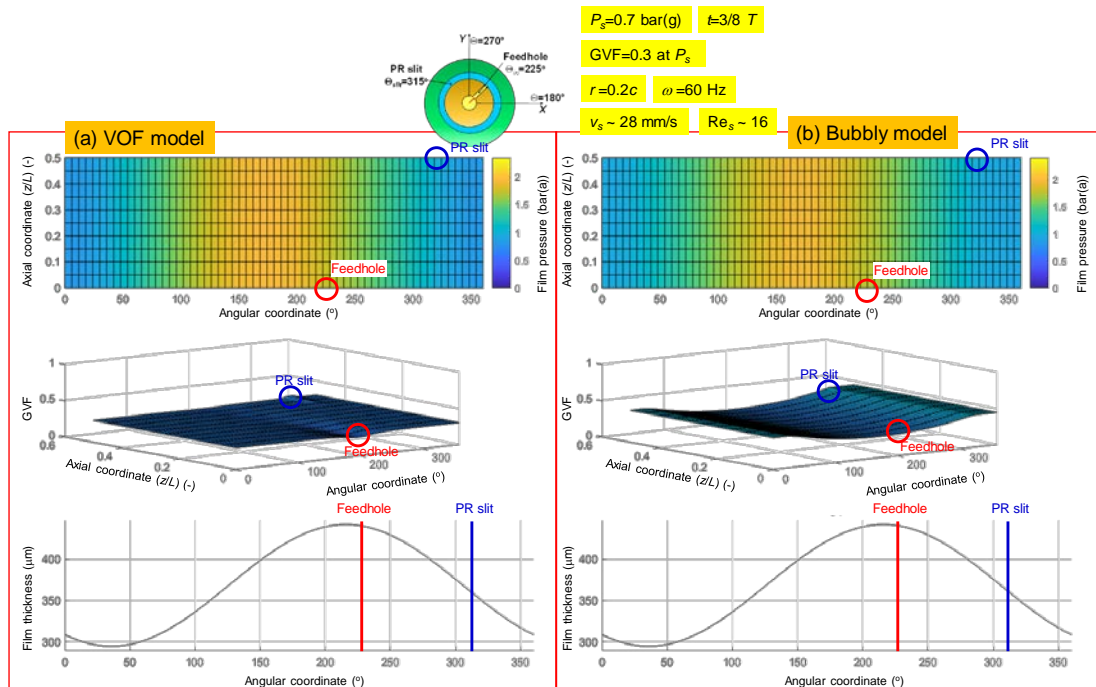


**Figure 24. Predicted film pressure field, gas volume fraction, and film thickness vs. circumferential coordinate and axial coordinate produced by (a) VOF model and (b) bubbly mixture model with  $\beta_s=0.3$ . Supply pressure  $P_s=0.7$  bar(g). Orbit radius  $r=0.2c$ . Whirl frequency  $\omega=60$ Hz.  $t=3/8T$  when the film thickness is the largest at the feedhole.**



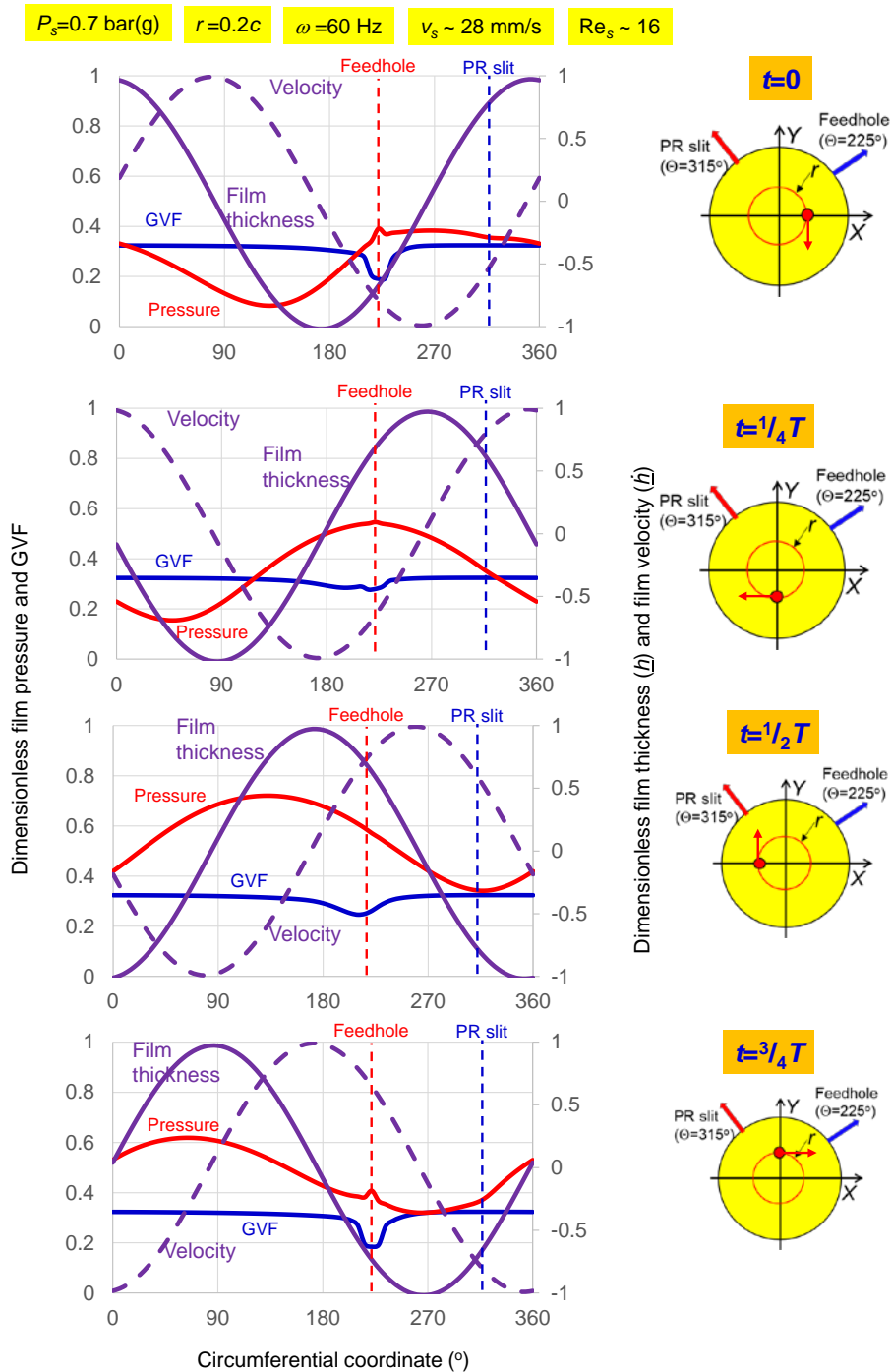


**Figure 25. VOF model predicted film pressure ( $\underline{P}$ ) and GVF at  $z=0$ , film thickness ( $\underline{h}$ ) and film velocity ( $\underline{\dot{h}}$ ) vs. circumferential coordinate ( $\Theta$ ) at  $t=0, \frac{1}{4}T, \frac{1}{2}T$ , and  $\frac{3}{4}T$ . Supply pressure  $P_s=0.7 \text{ bar(g)}$ . Orbit radius  $r=0.2c$ . Whirl frequency  $\omega=60\text{Hz}$ .  $v_s= 28 \text{ mm/s}$ .  $\Delta\Theta=\Theta_{slit}-\Theta_{in}=90^\circ$ .**

For  $P_s=0.7$  bar(g), Figure 26 displays the film dynamic pressure and the film thickness at  $\Theta=45^\circ$  versus time, dimensionless relative to  $T$ . The orbit radius  $r = 0.2c$ , and the whirl frequency  $\omega = 30$  Hz ( $v_s = 14$  mm/s). The red dots show the measured dynamic pressure; whereas the blue solid line shows predictions from the SFD VOF model, and the purple dashed line shows predictions from the bubbly mixture model with  $\beta_s=0.18$ . The predicted film dynamic pressures from both models agree well with the measured ones. Similarly, Figure 27 shows the dynamic film pressure and the film thickness at  $\Theta=45^\circ$  and for whirl frequency at  $\omega = 60$  Hz. As expected, the peak-to-peak ( $pk-pk$ ) film dynamic pressure increases as the whirl frequency increases. The measured peak film pressure is  $\sim 0.5$  bar larger than those predicted by the two models. The predictions from the VOF model are in better agreement with the measurement when compared to the ones from the bubbly mixture model with  $\beta_s=0.24$ .

The measurements at  $\omega = 30$  Hz (Fig. 26) do not show a clear indication of air ingestion. However, for  $\omega = 60$  Hz ( $v_s = 28$  mm/s), there are a few evidences indicating the presence of air content in the film land. These are high frequency pressure spikes at the peak of the dynamic pressure profile. The sealed ends SFD shows a dynamic pressure profile such that the magnitude of the positive pressure peak is larger than the one of the negative pressure peak (flat pressure zone near pressure ambient). Both the high frequency pressure spikes and the smaller negative film peak pressure at near the pressure ambient indicate the presence of air in the film land. The pressure profiles in Figs. 26 and 27 show that air content in the SFD increases as the whirl frequency ( $\omega$ ) increases.

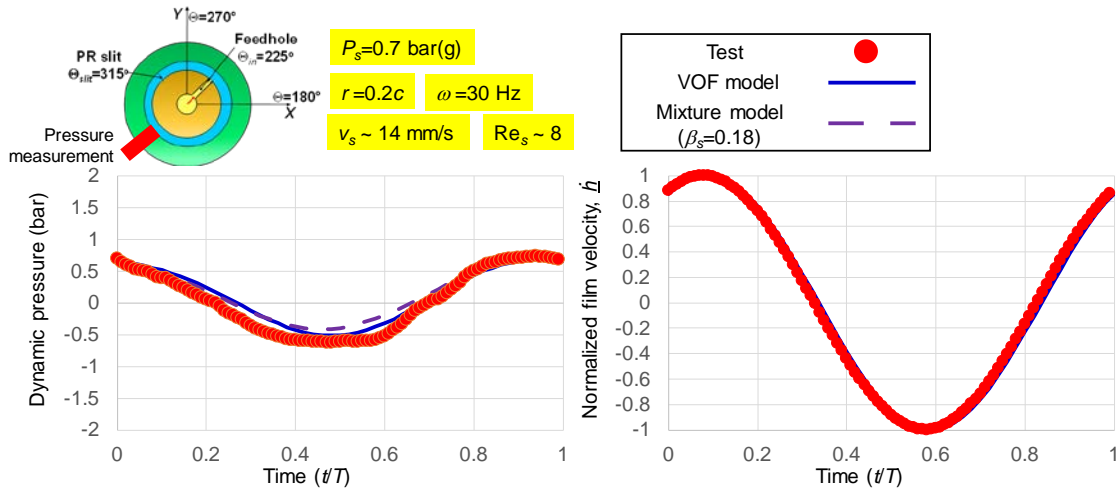


**Figure 26. Dynamic film pressure and film thickness at  $\Theta=45^\circ$  vs. time ( $t/T$ ). Supply pressure  $P_s=0.8$  bar(g). Orbit radius  $r=0.2c$ . Whirl frequency  $\omega=30$  Hz. Squeeze velocity  $v_s \sim 14$  mm/s. Reynolds #  $Re_s=8$ . Graphs include measured data and predictions from (a) VOF model and (b) bubbly mixture model.**

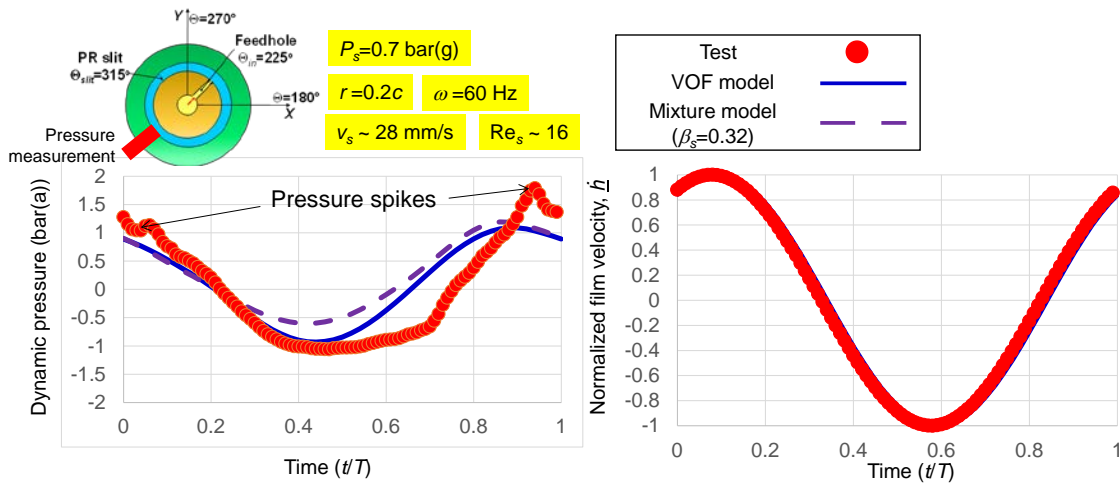


**Figure 27. Dynamic film pressure and film thickness at  $\Theta=45^\circ$  vs. time ( $t/T$ ). Supply pressure  $P_s=0.7$  bar(g). Orbit radius  $r=0.2c$ . Whirl frequency  $\omega=60$  Hz. Squeeze velocity  $v_s \sim 28$  mm/s. Reynolds #  $Re_s=16$ . Graphs include measured data and predictions from (a) VOF model and (b) bubbly mixture model.**

## CHAPTER VIII

### PARAMETERIC STUDY OF A SEALED SFD WITH ENDS OPEN TO AMBIENT.

#### PREDICTIONS FROM A VOF MODEL AND A BUBBLY MIXTURE MODEL

This chapter presents a parametric study obtaining predictions from two SFD models, namely (a) the VOF model and (b) the bubbly mixture model, and compares them. The parametric study shows the effect of damper geometry ( $D, L, c, \Delta\Theta = \Theta_{slit} - \Theta_{in}, A_{slit}$ ) and operating conditions ( $P_s, r, \omega$ ) on the film dynamic pressure and squeeze film reaction forces. The results provide a reference for engineers wishing to implement a sealed ends SFD. Table 4 lists the parameters and their range. Note the numbers in bold are the nominal operating conditions (similar to test SFD in Chapter VI).

**Table 4. SFD physical geometry parameters and operating conditions.**  
Nominal condition in **bold** face (from test SFD in Ch. VI).

Parameter	Range
Journal diameter, $D$ (mm)	76, <b>127</b> , 178
SFD axial length, $L$ (mm)	13, 19, <b>25</b>
Film clearance, $c$ ( $\mu\text{m}$ )	184, <b>373</b> , 737
Angular distance from feedhole to PR slits, $\Delta\Theta$ ( $^\circ$ )	0, <b>90</b> , 180, 270
PR slit cross-section area, $A_{slit}$ ( $\text{mm}^2$ )	1, <b>2</b> , 4
Supply pressure, $P_s$ (bar(g))	0.4, <b>0.7</b> , 1.4, 2.8
Orbit radius, $r/c$ (-)	<b>0.2</b> , 0.3, 0.4
Whirl frequency, $\omega$ (Hz)	20, 30, 40, 50, <b>60</b> , 80, 100

Figure 28 shows a schematic view of a SFD operating with circular centered orbits of amplitude  $r$  and whirl frequency  $\omega$ . The figure also depicts the tangential and radial forces.

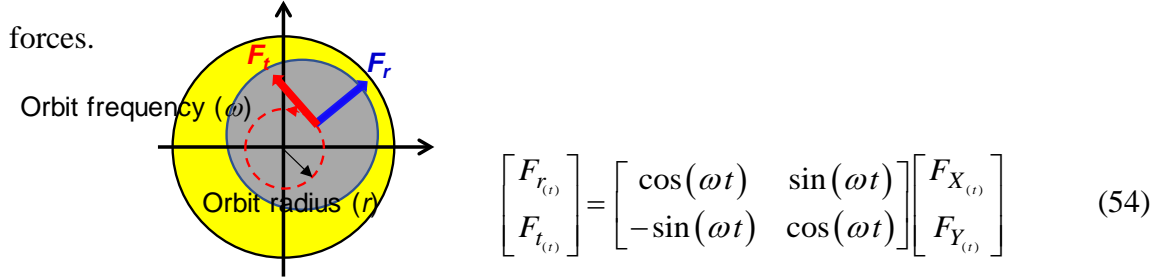


**Figure 28. SFD operating with a circular centered orbit.**

The SFD reaction force (without any cross-coupling) components are customarily expressed in terms of a damping ( $C$ ) and inertia ( $M$ ) coefficients as

$$F_t = -C v_s; F_r = -M a_s \quad (55)$$

where  $v_s = r\omega$  is the squeeze velocity and  $a_s = -r\omega^2$  is the radial acceleration. Note the tangential and radial forces oppose the journal center velocity and acceleration, respectively, as shown in Fig. 28.

Figure 29 shows an example of the predicted film reaction forces  $|F_t|$  and  $|F_r|$  versus time covering a whole period of journal whirl motion. The figure also includes the

period average of the reaction forces ( $F_i = \int F_i dt / T$ ,  $i=r, t$ ) as dashed lines. For a

centered circular orbit, the film reaction forces are generally constant. However, the reaction forces show a large distortion due to the feedhole and PR slits. When the journal is close to the feedhole location, the reaction forces are low. The bubbly mixture model



The force coefficients are normalized by Eq. (2), i.e.,  $\underline{C}_t = C_t/C^*$  and  $\underline{M}_r = M_r/M^*$ . The bars for each parameter shown represent the maximum and minimum magnitudes for  $-F_t/v_s$  and  $-F_r/a_s$  during a period of motion. Although the film reaction forces vary over one cycle of whirl motion, mechanical energy dissipates over a whole period of motion. Note however that the average force coefficients are an equivalent representation that produces the same amount of energy dissipation during a period of whirl.

The model with a bubbly mixture uses  $\beta_{(\Theta_{in}, z=0)} = \beta_{avg}$ , the average GVF estimated from a prediction obtained with the VOF model. Through all predictions shown in Figs. 30-37, the  $\beta_{avg}$  predicted from the SFD bubbly mixture model are  $\sim 0.05$  higher than those one from the VOF model. However, in general, the forces coefficients predicted from the VOF model are slightly larger than those predicted by the bubbly mixture model.

### **Effect of squeeze velocity ( $v_s = r\omega$ ) on the SFD dynamic forced performance**

To check the effect of the squeeze velocity on the SFD dynamic forced performance, the whirl frequency ( $\omega$ ) and the orbit radius ( $r$ ) are varied. The range of the squeeze velocity considered ( $v_s = r\omega$ ) is from 9 mm/s to 56 mm/s.

The data in Figs. 30-31 corresponds to orbit radius  $r=0.2c$ . The damper lubricant supply pressure  $P_s = 0.7$  bar(g). Figure 30 shows that the film  $pk-pk$  pressure, time-space average GVF ( $\beta_{avg}$ ), and the dynamic force coefficients ( $\underline{C}_t$ ,  $\underline{M}_r$ ) increase as the whirl

frequency increases. From 20 Hz to 100 Hz ( $v_s$  varies from 9 mm/s to 48 mm/s), blue square symbols present the predictions from the VOF model, and red circles display the predictions from the bubbly mixture model. The plots also include the measured film  $pk$ - $pk$  pressures shown as purple triangles. The predicted film  $pk$ - $pk$  pressures from both models agree well with the measurements.

Figure 31 displays the film  $pk$ - $pk$  pressure,  $\beta_{avg}$ , and the dynamic force coefficients ( $\underline{C}_t$ ,  $\underline{M}_r$ ) versus orbit radius ( $r$ ) varying from 10% ( $0.1c$ ) to 40% of the nominal clearance ( $0.4c$ ,  $c = 373 \mu\text{m}$ ). For  $\omega = 60$  Hz, the squeeze velocity ranges from 14 mm/s to 56 mm/s. At the nominal condition ( $r = 0.2c$ ), the average GVF ( $\beta_{avg}$ ) is 0.3.

When  $v_s < \sim 40$  mm/s, the GVF linearly increases with squeeze velocity  $v_s$ . As  $v_s$  increases, the magnitude of the  $pk$ - $pk$  pressure increases and thus air easily enters thru the PR slits. However, when  $v_s > 40$  mm/s,  $\beta_{avg}$  becomes nearly constant at 0.4. When  $\beta_{avg} \sim 0.4$ , a large amount of air content (40% air volume content) escapes thru the feedhole and PR slits and which must be equal to the inlet air flow thru the PR slits.

In Figs. 30-31, both dynamic force coefficients ( $\underline{C}_t$ ,  $\underline{M}_r$ ) decrease from 0.9 to 0.3 as the squeeze velocity ( $v_s$ ) increases from 9 mm/s to 48 mm/s due to the increase in  $\beta_{avg}$  from 0.1 to 0.4.

Shown as error bars in Figs. 30-31, both dynamic force coefficients ( $\underline{C}_t$ ,  $\underline{M}_r$ ) include variations that increase as the frequency ( $\omega$ ) or as the amplitude ( $r$ ) decreases (or as the GVF decreases). Recall the damping and inertia coefficients vary (max and min) due to the pressure distortion introduced by the feedhole and PR slits; as shown by the error bars in the graphs.



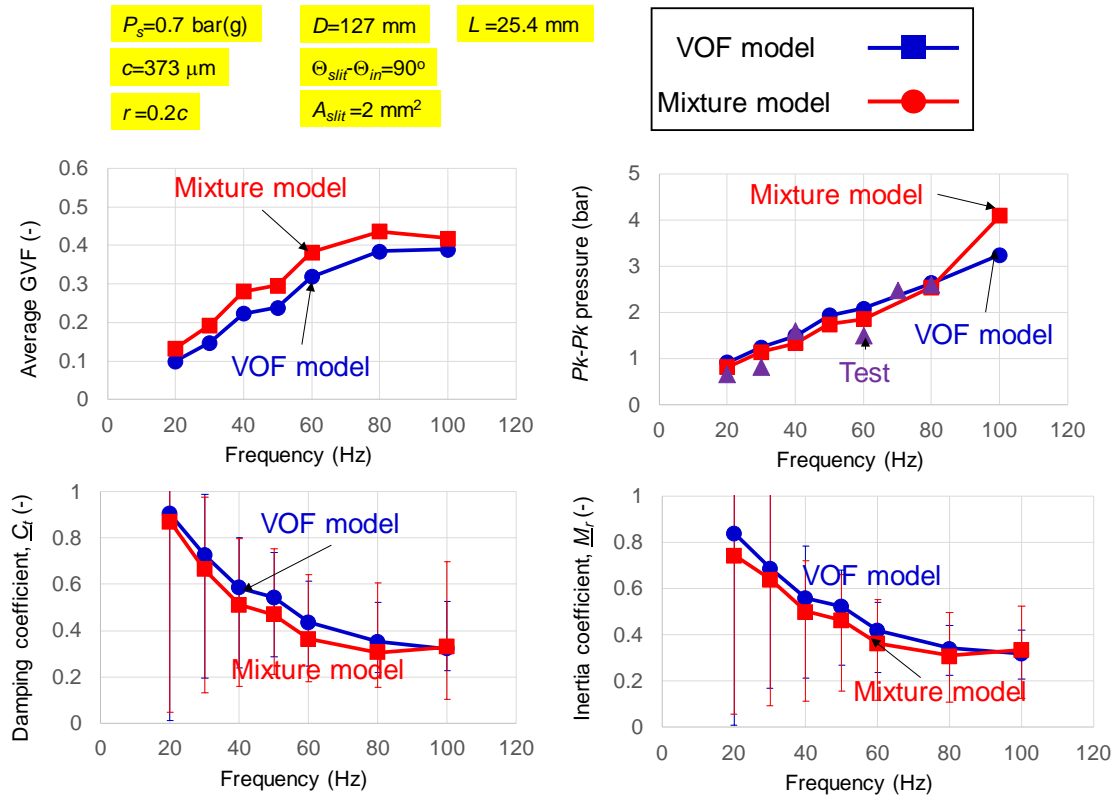


**Figure 30. Average GVF, film peak-to-peak pressure, and damping and inertia coefficients ( $\underline{C}_t$ ,  $\underline{M}_r$ ) vs. whirl frequency: Predictions from (a) VOF model and (b) bubbly mixture model.  $P_s=0.7$  bar(g),  $D=127$  mm,  $L=25.4$  mm,  $c=373$  mm,  $\Delta\Theta = \Theta_{slit} - \Theta_{in} = 90^\circ$ ,  $r=0.2c$ ,  $A_{slit}=2$  mm<sup>2</sup>.**

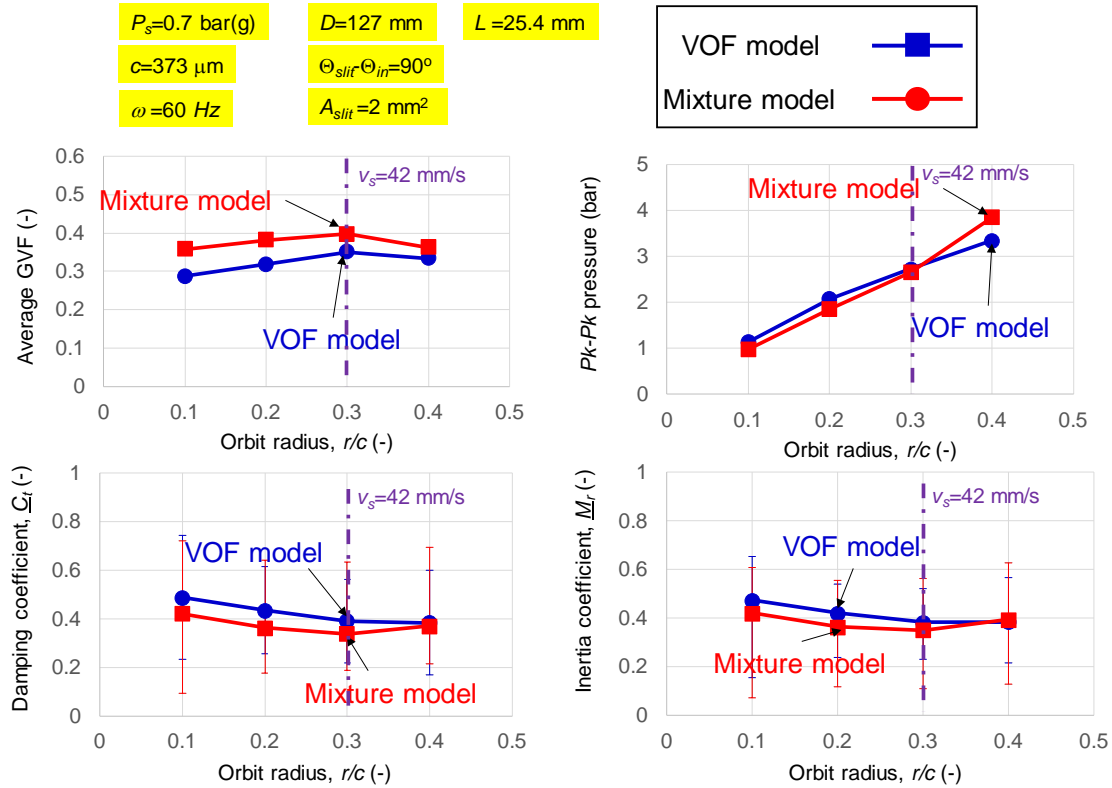


**Figure 31. Average GVF, film peak-to-peak pressure, and damping and inertia coefficients ( $\underline{C}_t$ ,  $\underline{M}_r$ ) vs. orbit radius ( $r/c$ ): Predictions from (a) VOF model and (b) bubbly mixture model.  $P_s=0.7$  bar(g),  $D=127$  mm,  $L=25.4$  mm,  $c=373$ mm,  $\Delta\Theta=90^\circ$ ,  $\omega=60$  Hz,  $A_{slit}=2$  mm<sup>2</sup>.**

### Effect of location of feedhole and PR slits on SFD dynamic forced performance

Figure 32 shows the effect of the arc distance ( $\Delta\Theta=\Theta_{slit}-\Theta_{in}$ ) between the PR slit and the feedhole on the GVF, the film  $pk-pk$  pressure, and the dynamic force coefficients ( $\underline{C}_t$ ,  $\underline{M}_r$ ). The squeeze velocity  $v_s=28$  mm/s and the Reynolds number  $Re_s=16$ .  $\beta_{avg}$  increases from 0.05 to 0.5 as the arc distance from the feedhole to PR slits ( $\Delta\Theta$ ) increases from  $0^\circ$  to  $180^\circ$ . When the PR slit and the feedhole are opposite to each other,  $\beta_{avg}$  is a maximum ( $\sim 0.5$ ). The average GVF decreases as the distance between the PR slit and the feedhole

decreases, and thus the *pk-pk* film pressure increases. Recall from Fig.25 that the film dynamic pressure at the feedhole location is lower than the one at other film land locations. A small GVF of 0.05 shows that the film pressure with a small fluctuation at the feedhole prevents air ingestion thru the PR slit when the feedhole and PR slits are in-phase (located at a same angle). Note the results with  $\Delta\Theta=90^\circ$  and  $270^\circ$  are not identical showing that the dynamic forced performance varies with the direction of whirling motion (clockwise or counterclockwise).

The variations in both dynamic force coefficients ( $\underline{C}_t$ ,  $\underline{M}_r$ ) are shown as error bars that increase with an increase in the arc distance from the feedhole to the PR slit (or as the GVF decreases).

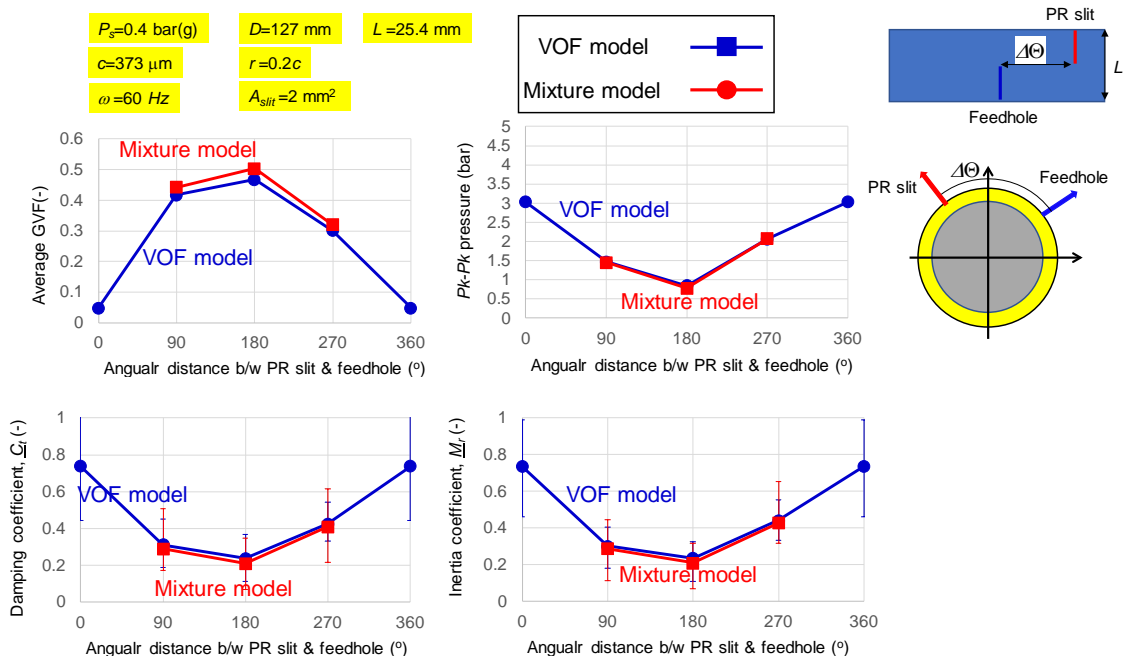


**Figure 32. Average GVF, film peak-to-peak pressure, and damping and inertia coefficients ( $\underline{C}_t$ ,  $\underline{M}_r$ ) vs. angular distance between PR slit and feedhole ( $\Delta\Theta$ ): Predictions from (a) VOF model and (b) bubbly mixture model.  $P_s=0.7$  bar(g),  $D=127$  mm,  $L=25.4$  mm,  $c=373$  mm,  $r=0.2c$ ,  $\omega=60$  Hz,  $A_{slit}=2$  mm<sup>2</sup>.**

### **Effect of SFD axial length on the SFD dynamic forced performance**

A range in SFD axial length ( $L$ ) of 13 mm ~ 25 mm is used to present the effect of the SFD axial length ( $L$ ) on the GVF and the dynamic forced performance. Figure 33 shows  $\beta_{avg}$ ,  $pk-pk$  pressure, and the dynamic force coefficients ( $\underline{C}_t$ ,  $\underline{M}_r$ ) versus damper axial length ( $L$ ). The lubricant is supplied thru the feedhole at  $\Theta=225^\circ$  and  $z=0$  and escapes thru the PR slit at  $\Theta=315^\circ$  and  $z=\pm 1/2L$  with the supply pressure  $P_s=0.7$  bar(g). The data correspond to circular orbit motions with the amplitude  $r=0.2c$  and  $\omega=60$ Hz

For the predictions from (a) the VOF model and (b) the bubbly mixture model, Figure 33 shows that the seal axial length ( $L$ ) does not significantly affect the average GVF ( $\beta_s$ ). Note the sealed ends SFD does not show a significant pressure drop across the axial coordinate; hence, an increase in  $L$  does not change the pressure at the feedhole/PR slits, and thus the GVF does not significantly change. The film  $pk-pk$  pressure also stays constant at ~ 2 bar. The dynamic force coefficients ( $\underline{C}_t$ ,  $\underline{M}_r$ ) are ~0.4 although the seal axial length increases.

The force coefficients include changes of ~25% from minimum to maximum magnitudes as the axial length ( $L$ ) increases from 13 mm to 25mm. Recall the variation in the force coefficients relates to the pressure distortion due to the feedhole and PR slits.

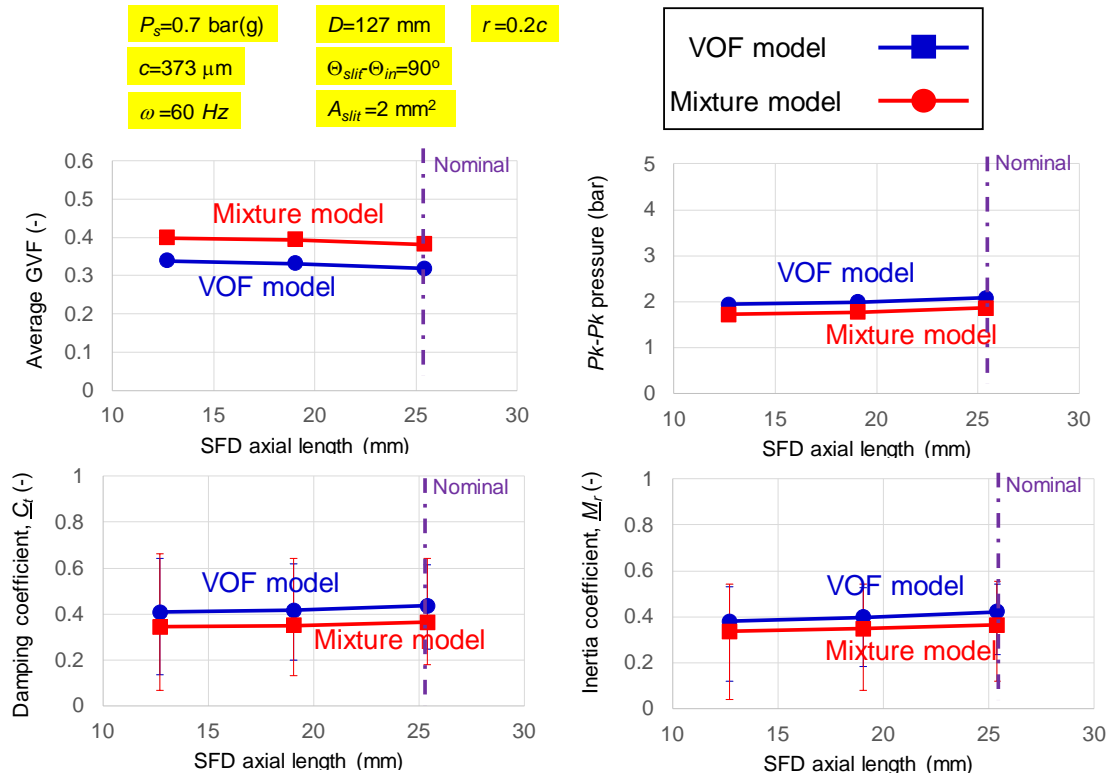


**Figure 33. Average GVF, film peak-to-peak pressure, and damping and inertia coefficients ( $\underline{C}_t$ ,  $\underline{M}_r$ ) vs. seal axial length ( $L$ ): Predictions from (a) VOF model and (b) bubbly mixture model.  $P_s=0.7 \text{ bar(g)}$ ,  $D=127 \text{ mm}$ ,  $c=373 \mu\text{m}$ ,  $r=0.2c$ ,  $\omega=60 \text{ Hz}$ ,  $\Delta\Theta=90^\circ$ ,  $A_{slit}=2 \text{ mm}^2$ .**

### Effect of SFD journal diameter on the SFD dynamic forced performance

To evaluate the effects of journal diameter on the dynamic forced performance of the PR sealed SFD ends open to ambient, the diameter of the journal increases from 76 mm to 178 mm ( $0.6D$  to  $1.4D$ ). The nominal journal diameter is 127 mm.

Figure 34 displays  $\beta_{avg}$ , the film  $pk-pk$  pressure, and the dynamic force coefficients ( $\underline{C}_t$ ,  $\underline{M}_r$ ) versus journal diameter ( $D$ ). From the VOF model, the average GVF ( $\beta_{avg}$ ) increases from 0.3 to 0.4 as  $D$  increases from  $0.6D$  to  $1.4D$ ; whereas the film  $pk-pk$  pressure increases from 1 bar to 3 bar.

The dynamic force coefficients ( $\underline{C}_t$ ,  $\underline{M}_r$ ) decrease 0.2 (from 0.5 to 0.3) as the journal diameter  $D$  increases more than two fold (from 76 mm to 178 mm). The decrease in ( $\underline{C}_t$ ,  $\underline{M}_r$ ) is due to an increase in  $\beta_{avg}$  from 0.3 to 0.4. Note that lubrication theory is strictly valid when the film land is fully wetted with a pure lubricant.

The variability in the force coefficients over one period of whirl motion, from minimum to maximum magnitudes, decreases from 0.3 to 0.2 as the journal diameter increases from 76 mm to 178 mm. The variation decreases due to the GVF increases. The air content in the film land reduces the pressure distortion.

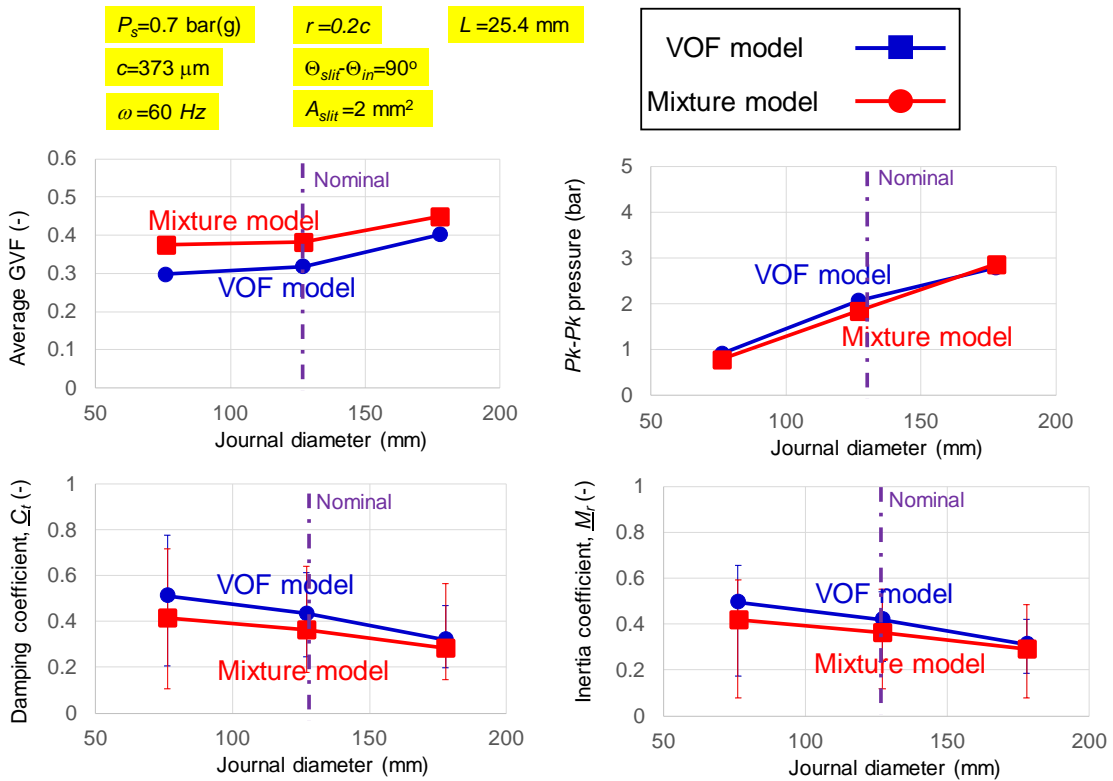


**Figure 34. Average GVF, film peak-to-peak pressure, and damping and inertia coefficients ( $\underline{C}_t$ ,  $\underline{M}_r$ ) vs. journal diameter ( $D$ ): Predictions from (a) VOF model and (b) bubbly mixture model.  $P_s=0.7$  bar(g),  $L=25.4$  mm,  $c=373$  mm,  $r=0.2c$ ,  $\omega=60$  Hz,  $\Delta\Theta=90^\circ$ ,  $A_{slit}=2$  mm<sup>2</sup>.**

### **Effect of SFD film clearance on the SFD dynamic forced performance**

The film clearance is one of the most important geometric parameters in a SFD since the clearance significantly changes the damping capability of the SFD ( $C^* \sim 1/c^3$ ). The film clearance is also easy to change since a change in a film clearance does not usually require a design change in other mechanical component in a turbomachinery system. To evaluate the effects of the damper film clearance on the PR sealed SFD dynamic forced performance, the clearance varies from 184 mm to 737 mm (from  $0.5c$  to  $2.0c$ ). Note the nominal clearance is  $c/D \sim 3/1000$ . Note the orbit radius is fixed as  $r/c=0.2$ .

Figure 35 shows the average GVF ( $\beta_{avg}$ ),  $pk-pk$  pressure, and the dynamic force coefficients ( $\underline{C}_t$ ,  $\underline{M}_r$ ) versus the film clearance ( $c$ ). The average GVF drastically decreases as the film clearance increases. As the film thickness increases, the journal kinematics squeeze motion generates a smaller dynamic film pressure [1] and thus a smaller amount of air entrains via the PR slits. Due to the decrease in the GVF, the film  $pk-pk$  pressure decreases only 0.5 bar as  $c$  increases from  $0.5c$  to  $2.0c$  (4 times of the smallest clearance); whereas the dynamic force coefficients ( $\underline{C}_t$ ,  $\underline{M}_r$ ) linearly increases from 0.2 to 0.8 (4 times). Note ( $\underline{C}_t$ ,  $\underline{M}_r$ ) are normalized by using Eq.(2) and thus the actual  $C_t$  and  $M_r$  decreases from 24.6 kN-s/m to 1.2 kN-s/m and 20 kg to 17kg, respectively. In opposition to lubrication theory formula, when PR slits allow air ingestion, a reduction in clearance does not help to increase the damping coefficient as much as the clearance does in a SFD operating with a pure lubricant.

The variability of the damping coefficients over a period of whirl motion, from minimum to maximum magnitudes, increases from 0.2 to 0.4 as the clearance grows. On

the other hand, the variability in the inertia coefficients decreases from 0.3 to 0.1 as the film clearance increases. Recall from Eq. (2) that  $C^* \sim 1/c^3$  and  $M^* \sim 1/c$ ; hence the variability in the damping is larger than the one for the inertia coefficient.

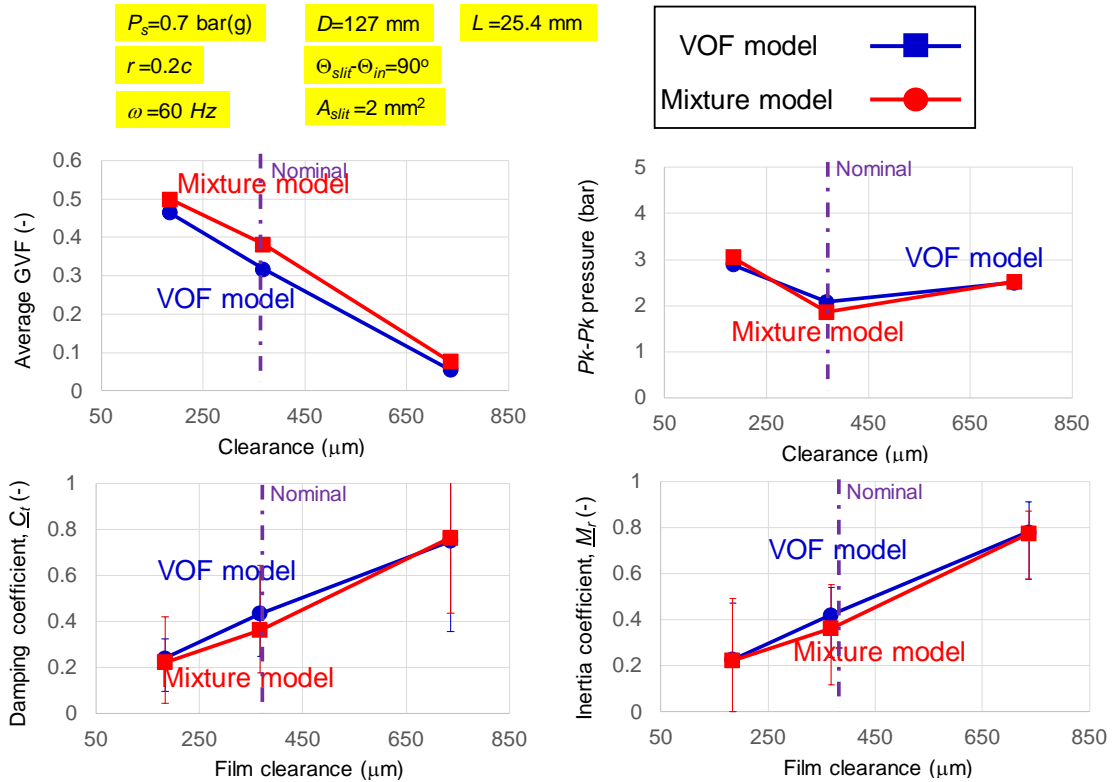


**Figure 35. Average GVF, film peak-to-peak pressure, and damping and inertia coefficients ( $\underline{C}_t$ ,  $\underline{M}_r$ ) vs. film clearance ( $c$ ): Predictions from (a) VOF model and (b) bubbly mixture model.  $P_s=0.7 \text{ bar(g)}$ ,  $D=127 \text{ mm}$ ,  $L=25.4 \text{ mm}$ ,  $r=0.2c$ ,  $\omega=60 \text{ Hz}$ ,  $\Delta\Theta=90^\circ$ ,  $A_{slit}=2 \text{ mm}^2$ .**



## Effect of SFD supply pressure on the SFD dynamic forced performance

Managing the lubricant supply pressure is one of the easiest ways to prevent air ingestion into a damper film land. In practice, an increase in lube oil supply pressure (flowrate) resolves most oil cavitation and air ingestion issues [4] in both open ends and sealed ends SFDs. In this example, the supply pressure of the SFD varies from 0.7 bar(g) to 2.8 bar(g) (4 times the nominal pressure of 0.7 bar(g)).

Figure 36 presents  $\beta_{avg}$ ,  $pk-pk$  film pressure, and the dynamic force coefficients ( $\underline{C}_t$ ,  $\underline{M}_r$ ) versus oil supply pressure for (a) the VOF model and (b) the bubbly mixture model. An increase in supply pressure from 0.7 bar(g) to 2.8 bar(g) decreases  $\beta_{avg}$  from 0.4 to 0.1. As  $\beta_{avg}$  decreases, the  $pk-pk$  film pressure increases from 1.5 bar to 3.5 bar; whereas the dynamic force coefficients ( $\underline{C}_t$ ,  $\underline{M}_r$ ) increases from 0.3 to 0.85.  $\beta_{avg}$  largely decreases as the supply pressure increases when  $P_s < 1.5$  bar(g) since the supply pressure ( $P_s$ ) is lower than half of the  $pk-pk$  pressure.

The graphs include as the error bars the variability of the force coefficients, from minimum to maximum magnitudes, within a period of whirl motion. The coefficients variability increases as the supply pressure increases (and the GVF decreases) since the pressure distortions at the feedhole location magnify. Although the variation increases, the average force coefficient ( $\underline{C}_t$ ,  $\underline{M}_r$ ) also significantly increases with  $P_s$ . Recall the ( $\underline{C}_t$ ,  $\underline{M}_r$ ) represents the dynamic performance of the SFD.

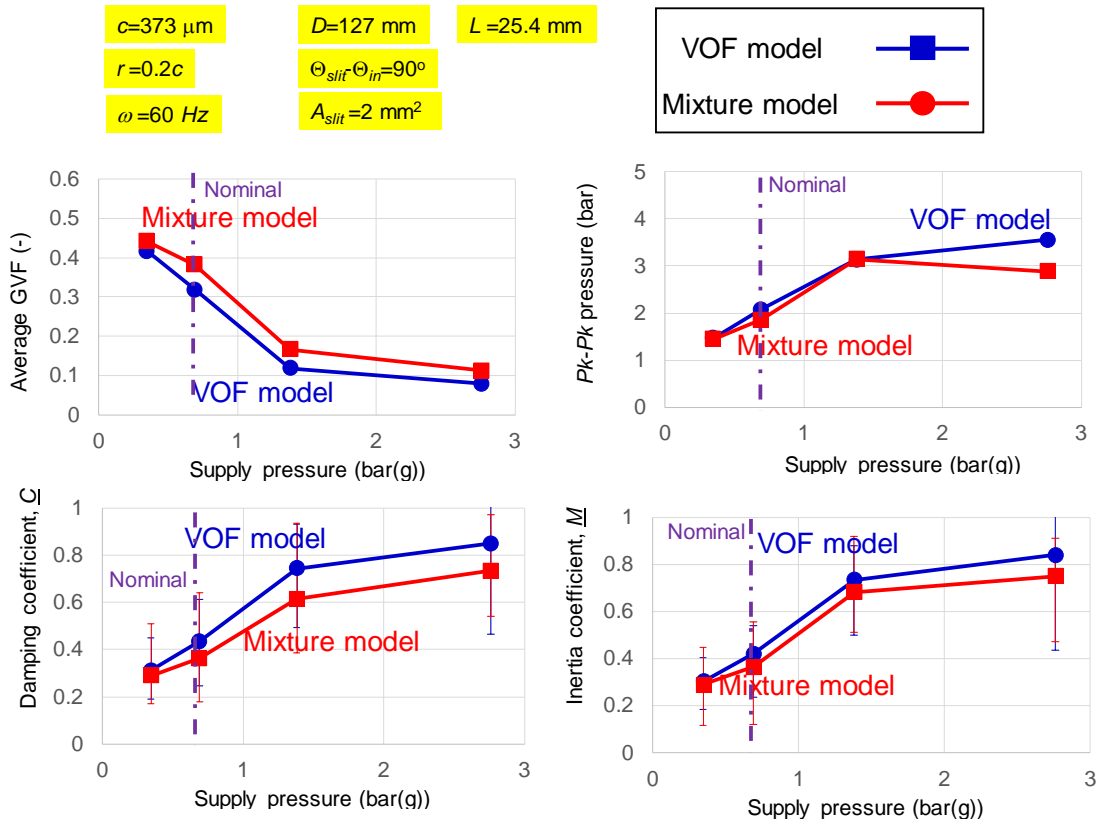


**Figure 36. Average GVF, film peak-to-peak pressure, and damping and inertia coefficients ( $\underline{C}_t$ ,  $\underline{M}_r$ ) vs. supply pressure ( $P_s$ ): Predictions from (a) VOF model and (b) bubbly mixture model.  $D=127 \text{ mm}$ ,  $L=25.4 \text{ mm}$ ,  $c=373 \text{ mm}$ ,  $r=0.2c$ ,  $\omega=60 \text{ Hz}$ ,  $\Delta\Theta=90^\circ$ ,  $A_{slit}=2 \text{ mm}^2$ .**

### **Effect of SFD PR slit area on the SFD dynamic forced performance**

A PR seal has abutted ends, named PR slits, for installation in a groove. The PR slit opens and minimizes the gap between the PR and the bearing cartridge when the PR locates in the groove. San Andrés et al. [39] present that the PR slits allow a large amount of leakage and air ingestion although the flow thru the PR slits is ignored in most predictive models. The SFD model in this dissertation includes the flow thru the PR slits. This section presents the effect of the PR slit cross-sectional area ( $1\text{mm}^2$  to  $4\text{mm}^2$ ) on the SFD dynamic forced performance. The PR slit area varies from.

Figure 37 displays the average GVF, and the film  $pk-pk$  pressure, and the film reaction forces versus the PR slit cross-sectional area ( $A_{slit}$ ). The GVF slightly increases as the PR slit area ( $A_{slit}$ ) increases; whereas the  $pk-pk$  pressure and the fluid film reaction forces slightly decrease. It shows that the PR slit area does not significantly change the dynamic performance of a PR sealed ends damper. Note the feedhole cross-sectional area is  $\sim 4.9\text{mm}^2$ , which is larger than the largest PR slit area. The effect of PR slit area on the dynamic performance of a SFD is marginal when the PR slit area is smaller than that of the feedhole area.

The variability of the force coefficients, minimum and maximum within a period of whirl motion, is nearly constant as the PR slit area increases. The area of the PR slit, within the range considered, does not affect either the film pressure or the GVF, and hence the variability remains the same.

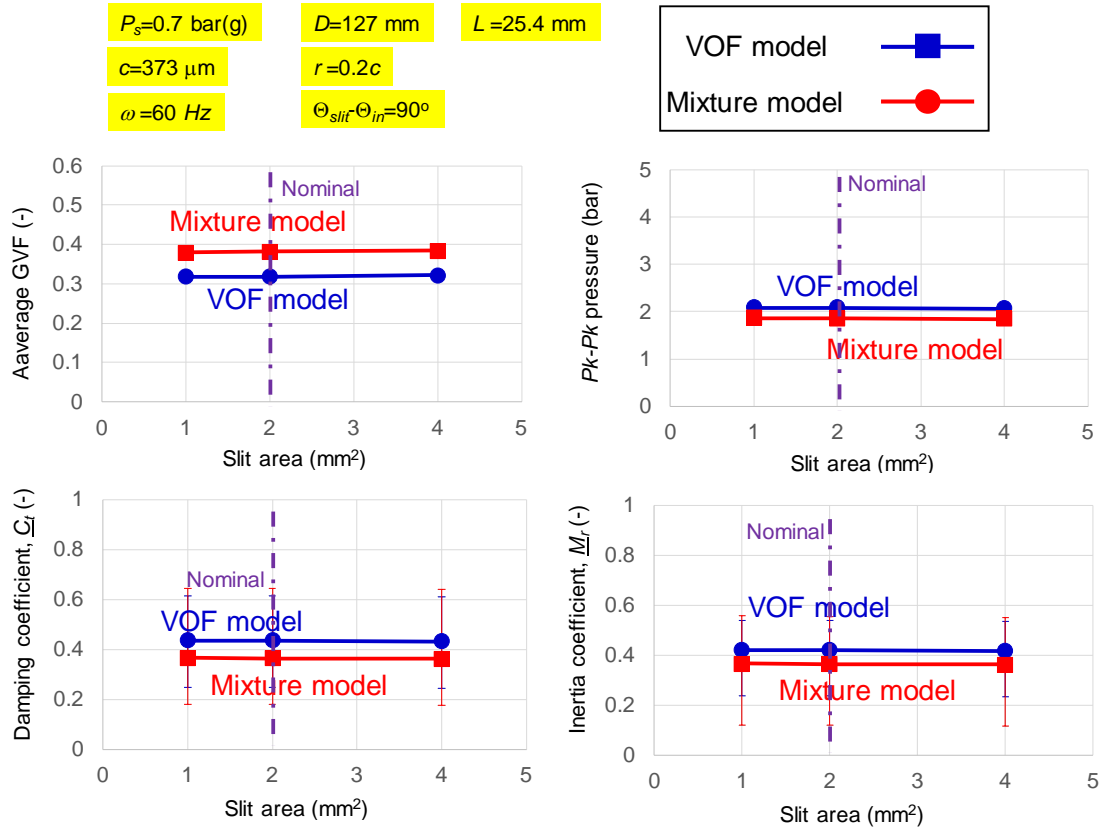


**Figure 37. Average GVF, film peak-to-peak pressure, and damping and inertia coefficients ( $\underline{C}_t$ ,  $\underline{M}_r$ ) vs. PR slit area ( $A_{slit}$ ): Predictions from (a) VOF model and (b) bubbly mixture model.  $P_s=0.7$  bar(g),  $D=127$  mm,  $L=25.4$  mm,  $c=373$   $\mu$ m,  $r=0.2c$ ,  $\omega=60$  Hz,  $\Delta\Theta=90^\circ$ .**

## CHAPTER IX<sup>8</sup>

### CONCLUSIONS

This dissertation presents measurements and analyses of the dynamic forced performance obtained from a sealed ends SFD operating (a) with a bubbly mixture and (b) with PR slits open to ambient. The predictions are benchmarked against the experimental test results. Two distinctive models evaluate the evolution of the GVF in the film land: a bubbly mixture model and a volume of fraction (VOF) model.

Air ingestion in SFDs, with either open ends or sealed ends, leads to operation with a *bubbly like* (air in oil) mixture that affects the SFD force coefficients, damping in particular. Research in the late 1990s' produced a wealth of experimental results and predictive models mainly for open ends dampers operating with a controlled bubbly mixture of known gas volume fraction. The models in Refs. [20, 21], validated by test results [37], when correlated to experiments with natural air ingestion [38] offer an accurate predictive tool to anticipate the effects of air ingestion under actual operating conditions.

Since then, although test results have become available for dampers sealed with piston rings (PR) and/or O-rings (OR) [34, 39, 40], no analytical effort has produced an accurate physical model for PR sealed ends dampers. Profuse experimental observation shows that PRs leak through the slit made by its abutted ends. Oil flows out as a jet at this location that is also the place drawing air into the squeeze film.

---

<sup>8</sup>Portions of this section reprinted with permission from [41] *Model and Experimental Verification of the Dynamic Forced Performance of a Tightly Sealed Squeeze Film Damper Supplied with a Bubbly Mixture* by San Andrés, L., and Koo, B., 2019, ASME J. Eng. Gas Turb. Pwr., GTP-19-1415, Copyright 2019 by ASME.

To date no archival publication has presented and compared the forced performance of sealed ends SFDs operating with a bubbly mixture vis-à-vis operating with natural air ingestion. This dissertation is an attempt to quantify natural air ingestion in a PR sealed ends SFD and shows a direct comparison of the bubbly mixture model prediction against those from a VOF method. To validate the models, the author uses two uniquely designed test rigs.

One test rig for bubbly mixture has one axial end PR sealed and another OR sealed. A bubbly mixture blended via a sparger with a controlled GVF enters thru an orifice feedhole and exits thru a PR slit submerged in a large volume of reservoir.

Another test rig (drawing natural air ingestion) has both axial ends sealed with PRs open to ambient. To avoid oil re-entering thru the PR slits, a suction pump continuously removes the oil as soon as it exits thru the PR slits.

In the experiments with a bubbly mixture, the supply pressure and inlet gas volume fraction vary (controlled), while the test SFD system performs circular orbits over a range of whirl frequencies. Both experimentally derived and predicted damping coefficients ( $C_{SFD}$ ) decrease by just ~20% as the GVF increases to 0.5. Thus, the sealed ends SFD is less sensitive to air ingestion as compared to an open ends SFD. On the other hand, the added mass coefficients ( $M_{SFD}$ ), both test derived and predicted, decrease rapidly with gas content. Predictions for damping and the added mass coefficients are lower (10% max. difference) than those derived from the experiments. Lubricant supply pressure has a small effect on the force coefficients because the dynamic pressure is not large enough to reach to the vapor pressure due to the small squeeze velocity.

The dynamic load tests evidence a quadrature stiffness that represents the friction of the PR sliding against the journal walls. This stiffness, derived from a force parallel to the squeeze velocity, increases with the magnitude of lubricant supply pressure that pushes the ring toward the journal groove. In practice, the quadrature stiffness could make the system appear overly *stiff* for displacements with a low frequency and also impair the (viscous) mechanical energy dissipation within the film.

The force coefficients predicted by the SFD with a bubbly mixture model show a good correlation with those of experimentally derived, the differences are within ~25% for damping and ~10% for the inertia coefficients. However, the model requires a reference GVF, which is barely known in a sealed ends SFD with natural air ingestion.

To produce an accurate physical model to predict the force coefficients of sealed ends SFDs operating with a natural air ingestion thru PR slits, the author investigated on a PRSFD not submerged in a pool of lubricant but facing ambient conditions that favor natural air ingestion. To model the SFD with the PR slits open to ambient, a VOF method is adopted. The sealed ends SFD model implementing the VOF method predicts well the experimentally derived damping coefficients; the difference is ~10%. Alas the model largely under-predicts the inertia coefficients by up to ~30%. In addition, a predicted time-space average GVF is adopted to model the SFD as if it were operating with a bubbly mixture. Predictions of the bubbly mixture model also show a good agreement with the test results, within 10% difference for the damping coefficients.

For a nominal condition of  $P_s = 0.7 \text{ bar(g)}$ ,  $r = 0.2c$ ,  $\omega = 60 \text{ Hz}$ , the GVF equals to ~0.4. The parametric study shows the GVF in the film land increases as the whirl frequency

( $\omega$ ) or the orbit radius increases ( $r$ ), i.e., as the squeeze velocity ( $v_s = r\omega$ ) grows. The axial film land length, the journal diameter, and the PR slit area do not significantly alter the average GVF. An increase in the supply pressure drastically decreases the GVF, but it does not fully eliminate gas in the film land. The GVF also decreases as the film clearance increases since the amount of the air entering thru the PR slit reduces due to a decrease in the generated film dynamic pressure. This parametric study shows that a conventional lubricant theory, Eq. (2), is not a good tool to predict the actual dynamic performance of a sealed ends SFD with natural air ingestion.

Most interestingly, the location of the PR slit relative to the feedhole significantly changes the GVF in the film. When the PR slit aligns with a feedhole, the film land is mostly filled with a pure lubricant. The GVF increases as the arc distance from the PR slit to the feedhole increases; and hence, the SFD dynamic forced performance worsens.

The radial and tangential forces vary over one full period of whirl motion due to the pressure distortions at the feedhole and the PR slits. However, the period-averaged force coefficients, hereby shown and discussed, effectively represent the dynamic performance of the SFD.

An experimental study including a broad range of squeeze velocities, and inlet/outlet lubricant supply pressure conditions could complement this research effort. In specific, a high speed camera could aid to track the path of air content in a squeeze film and so as to deliver the evolution of the GVF during damper operation. A formal investigation towards correlating the operating GVF to  $\gamma$  (feed flow parameter) would be a major step towards assessing a priori the likelihood of air ingestion in a sealed ends SFD. In spite of



the current effort, experimental and analytical, the sought correlation is but an illusion.

## REFERENCES

- [1] San Andrés, L., 2012, *Modern Lubrication Theory*, “Squeeze Film Dampers (SFDs),” Notes 13, Texas A&M University Digital Libraries, <http://oaktrust.library.tamu.edu/handle/1969.1/93197> [February 20<sup>th</sup>, 2018].
- [2] Vance, J. M., Zeidan, F. Y., and Murphy, B., 2010, *Machinery Vibration and Rotordynamics*, John Wiley & Sons, New York, Inc, 2010, pp. 216–238.
- [3] Zeidan, F. Y., San Andrés, L., and Vance, J. M., 1996, “Design and Application of Squeeze Film Dampers in Rotating Machinery,” *Proc. of the 25<sup>th</sup> Turbomachinery Symposium*, Turbomachinery Laboratory, September, Houston, 17-19<sup>th</sup> TX, pp. 169–188, (<http://oaktrust.library.tamu.edu/handle/1969.1/158832>) [February 20<sup>th</sup>, 2018].
- [4] Della Pietra, L. and Adiletta, 2002, “The Squeeze Film Damper over Four Decades of Investigations. Part I: Characteristics and Operating Features,” *Shock Vib. Dig.*, **34**(1), pp. 3–26.
- [5] San Andrés, L., 1985, “Effects of Fluid Inertia Effect on Squeeze Film Damper Force Response,” Ph.D. Dissertation, Texas A&M University, College Station, TX.
- [6] Jeung, S.-H., 2017, “Experimental Performance of an Open Ends Squeeze Film Damper and a Sealed Ends Squeeze Film Damper,” Ph.D. Dissertation, Texas A&M University, College Station, TX, USA.
- [7] Hirt, C. W., and Nichols, B. D., 1981, “Volume of Fluid (VOF) Method for the Dynamics of Free Boundaries,” *J. Comput. Phys.*, **39**, pp. 201–225.

- [8] Zeidan, F. Y., and Vance, J. M., 1990, "Cavitation Regimes in Squeeze Film Dampers and Their Effect on the Pressure Distribution," *STLE Tribol. Trans.*, **33**(3), pp. 447–453.
- [9] Braun, M. J., and Hannon, W. M., 2010, "Cavitation Formation and Modelling for Fluid Film Bearings: A Review," *Proc. of IMechE, Part J: Journal of Engineering Tribology*, **224**(9), pp. 839–863, September 1<sup>st</sup>.
- [10] Jung, S. Y., and Vance, J., 1993, "Effects of Vapor Cavitation and Fluid Inertia on the Force Coefficients of a Squeeze Film Damper Part I-Analysis of a Long SFD," *STLE Tribol. Trans.*, **36**(4), pp. 597–604.
- [11] Jung, S. Y., and Vance, J., 1993, "Effects of Vapor Cavitation and Fluid Inertia on the Force Coefficients of a Squeeze Film Damper Part II-Experimental Comparisons," *STLE Tribol. Trans.*, **36**(4), pp. 700–706.
- [12] Swift, H. W., 1932, "The Stability of Lubricating Films in Journal Bearings," *Minutes of the Proceedings of the Institution of Civil Engineers*, **233**, pp. 267–288.
- [13] Stieber, W., *Das schwimmlager: Hydrodynamiche Theorie des Gleitlagers*, Heidelberg, Berlin:VDI-Verlag.
- [14] Bayada, G., and Chupin, L., 2013, "Compressible Fluid Model for Hydrodynamic Lubrication Cavitation," *ASME J. Tribol.*, **135**, pp. 041–602.
- [15] Foberg, L., 1974, "Cavitation Boundary Conditions with Regard to the Number of Streamers and Tensile Strength of the Liquid," *Cavitation and Related Phenomena in Lubrication*, ImechE, England, pp. 31–36.

- [16] Elrod, H. G., 1981, "A Cavitation Algorithm," *ASME J. of Lubr. Tech.*, 103, pp. 350–354.
- [17] Sun, D. C., and Brewe, D. E., 1992, "Two Reference Time Scales for Studying the Dynamic Cavitation of Liquid Films," *ASME J. Tribol.*, **114**, pp. 612–615.
- [18] White, D. C., 1970, "Squeeze Film Journal Bearings," Ph.D. dissertation, Cambridge University, Cambridge, U.K.
- [19] Zeidan, F. Y., and Vance, J. M., 1989, "Cavitation Leading to a Two-Phase Fluid in a Squeeze Film Damper Bearing," *STLE Trib. Trans.*, **32**, pp. 100–104.
- [20] Tao, L., Diaz, S., San Andrés, L., and Rajagopal, K.R., 2000, "Analysis of Squeeze Film Dampers Operating with Bubbly Lubricants," *ASME J. Tribol.*, **122**, pp. 205–210.
- [21] Diaz, S., and San Andrés L., 2001, "A Model for Squeeze Film Dampers Operating with Air Entrainment and Validation with Experiments," *ASME J. Tribol.* **123**, pp. 125–133.
- [22] Mendez, T. H., Torres, J. E., Ciaccia, M. A., and Diaz, S., 2010, "On the Numerical Prediction of Finite Length Squeeze Film Dampers Performance with Free Air Entrainment," *ASME J. Eng. Gas Turb. Pwr.*, **132**, 012–501.
- [23] Xing, C., Braun, M. J., and Li, H., 2009, "A Three-Dimensional Navier-Stokes-Based Numerical Model for Squeeze-Film Dampers. Part 1-Effects of Gaseous Cavitation on Pressure Distribution and Damping Coefficients without Consideration of Inertia," *STLE Trib. Trans.*, **52**(5), pp. 680–694.

- [24] Xing, C., Braun, M. J., and Li, H., 2009, “A Three-Dimensional Navier-Stokes-Based Numerical Model for Squeeze-Film Dampers. Part 2-Effects of Gaseous Cavitation on the Behavior of the Squeeze Film Damper,” *STLE Trib. Trans*, **52**(5), pp. 695–705.
- [25] Younan, A. A., Cao, J., Dimond, T. M., and Allaire, P. E., 2010, “Nonlinear Analysis of Squeeze Film Damper with Entrained Air in Rotordynamic Systems,” *STLE Trib. Trans*, **54**(1), pp. 132–144.
- [26] Nikolajsen, J. K., 1999, “Viscosity and Density Models for Aerated Oil in Fluid-Film Bearings,” *Tribology Transactions*, **42**(1), pp. 186–191.
- [27] Gehannin, J., Arghir, M., and Bonneau, O., 2016, “A Volume of Fluid Method for Air Ingestion in Squeeze Film Dampers,” *STLE Trib. Trans.*, **59**(2), pp. 208–218.
- [28] Adiletta, G., and Pietra, L. D., 2006, “Experimental Study of a Squeeze Film Damper with Eccentric Circular Orbits,” *ASME J. Tribol.*, **128**, pp. 365-377.
- [29] Zeidan, F. Y., and Vance, J. M., 1990, “Cavitation and Air Entrainment Effects on the Response of Squeeze Film Supported Rotors,” *ASME J. Tribol.*, **112**, 347–353.
- [30] Dousti, S., 2014, “An Extended Reynolds Equation Development with Applications to Fixed Geometry Bearings and Squeeze Film Dampers,” Ph. D. Dissertation, University of Virginia, Charlottesville, VA, USA.
- [31] San Andrés, L., and Delgado, A., 2012, “A Novel Bulk-Flow Model for Improved Predictions of Force Coefficients in Grooved Oil Seals Operating Eccentrically,” *ASME J. Eng. Gas Turbines Power*, **134**, pp. 052–509.

- [32] San Andrés, L., and Diaz, S., 2002, “Pressure Measurements and Flow Visualization in a Squeeze Film Damper Operating with a Bubbly Mixture,” *ASME J. Tribol.*, **124**(2), pp. 346–350.
- [33] San Andrés, L. and Vance, J., 1987, “Effect of Fluid Inertia on Finite Length Sealed Squeeze Film Dampers,” *ASLE Transactions*, **30**(3), pp. 384–393, 1987.
- [34] San Andrés, L., Jeung, S.-H., Sean, D., and Savela, G., 2016, “Squeeze Film Dampers: an Experimental Appraisal of their Dynamic Performance,” *Proc. of the 1<sup>st</sup> Asia Turbomachinery and Pump Symposium*, Singapore, February, 22–25<sup>th</sup>, (<https://oaktrust.library.tamu.edu/handle/1969.1/158832>) [February 20<sup>th</sup>, 2018].
- [35] San Andrés, L., 2012, *Modern Lubrication Theory*, “Thermohydrodynamic Bulk-Flow Model in Thin Film Lubrication,” Notes 10, Texas A&M University Digital Libraries, <http://oaktrust.library.tamu.edu/handle/1969.1/93197> [February 20<sup>th</sup>, 2018].
- [36] Fritzen, C. P., 1986, “Identificatio of Mass, Damping, and Stiffness Matrices of Mechanical Systems,” *J. Vib. Acoust.*, **108**(1), pp. 9–16.
- [37] Diaz, S. E., 1999, “The Effect of Air Entrapment on the Performance of Squeeze Film Dampers: Experiments and Analysis,” Ph. D. Dissertatio, Texas A&M University, College Station, TX, May.
- [38] San Andrés, L., and Diaz, S., 2003, “Flow Visualization and Forces from a Squeeze Film Damper Operating with Natural Air Entrainment,” *ASME J. Tribol.*, **25**, pp. 325–333.

- [39] San Andrés, L., Koo, B., and Jeung, S.-H., 2019, “Experimental Force Coefficients for Two Sealed Ends Squeeze Film Dampers (Piston Rings and O-rings): An Assessment of Their Similarities and Differences,” *ASME J. Eng. Gas Turb. Pwr.*, **141**, 021–024.
- [40] San Andrés, L., and Koo, B., 2018, “Effect of Lubricant Supply Pressure on SFD Performance: Ends Sealed with O-rings and Piston Rings,” Paper No. IFToMM2018-0181, *Proc. Of IFToMM Conference on Rotordynamics*, September, 23–27<sup>th</sup>, Rio de Janeiro, Brazil.
- [41] San Andrés, L., and Koo, B., 2019, “Model and Experimental Verification of the Dynamic Forced Performance of a Tightly Sealed Squeeze Film Damper Supplied with a Bubbly Mixture,” *Proc. Of ASME Turbo Expo 2019*, GT2019-90330, June 17-21<sup>st</sup>, Phoenix, AZ, USA.
- [42] “NI cDAQ -917x User Manual,” User manual for NI compact DAQ 9171/9174/9178 USB Chassis, National Instruments, July, 2011.
- [43] Coleman, H. W., and Steele, G. W., 1998, *Experimentation and Uncertainty Analysis for Engineers*, John Wiley & Sons, New York.
- [44] Beckwith, T., Marangoni, R., and Lienhard, J., 1993, “Mechanical Measurements,” Prentice Hall, 5<sup>th</sup> edition, pp.82.

## APPENDIX A

### IDENTIFIED PARAMETERS FOR THE UNLUBRICATED TEST SYSTEM

Figure A1 shows the measured real and imaginary parts of complex dynamic stiffness coefficients ( $H$ ) and the physical model fits for the dry system, i.e. without a lubricant, versus frequency. The graphs include the results for tests without (open ends) and with the end seals in place. Recall that end seals refer to the O-ring (OR) and piston ring (PR) installed at the bottom and top ends of the damper journal, respectively. Table A1 lists the identified force coefficients, the dry system natural frequency and its damping ratio. Note that as  $\omega \rightarrow 0$ , the imaginary part of  $H$  does not have a null magnitude, thus evidencing the quadrature stiffness ( $K_0$ ). The effect is more evident when the two seals (unlubricated) are in place. The end seals do not show viscous damping, when compared to that of the structure.

The real part of the complex stiffness,  $\text{Re}(H)$ , shows the end seals do increase the system stiffness,  $\sim 20\% K_S$ , but do not affect the system effective mass. Note that with the seals in place, the *dry* system natural frequency increases  $\sim 20\%$ ; whereas the damping ratio remains at  $\sim 7\%$ . Note the structure damping and inertia coefficients are slightly orthotropic since the test system includes many inlet/outlet lubricant lines and non-flexible connections to the various sensors. The inset table in the figure lists the correlation coefficient ( $R^2$ ) between the measurements and the fit to the physical model. The test results for the real parts,  $\text{Re}(H)$ , show good correlation ( $R^2 > 0.9$ ) to the model. However, the goodness of the fit for the imaginary parts is poor ( $R^2 \sim 0.5$ ) since, as



expected, the structure damping is non viscous. Nonetheless, as  $C_s/C^* \sim 0.1$ , it is a small fraction of the viscous damping in the fluid film.

**Table A1. Dry system structural parameters (without and with end seals, PR-OR) obtained from circular orbit tests without any lubricant. Parameters identified over frequency range 10–60 Hz. Orbit amplitude  $r = 0.2c$ .**

			(a) Open ends		(b) Seals installed		(c) Seals only	
			No seals				(b)-(a)	
Physical parameter			Direct		Direct		Direct	
			XX	YY	XX	YY	XX	YY
$K$	[MN/m]		3.0		4.0		1	1
$C$	[kN-s/m]		0.6	0.7	0.7	0.5	-0.5	0.1
$K_0$	[MN/m]		0.2	0.3	0.5	0.5	0.5	0.3
$M^{(*)}$	[kg]		8.1	3.1	5.8	2.1		
Natural frequency	$f_n$	[Hz]	53	65	63	74	$f_n = (K_s/M_s)^{0.5}$	
Damping ratio	$\zeta_s$	[-]	0.10	0.07	0.05	0.08	$\zeta_s = C_s/(2M_sK_s)^{0.5}$	

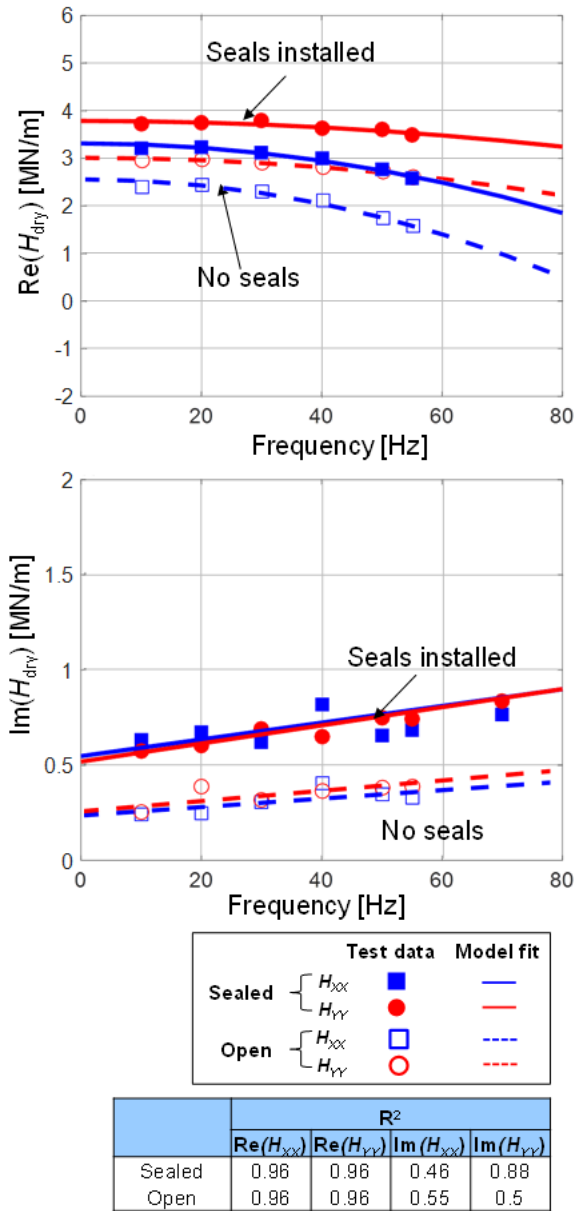


**Figure A1. Dry test system (without lubricant): real and imaginary parts of system dynamic complex stiffnesses ( $H_{xx}$ ,  $H_{yy}$ ) versus excitation frequency. With and without end seals (PR-OR). Orbit amplitude  $r = 0.2c$ . Test data and model fits in frequency range 10 Hz to 70 Hz.**

## APPENDIX B

### UNCERTAINTY OF IDENTIFIED FORCE COEFFICIENTS

A total uncertainty consists of a bias uncertainty and measurement variability. These uncertainties are outlined, along with the combination of bias uncertainty and variability into the total uncertainty for each dynamic force coefficient ( $K$ ,  $C$ ,  $M$ ).  $U_B$ ,  $U_V$ , and  $U_t$  denote bias uncertainty, variability, and total uncertainty, respectively.

The total uncertainty of a measurement with variables is

$$U_t = \sqrt{(U_1)^2 + (U_2)^2 + \dots + (U_N)^2} \quad (\text{B1})$$

when  $N$  is the number of variables.

#### **Bias uncertainty**

- The data acquisition system (DAQ) has a rated resolution of  $U_{B,DAQ}=0.1$  % [42] in a measured voltage, i.e., 1 mV. The 4096 samples with a sampling rate of 16,384 Hz gives an uncertainty in the out frequency of 2 Hz for the entire frequency range. For a nominal whirl frequency of 60 Hz, the frequency uncertainty is 3.3%.
- An uncertainty of a displacement sensor with the sensor sensitivity of 33.4 mV/ $\mu\text{m}$  is 0.3  $\mu\text{m}$ . For the nominal orbit radius of  $r=0.2c=74.6$   $\mu\text{m}$ , the uncertainty of the measured displacement  $U_{B,D}=0.4$  %.
- An uncertainty of a load cell with the sensor sensitivity of 2.25 mV/N is 0.44 N. For the measured peak load at the nominal operating condition ( $P_s=10$  psig,  $r=0.2c$ ,  $\omega=60$  Hz), the uncertainty of the measured load  $U_{B,L}=0.7$  %.

- An uncertainty of an accelerometer with the sensor sensitivity of 11 mV/(m/s<sup>2</sup>) is 0.091 m/s<sup>2</sup>. For a nominal squeeze acceleration ( $a_s = r\omega^2$ ) at  $r = 0.2c$  and  $\omega = 60$  Hz, the uncertainty of the measured acceleration  $U_{B,A}=0.9\%$ .

The total bias uncertainties in the complex dynamic stiffness ( $H$ ) from the individual measurement uncertainties at the nominal condition are

$$U_B = \sqrt{(U_{B,D})^2 + (U_{B,L})^2 + (U_{B,A})^2 + (U_{B,\omega})^2} = 3.5\% \quad (\text{B2b})$$

### Uncertainty due to curve fit

A complex stiffness is estimated at several selected frequencies ( $\omega$ ) to identify force coefficients. The real and imaginary parts of the complex dynamic stiffness are curve fitted to the physical model,  $\text{Re}(H)=(K-M\omega^2)$  and  $\text{Im}(H)=(K_0+C\omega)$ , with both correlation factor ( $R^2$ ).

Ref. [43] presents the standard deviation of the intercept and slope of a curve fit as

$$S_{Intercept} = \sqrt{\frac{1}{N(N-2)} \frac{1-R^2}{R^2}}$$

$$S_{Slope} = \sqrt{\frac{1}{(N-2)} \frac{1-R^2}{R^2}} \quad (\text{B4})$$

where  $N$  denotes the number of frequencies selected for a curve fit.

To estimate the uncertainty from the curve fit correlation factor ( $R^2$ ), a precision uncertainty equation in Ref.[44] gives

$$U_{R,K} = \frac{t_d \cdot S_{Intercept}}{K} \quad (\text{B3a})$$

$$U_{R,C} = \frac{t_d \cdot S_{Slope}}{C} \quad (B3b)$$

$$U_{R,M} = \frac{t_d \cdot S_{Slope}}{M} \quad (B3c)$$

where  $t_d$  denotes the Student's t-distribution and  $U_R$  denotes the uncertainties due to curve fit. Note  $t_d=1.96$  corresponds to a 95 % confidence interval. (K, C, M)=(2.6 MN/m, 10 kN-s/m, 43 kg).

For the nominal operating condition, the uncertainty due to the curve fit is ( $U_{R,K}$ ,  $U_{R,C}$ ,  $U_{R,M}$ )=(5.4 %, 6.0 %, 11 %).

### Uncertainty due to variability

An uncertainty due to variability deals with repeatability of measurements. As an effort assess the repeatability of the tests and the identified force coefficients, each test result is measured and recorded for 1 second including several periods of the whirl motion to calculate the standard deviation of the force coefficient among the whirl motions.

An uncertainty due to variability is a function of the Student's t-distribution ( $t_d$ ) and the standard deviation of the result ( $S_i$ ) [44].

$$U_{V,x} = \frac{t_d S_x}{x}; \quad x = K, C, M \quad (B5)$$

The formula for the sample standard deviation is

$$S_x = \sqrt{\frac{1}{(N-1)} \sum_{i=1}^N (x_i - \bar{x})^2} \quad (\text{B6})$$

where  $x$  denotes measured data,  $\bar{x}$  denotes an average of all measured data, and  $N$  denotes the number of the data point. Subscript  $i$  is the data index number.

Table B1 lists the actual force coefficients measured from the system of the PR sealed SFD operating with ends open to ambient. The test was repeated three times under the nominal condition,  $P_s=0.7$  bar(g),  $r=0.2c$ ,  $\omega=40-70$  Hz,  $\Delta\Theta=90^\circ$ .

**Table B1. Identified system force coefficients ( $K, C, M$ )<sub>L</sub> for the PR sealed ends SFD at the nominal operating condition:  $P_s=0.7$  bar(g),  $r=0.2c$ , and  $\omega=40-70$  Hz.**

Test #	$K_{XX}$ (MN/m)	$K_{YY}$ (MN/m)	$C_{XX}$ (kN-s/m)	$C_{YY}$ (kN-s/m)	$M_{XX}$ (kg)	$M_{YY}$ (kg)
1	2.5	3.0	9.2	11.6	45.7	41.1
2	2.7	2.5	9.0	11.4	46.3	38.6
3	3.0	2.2	9.5	11.8	50.3	35.2

The uncertainties due to variability are

$$U_{V,K} = 2.4\% \quad (\text{B7a})$$

$$U_{V,C} = 4.6\% \quad (\text{B7b})$$

$$U_{V,M} = 12.5\% \quad (\text{B6c})$$

### Total uncertainty

The total uncertainty in the SFD dynamic forced coefficients are

$$U_{i,K} = \sqrt{(U_B)^2 + (U_{R,K})^2 + (U_{V,K})^2} = 6.9\% \quad (\text{B7a})$$

$$U_{i,C} = \sqrt{(U_B)^2 + (U_{R,C})^2 + (U_{V,C})^2} = 8.3 \% \quad (\text{B7b})$$

$$U_{i,M} = \sqrt{(U_B)^2 + (U_{R,M})^2 + (U_{V,M})^2} = 17 \% \quad (\text{B7c})$$

## APPENDIX C

### ESTIMATION OF THE LOSS COEFFICIENTS FOR A FEEDHOLE AND PISTON RING SLITS

Figure C1 shows a hydraulic circuit with flow resistances ( $R$ ) to represent the flow of lubricant through the journal. The pump supplies the ISO VG 2 oil into the the journal at the supply pressure ( $P_s$ ) and flowrate  $Q_{in}$ . The flow resistance through an orifice with a check valve is denoted as  $R_o$  and the flow resistances for the top and bottom film lands are  $R_{TL}$  and  $R_{BL}$ , respectively. Oil flows through the PR slits at the top and bottom end of the film land denoted as  $R_{TS}$  and  $R_{BS}$ .

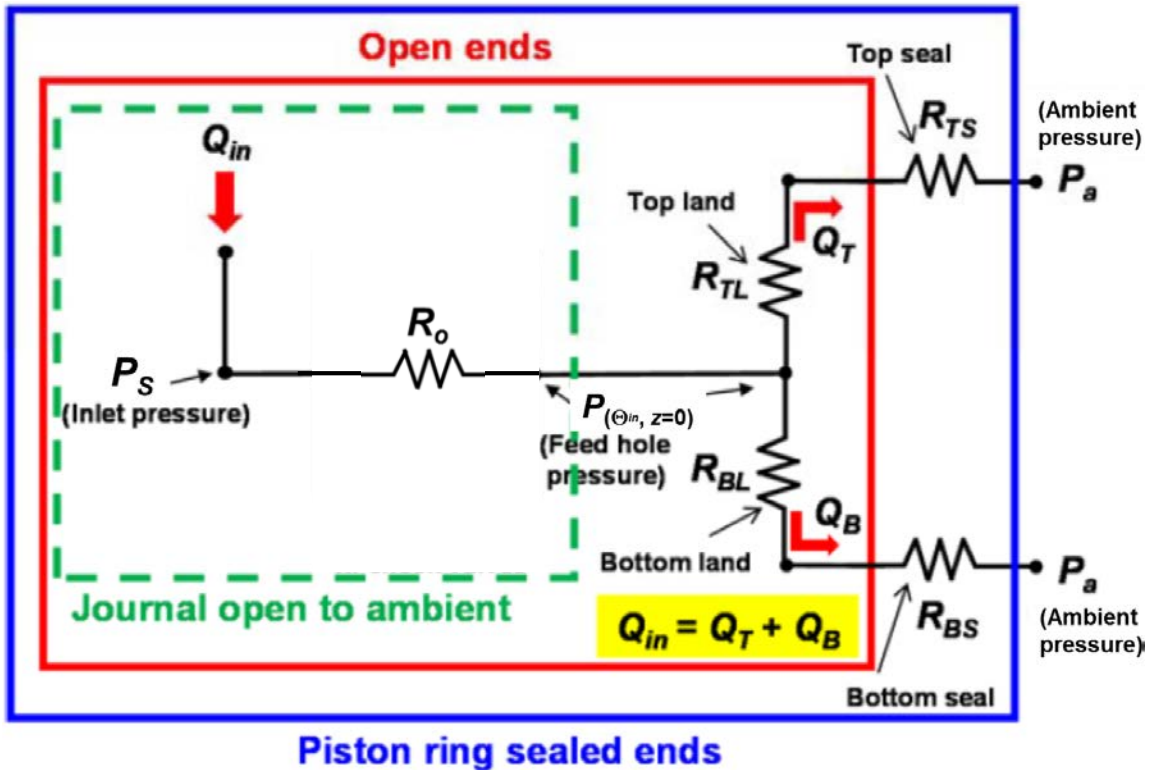


Figure C1. Flow diagram of lubricant through journal with hydraulic resistances for open condition and piston ring sealed ends SFD.



A pressure gauge measures the inlet supply pressure ( $P_s$ ) of the lubricant before entering the journal while a flow meter records the inlet flowrate ( $Q_{in}$ ) through the journal. The flowrate through the top and bottom sections ( $Q_T$  and  $Q_B$ ) are calculated by the time to fill a known volume located underneath the bearing cartridge,  $Q_{in}=Q_T+Q_B$ .

$$Q_{in} = \frac{P_s - P_{(\Theta_{in}, z=0)}}{\left(\frac{R_o}{n}\right)} = Q_T + Q_B \quad (D1)$$

$$Q_T = C_T P_{(\Theta_{in}, z=0)}; Q_B = C_B P_{(\Theta_{in}, z=0)} \quad (D2)$$

where  $C_T$  and  $C_B$  denote the flow conductances for top and bottom sections of the journal where  $C=1/R$ . In addition,  $n$  denotes the number of the feedholes.

Figure C2 displays the recorded inlet flowrate ( $Q_{in}$ ) versus the supply pressure ( $P_s$ ) for the flow through the orifices and a journal open to ambient (blue circles), open ends SFD (red squares), and PR sealed ends SFD (purple triangles). A slope of the trend line indicates a flow conductance ( $1/R$ ). for the journal open to ambient condition, the slope shows the flow conductance,  $C_o=1/R_o=0.9$  ( $\text{mm}^3/\text{s}/\text{Pa}$ ). By the hydraulic network shown in Fig. C1, the averaged PR sealed flow conductance through the top and bottom seals  $C_S =0.2$  ( $\text{mm}^3/\text{s}/\text{Pa}$ ). From Eqs. (14-15) at the supply pressure of 0.7 bar(g), the orifice-like coefficients are  $C_d=1.0$  and  $C_{slit}= 0.5$ .

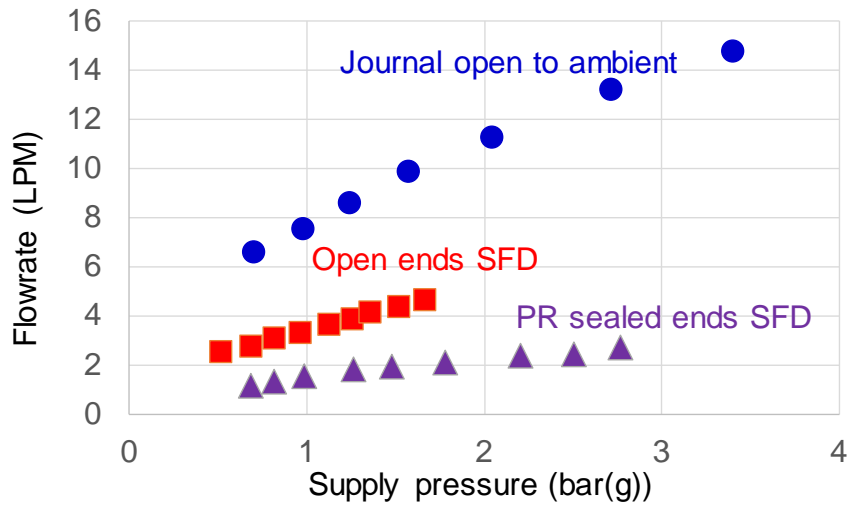


**Figure C2. Lubricant flowrate ( $Q_{in}$ ) vs. supply pressure ( $P_s$ ): Journal open to ambient pressure, open ends damper, and PR sealed ends damper.**